Synergy of decay spectroscopy and mass spectrometry for the study of exotic nuclides

DISSERTATION

zur Erlangung des akademischen Grades

Doctor rerum naturalium
(Dr. rer. nat.)

vorgelegt

der Fakultät Mathematik und Naturwissenschaften
der Technischen Universität Dresden

von

Dipl. Phys. Juliane Stanja

geboren am 29.05.1986 in Mühlhausen

Eingereicht am 19.12.2012

Gutachter:	Prof. Dr. Kai Zuber
	Prof. Dr. Klaus Blaum
Tag der Verteidigung:	12.04.2013

Zusammenfassung

Mit nur 2 Bestandteilen weisen Atomkerne eine reiche Struktur auf, die von der Anordnung der Protonen- und Neutronenzustände abhängt. Diese Anordnung kann insbesondere in der Nähe von Schalenabschlüssen zur Bildung von angeregten Zuständen mit ungewöhnlich langen Halbwertszeiten, auch Isomere genannt, führen. Massenspektrometrie an kurzlebigen Nukliden wird oft durch die Existenz dieser Zustände erschwert, die eine höhere Produktionsrate als der Grundzustand aufweisen können.
Diese Arbeit präsentiert die ersten Ergebnisse, die mit einem Zerfallsspektroskopiesystem gewonnen wurden, das an das hochauflösende Penningfallen Massenspektrometer ISOLTRAP gekoppelt ist, welches sich am Isotopenseparator ISOLDE am CERN befindet. Es wurden die Isomere in den neutronenarmen Thalliumisotopen untersucht. Die Daten für $^{184,190,193-195}$Tl erlauben es, bereits existierende Massenwerte zu verbessern und für die Isotope ^{190,193,194}Tl eine Massen-Spinzustands-Zuweisung vorzunehmen. Da für ^{194}Tl sowohl der Grundzustand als auch der isomere Zustand beobachtet wurden, konnte die Anregungsenergie des isomeren Zustands zum ersten Mal experimentell bestimmt werden. Mit Hilfe der Daten wurden systematische Trends in der Nähe des Schalenabschlusses bei $Z = 82$ diskutiert.

Abstract

With only two ingredients, atomic nuclei exhibit a rich structure depending on the ordering of the different proton- and neutron-occupied states. This ordering can give rise to excited states with exceptionally long half-lives, also known as isomers, especially near shell closures. On-line mass spectrometry can often be compromised by the existence of such states that may even be produced in higher proportion than the ground state.
This thesis presents the first results obtained from a nuclear spectroscopy setup coupled with the high-resolution Penning-trap mass spectrometer ISOLTRAP, at CERN's radioactive ion beam facility ISOLDE. The isomerism in the neutron-deficient thallium isotopes was investigated. The data on $^{184,190,193-195}$Tl allow an improvement of existing mass values as well as a mass-spin-state assignment in ^{190,193,194}Tl. Due to the presence of the ground and isomeric state for ^{194}Tl the excitation energy of the latter was determined for the first time experimentally. Systematic trends in the vicinity of the $Z = 82$ shell closure have been discussed.

Contents

List of Figures

List of Tables

1. Introduction

The question what is the internal structure of matter exists since more than 2400 years. The Greek Democritus speculated that matter is divisible until a smallest indivisible unit of matter is reached. This unit he called an atom.
At the end of the 19th century, Bequerel discovered the spontaneous emission of radiation from uranium compounds [Beq96] which was later found to originate from the uranium atom itself. M. Curie demonstrated, during her studies on this new property which she called radioactivity, that there are other elements showing a similar behavior. Studying the penetration of matter and the ionization of air by the emitted radiation, Rutherford and Villard classified three different types of radiation as α, β and γ radiation [Rut98, Vil00]. Bombarding thin gold foils with α radiation it was shown by Rutherford, Geiger and Marsden that the atom itself consists of a small and dense nucleus and an electron cloud around it [GM09, Rut11]. This observation gave birth to the branch nuclear physics which is dedicated to the investigation of nuclear properties.
At the beginning, the internal structure of the nucleus posed one of the main problems which was solved by the discovery of the neutron in 1932 by Chadwick [Cha32]. The nucleus itself was thus found to consist of the nucleons that can be subdivided into the charged protons and the uncharged neutrons. The nucleons are held together by the nuclear force which on short distances is stronger than the Coulomb repulsion of the protons. By the number of protons Z, the chemical element, and by the number of neutrons N, the isotope of the element with mass number $A = Z + N$ is determined. Based on this knowledge the first mass formula was derived by Weizsäcker in 1935 [vW35]. With this formula the instability against radioactive decay which is observed for several nuclei, see Fig. 1.1, can be understood as driven by mass minimization. In the following, radioactivity is understood as the spontaneous change of species, typically accompanied by the emission of charged particles and gamma-rays.
Already in the early years of nuclear physics some nuclei were found to decay with different half-lives although from the same element and with the same mass number. In 1936, Weizsäcker suggested that this is due to the decay of different metastable states in the same nucleus which can be distinguished by their energy and total angular momentum [vW36]. The state at lowest energy is called the ground state and metastable excited states are referred to as isomers [WD01]. Weizsäcker already assumed that isomers arise if the deexcitation to lower states in the same nuclide is accompanied by a dramatic change in angular momentum. However, a nuclear model was still missing. The observation of nuclei, becoming extremely bound at certain magic nucleon numbers $\{Z, N\} = \{2, 8, 20, 28, 50, 82, ...\}$, finally raised the idea of a nuclear shell structure in analogy to the atomic one [MJ55]. With the resulting shell model different nuclear states can be interpreted as different nucleon configu-

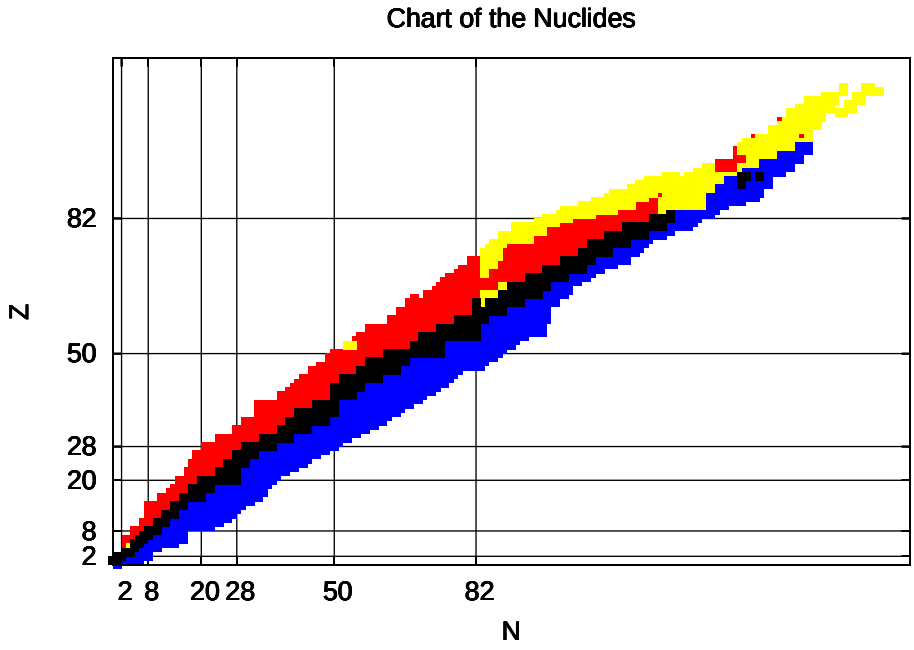

Figure 1.1: Chart of the Nuclides that shows all nuclei presently known, adopted from [MPD12]. They are color coded by their decay type - β^+/EC-(red), β^--(blue) and α-decay (yellow). Stable nuclei are marked black. The black lines mark the magic numbers where shell closures occur.

rations. Thus, studies on nuclear excited states can reveal information about nuclear structure in analogy to the atom.
This work focuses on the neutron-deficient thallium (Tl, $Z = 81$) isotopes in the vicinity of the $Z = 82$ magic number. Most of them have isomeric states at only a few hundreds keV [JA60, Vea74]. Their investigation for nuclear structure studies becomes especially interesting with respect to the reports about deformation and shape coexistence which exist in this region [Hea83]. The nuclear properties under investigation are the masses, the excitation energies of the isomers and the spin-state ordering of the ground and isomeric states. Some of these properties are just predicted from systematics, as for ^{194}Tl and ^{190}Tl [ens12]. A measurement principle to approach the missing data in a unique way, namely by combining high-precision mass measurements with nuclear decay spectroscopy, is presented. The radioactive nuclides are produced at the ion-beam facility ISOLDE at CERN. The first step is a high-precision mass measurement on the ion sample that allows to distinguish between ground and isomeric state. This, as well as the isomeric purification, is carried out with the Penning-trap mass spectrometer ISOLTRAP. In the second step a decay pattern is assigned to the purified ion sample from nuclear decay spectroscopy. For this purpose, a decay station was attached to the ISOLTRAP experiment. The information from both measurements together allows to determine a spin-state ordering.

The basics of nuclear physics relevant for this work are briefly reviewed in chapter 2. The experimental setup of the ISOLTRAP experiment as well as of the decay station are presented in detail in chapter 3. Since the attachment of the decay station to the Penning traps required modifications to the previous beam line, transport-efficiency simulations have been made. The feasibility of an alternative beam-line design based on a quadrupole bender was tested. Furthermore, the decay-spectroscopy system was studied with Monte-Carlo simulations with respect to detection efficiencies. The simulation studies are presented in chapter 4. The combination of mass and decay measurements at the ISOLTRAP setup was first applied on ^{184,190,193,194,195}Tl. In chapter 5 details on the data analysis as well as the results for each measured nuclide will be presented. The impact of these measurements on the physics in this region is discussed in chapter 6. A summary and an outlook are given in chapter 7.

2. Basics of nuclear physics

Up to now, about 3000 nuclides have been discovered, see Fig. 1.1. Their properties, such as the mass, the total angular momentum and parity, radioactive decay modes and nuclear excited states, are typically determined from different and complementary experiments. All of them are required to draw a consistent picture of a nucleus or an isotopic chain, and thus of the region they are representing on the nuclear chart.
In the following, a brief overview on the nuclear properties is given. An interpretation of nuclear properties in terms of nuclear structure can be carried out in the vicinity of shell closures by the shell model, which is presented briefly. More details can be found for example in [Kra88].

2.1. Nuclear properties

The mass m_N of a nucleus with Z protons and N neutrons is given by

$$m_N c^2 = m_A c^2 - Z m_e c^2 + \sum_{i=1}^{Z} B_i \tag{2.1}$$

where m_A is the atomic mass, m_e is the electron mass and B_i is the binding energy of the ith electron. The last term is usually omitted since electron binding energies are much smaller than the atomic mass. The nuclear mass does not equal the sum of the masses of its constituents. The difference

$$\Delta m(Z,N) = Z \cdot m_p + N \cdot m_n - m_N \tag{2.2}$$

is called the mass defect, with m_p the proton mass and m_n the neutron mass, and is linked to the binding energy B of the nucleus by the mass-energy equivalence $B(Z,N) = \Delta m c^2$.
The total angular momentum $\mathbf{I}$ and parity Π of the nucleus are constructed from the total angular momenta and parities of all nucleons

$$\mathbf{I} = \sum_{p=1}^{Z} \mathbf{j}_p + \sum_{n=1}^{N} \mathbf{j}_n \tag{2.3}$$

$$\Pi = \prod_{p=1}^{Z} \pi_p \cdot \prod_{n=1}^{N} \pi_n. \tag{2.4}$$

The total angular momentum of a nucleon inside a nucleus itself is composed of the orbital angular momentum $\mathbf{l}$ and the spin $\mathbf{s}$

$$\mathbf{j} = \mathbf{l} + \mathbf{s}. \tag{2.5}$$

Since the nucleons are fermions with spin-quantum number $s = \frac{1}{2}$ the total angular-momentum quantum numbers of all nucleons are half-integral. Thus, odd-A nuclei will have half-integer and even-A nuclei will have integer total angular-momentum quantum number. To predict the parity of the nucleus in the ground or one of the excited states, the wave functions of all nucleons must be known. In general, this is not the case and thus the parity can only be measured or predicted under certain assumptions.

2.2. The shell model

By means of nuclear models, the behavior even of unknown nuclear properties can be predicted. In addition, nuclear models support the interpretation of some nuclear properties. The description of the nucleus must take all nucleons and their interactions into account. For nuclei with more than two nucleons this is a many-body problem with a nuclear potential determined not only from two-nucleon but also from three-nucleon interactions. To circumvent the mathematical complexity of this problem, simplifications are carried out which still allow to confirm measured nuclear properties and predict new ones.
The independent-particle model was the first successful nuclear model. In 1948, Goeppert-Mayer summarized the behavior of several nuclear properties and pointed to the particular stability of nuclei at certain even nucleon numbers which she interpreted as closed shells [May48]. Only one year later, [May49] and [HJS49] reproduced these numbers from calculations. It is assumed that the nucleons are independent of each other. Thus, the Schrödinger equation can be solved for each nucleon separately, with an average nuclear potential created only by two-nucleon interactions of the remaining nucleons. For simplification, this potential can be taken either as a square well or as a spherical harmonic-oscillator potential, although a Wood-Saxon potential which has a shape in between both potentials is more realistic. Furthermore, a strong spin-orbit coupling term has to be added, which leads to a level splitting according to $j = l \pm \frac{1}{2}$, where the level with high j is lowered significantly in energy and the level with low j is slightly raised in energy. Thus, groups of states arise at very similar energies within a group and large energy distances between the groups, see Fig. 2.1. This is understood as shell structure with shell gaps appearing exactly at the magic numbers. Initially, the concept of shells seems confusing in the dense volume of the nucleus due to the many collisions that are expected. This is solved by the Pauli principle. Then nucleon collisions are only allowed if there exists a final state that they are able to reach, which mostly is only possible for valence nucleons [Kra88]. Finally, the many-body wave function is the anti-symmetric product of the single-particle wave functions and the energy eigenvalues are the sum of single-particle energy eigenvalues. The state with the lowest energy is called the ground state and all states with higher energy

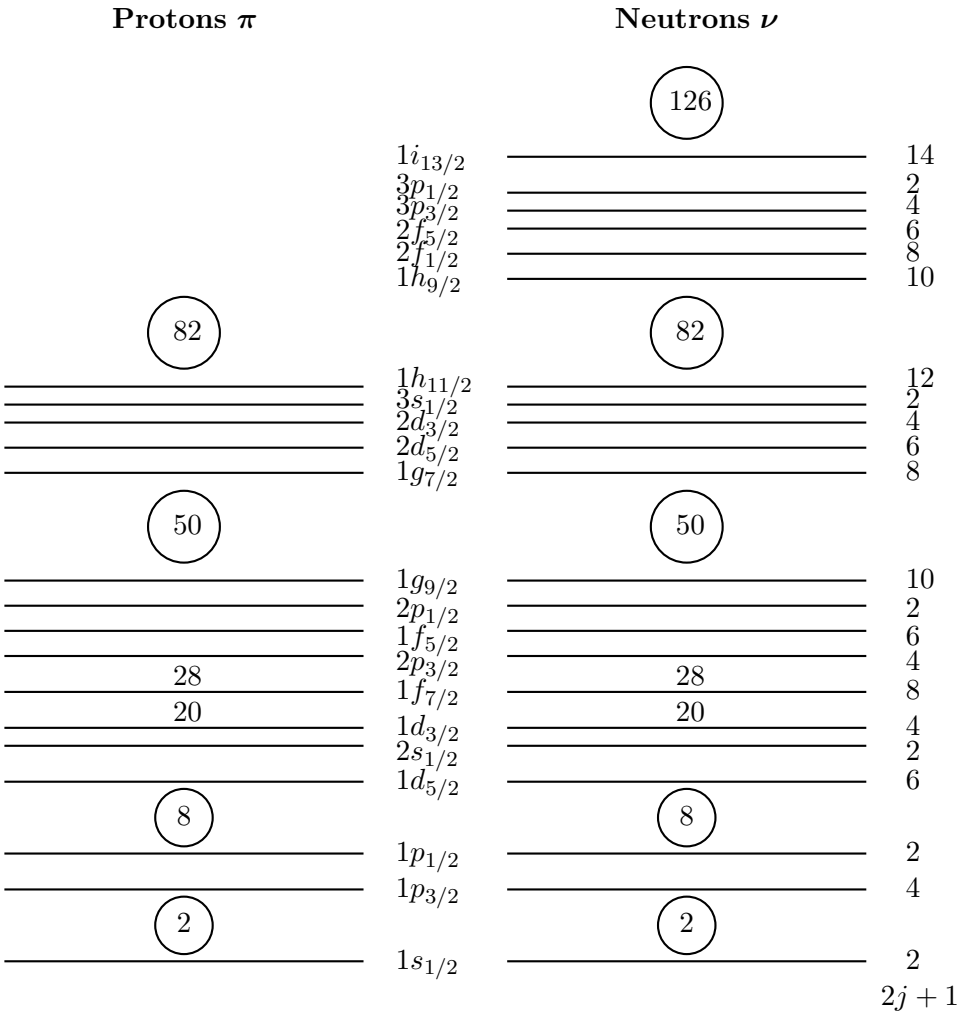

Figure 2.1: Energy levels for protons and neutrons that result from a shell model with an intermediate potential that includes the spin-orbit interaction. To the right the maximum number of nucleons $2j + 1$ for each level is given. The magic numbers that represent shell closures are also shown.

are excited states which arise due to nucleon excitations. Within this model, predictions about the spin and parity of the ground state and to some extent of excited states can be made by assuming that closed shells and paired nucleons in open shells do not contribute. Especially for nuclei in the vicinity of magic numbers this has proven to be a good approximation.
The key point of models based on the independent particle model is the construction of a suitable nuclear potential. The criterion is to fit experimental data by theory. Discrepancies can be overcome by including additional terms such as a tensor force or a quadratic spin-orbit interaction. An overview of potentials based on two-nucleon interactions is given in [Bet71]. More recently also three-nucleon interactions have been taken into account for light nuclei

[PPW01]. Two-nucleon and many-body interactions are reviewed in [BFS10].

2.3. Radioactive decay

From the experimental point of view, nuclear structure can be investigated and understood by studying the properties of nuclear excited states in analogy to atomic physics. Excited states are for example produced in the laboratory by radioactive decay where one nucleus, referred to as the mother nucleus, is spontaneously transformed into another lighter nucleus - the daughter nucleus. Here, the radioactive decay follows the decay law

$$n(t) = n_0 \cdot e^{-\frac{\ln 2 \cdot t}{t_{1/2}}} \tag{2.6}$$

where n_0 is the initial number of mother nuclei and $t_{1/2}$ is the time needed for half of the nuclei to decay, also referred to as the half-life of the mother nucleus. The main types of nuclear decay are α-decay, β^+- and β^--decay. During α-decay a α-particle, a ^{4}He nucleus, can escape from the mother nucleus via tunneling, leaving the daughter nucleus with $A' = A - 4$ and proton number $Z' = Z - 2$

$$^A_Z X_N \longrightarrow ^{A-4}_{Z-2} X'_{N-2} + \alpha. \tag{2.7}$$

This process happens mostly for heavy nuclei with $Z > 83$ where the Coulomb repulsion of the protons increases faster than the attractive nuclear force. Nuclei that show either proton or neutron excess tend to undergo β-decay where one nucleon type is converted into the other. In β^-- decay

$$^A_Z X_N \longrightarrow ^A_{Z+1} X'_{N-1} + e^- + \bar{\nu}_e \tag{2.8}$$

a neutron is converted into a proton, an electron and an electron-anti-neutrino are emitted. Neutron-rich nuclei that undergo this type of decay are marked blue in Fig. 1.1. The neutron-deficient nuclei, marked red in Fig. 1.1, decay via β^+-decay

$$^A_Z X_N \longrightarrow ^A_{Z-1} X'_{N+1} + e^+ + \nu_e \tag{2.9}$$

where a proton is converted into a neutron, a positron, or anti-electron, and an electron-neutrino. This process is only possible if there exists an electron to combine with the proton. Electrons within the nucleus can be created via e^+-e^--pair production. Thus, the mass difference between the mother and the daughter nucleus must be at least $2 \cdot m_e c^2$ =1022 keV to create an electron-positron pair. A competing process that is allowed even below this limit is the capture of an atomic electron (EC)

$$^A_Z X_N + e^- \longrightarrow ^A_{Z+1} X'_{N-1} + \nu_e \tag{2.10}$$

that also leads to a conversion of a proton into a neutron and the emission of an electron-neutrino. The vacancy left by the electron is filled by an electron from a higher shell, leading for nuclei with high Z usually to the emission of characteristic X-rays. Besides the described modes of radioactive decay there

also exist more exotic ones. They usually occur at the limit of nuclear stability, i.e. in nuclei with an extreme excess of one type of nucleons. These modes are reviewed in [Pfü12].
As already mentioned, radioactive decay modes typically lead to excited states in the daughter nucleus. Their disintegration towards the ground state by gamma-ray emission or internal conversion is also often called radioactive decay, although it differs from the former types since it does not change Z and N. The de-excitation from an initial state with I_i to a final state with I_f by emitting a gamma-ray with multipole order ΔI needs to fulfill the selection rule

$$|I_i - I_f| \leq \Delta I \leq |I_i + I_f|. \tag{2.11}$$

The parity change $\Delta\Pi$ for an electric $E\{\Delta I\}$ transition is

$$\Delta\Pi = (-1)^{\Delta I} \tag{2.12}$$

and

$$\Delta\Pi = (-1)^{\Delta I+1} \tag{2.13}$$

for a magnetic $M\{\Delta I\}$ transition, each for multipole order ΔI. The transition probability $T_{if}^{\Delta I}$ for the decay from state I_i to state I_f by emitting a gamma-ray with energy E_γ is [Fir96]

$$T_{if}^{\Delta I} = \frac{8\pi(\Delta I+1)}{\hbar\Delta I[(2\Delta I+1)!!]^2} \cdot \left(\frac{E_\gamma}{\hbar c}\right)^{2\Delta I+1} \cdot B(\Delta I : I_i \rightarrow I_f) \tag{2.14}$$

where $B(\Delta I : I_i \rightarrow I_f)$ is the reduced nuclear matrix element. From Eq. 2.14 it is clear that the lowest allowed value of ΔI gives the highest transition probability. In addition, the transition probability is inverse proportional to the half-life of the de-excited level, thus states at low energies that can only de-excite by transitions with high ΔI values will have a longer half-life. A competing process for the de-excitation of nuclear states by gamma-ray emission is the internal conversion where the decay energy is transferred to an atomic electron that leaves the atom with an energy E_e

$$E_e = E_\gamma - B_e - E_{rec} \tag{2.15}$$

where B_e is the binding energy of the electron and E_{rec} the recoil energy of the nucleus. The latter is usually omitted since it only makes a small fraction of the energy. The fraction of internal conversion compared to gamma-ray emission increases as Z increases, the multipolarity increases and the transition energy decreases. The internal conversion is the reason why half-lives of excited states do not grow to infinity.

2.4. Isomeric states

Due to their many constituents nuclei do not only exist in one but many configurations or states. As in atomic physics the excited states yield information

about the internal structure. For example, nuclei with magic nucleon numbers have a first excited state at a large excitation energy compared to their neighbors. This is consistent with the stability found from binding energies for the ground states of magic nuclei.
In 1917, Soddy predicted nuclei identical with respect to mass and chemistry but different in terms of disintegration [Sod17]. This was described for the first time by [vW36] as long-living nuclear excited states ($t_{1/2} \gtrsim 1\,\mathrm{ns}$), also referred to as isomers, existing besides the ground state. Weizsäcker pointed out that they arise if the difference in total angular momentum to nuclear states with lower excitation energies is large, and thus a de-excitation by gamma-rays would be of high multipolarity. According to Eq. 2.14 the probability for such transitions is small and the state becomes metastable. This is often referred to as spin trap. Alternatively, the de-excitation of the state can be accompanied by a significant change in nuclear shape [WD01]. This is observed in very heavy nuclei where the non-spherical shape of the excited state hinders the transition to the spheroidal ground state. A third type of isomers is observed for example in the region with $N = 106$ and $Z = 72$. These nuclei are deformed and their states have to be described by another quantum number K which is the projection of the total angular momentum to the symmetry axis. The decay of excited states by gamma-ray emission is not hindered if the multipolarity of the decay radiation equals at least ΔK. For a large change in K radiation with high multipolarity and thus almost negligible transition probability is required. Instead the isomers decay by hindered transitions, and thus violate the K selection rule, see for example ^{180}Hf [WD99].

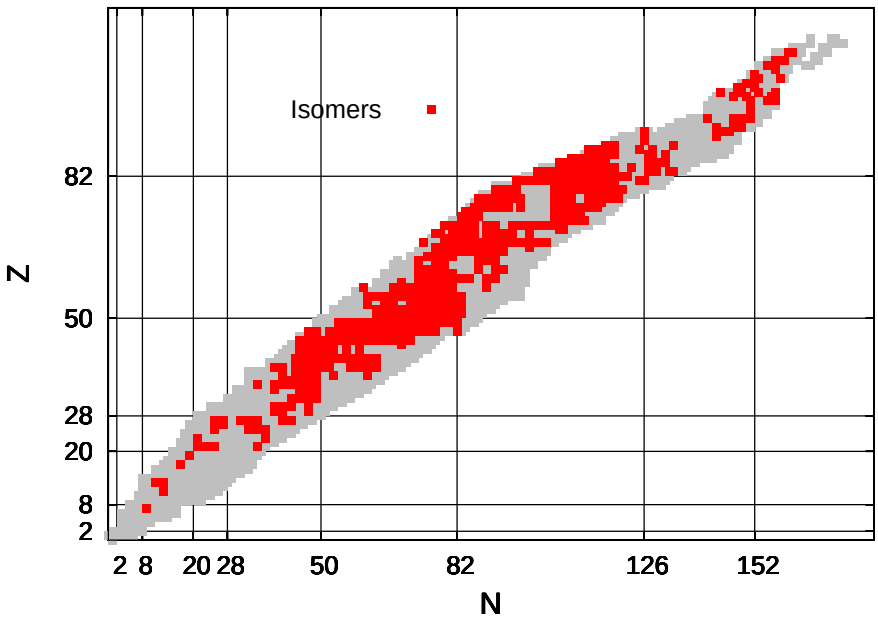

Figure 2.2: Distribution of isomers (red) on the nuclear chart with arbitrary half-life and excitation energy.

Isomers are distributed over the whole nuclear chart, as can be seen from Fig 2.2. Their excitation energy ranges from a few eV, as in ^{229m}Th, to a few MeV, as in ^{147m}Gd. The half-lives vary from a few ns, as in ^{212m}Po, to more than 10^{15}a, as in ^{180m}Ta. The latter is special since its half-life is much longer than that of the ground state ($t_{1/2} = 8.15\,\mathrm{h}$). In addition, it is the only naturally occurring isomer which makes it interesting for astrophysical research [Cea89, Bea99].
Isomers are interesting on their own since they are the only nuclear excited states that can be studied separately thanks to their half-lives and excitation energies. In addition, if their excitation energy is low they are most likely formed by single-particle excitations and thus they are ideal test cases for the shell model. Furthermore, by electromagnetic manipulation isomers give access to further excited states which may not be addressed by radioactive decays, see for example the photo-excitation of ^{180m}Ta [WDC01]. Thus, isomers are well suited for nuclear-structure studies. The practical benefit of isomers is for example the use of ^{99m}Tc for imaging during medical examinations. With respect to future applications, the aspect that isomers form energy traps is interesting. A controlled release of their energy which is linked to the question of new forms of energy storage and the realization of gamma-ray lasers [BS97, CC97] is subject of current research.

3. ISOLTRAP and the new decay station

For the measurements described in chapter 5 the high-precision Penning-trap mass spectrometer ISOLTRAP was used. It is located at the low-energy facility ISOLDE at CERN and typically reaches a precision of $\delta m/m = 10^{-8}$. With the relative resolving and purification power of $10^5 - 10^6$ even isomeric states at a few 100 keV excitation energy in exotic nuclei can be resolved and cleaned at the ISOLTRAP experiment. Such isomerical pure ion samples are well suited for nuclear spectroscopy and thus the ISOLTRAP mass-measurement system was extended by a decay-spectroscopy setup. In the following, the Penning trap mass spectrometer and the new system are presented in more detail.

3.1. Ion-beam production at ISOLDE

The radioactive ion-beam facility ISOLDE is located at the tangent of CERNs first and smallest circular proton accelerator - the PS Booster. In this stack of four synchrotrons the protons reach an energy of 1-1.4 GeV before they are branched off as very short high-intensity pulses to ISOLDE [iso12]. The proton beam hits a thick, heated target, for example made of uranium carbide, from which a wide variety of radioactive species is produced. Keeping the example, the uranium, consisting to 99.27% of the isotope ^{238}U, either undergoes spallation, meaning the main product is an atom with high Z, as the example in (3.1), or fragmentation as described in (3.2), where uranium is split into two atoms that differ a lot in Z. If the product atoms are similar in Z the process is called fission (3.3)

$$\mathrm{p} + ^{238}\mathrm{U} \longrightarrow ^{208}\mathrm{Fr} + \mathrm{Residuals} \tag{3.1}$$

$$\mathrm{p} + ^{238}\mathrm{U} \longrightarrow ^{11}\mathrm{Li} + \mathrm{X} + \mathrm{Residuals} \tag{3.2}$$

$$\mathrm{p} + ^{238}\mathrm{U} \longrightarrow ^{143}\mathrm{Cs} + \mathrm{Y} + \mathrm{Residuals} \tag{3.3}$$

where residuals can be several protons and neutrons. The produced atoms can be very exotic and with half-lives of only a few μs and below. The target is heated to about 2000°C and the nuclear-reaction products can diffuse out of the target into the ionization section. Since this process takes some time, until now only ion beams with half-lives of a few ms have been produced. There they undergo either surface ionization or hot plasma ionization, where the former can be combined with element-selective laser ionization using the Resonant Ionization Laser Ion Source (RILIS) setup [Fea08, Fea12]. During the ionization process, physical and chemical properties are exploited to achieve a high yield

of the desired nuclide and suppress unwanted contaminants. Afterwards, the ion beam is accelerated up to 60 keV and guided through the High Resolution Separator (HRS) or the General Purpose Separator (GPS), where it is mass-separated on-line by mass number A. The GPS consists of one 70°-bending magnet and reaches a resolving power of up to 2400 and the HRS consists of one 90°- and one 60°-bending magnet and can achieve a resolving power of up to 10^4 [Kug00]. The ion beam is finally delivered to one of the experimental beam lines in the experimental hall.

3.2. The ISOLTRAP setup

The ISOLTRAP experiment, as shown in Fig. 3.1, is a Penning-trap mass spectrometer located in the ISOLDE experimental hall [Mea08]. Mass measurements in Penning traps take advantage of the relation existing between the cyclotron frequency ν_c of an ion with mass m and charge q in a magnetic field B

$$\nu_c = \frac{1}{2\pi}\frac{q}{m} \cdot B, \tag{3.4}$$

as shown by [BG86]. In the following, the most relevant parts of the ISOLTRAP setup and the measurement technique will be described in more detail.

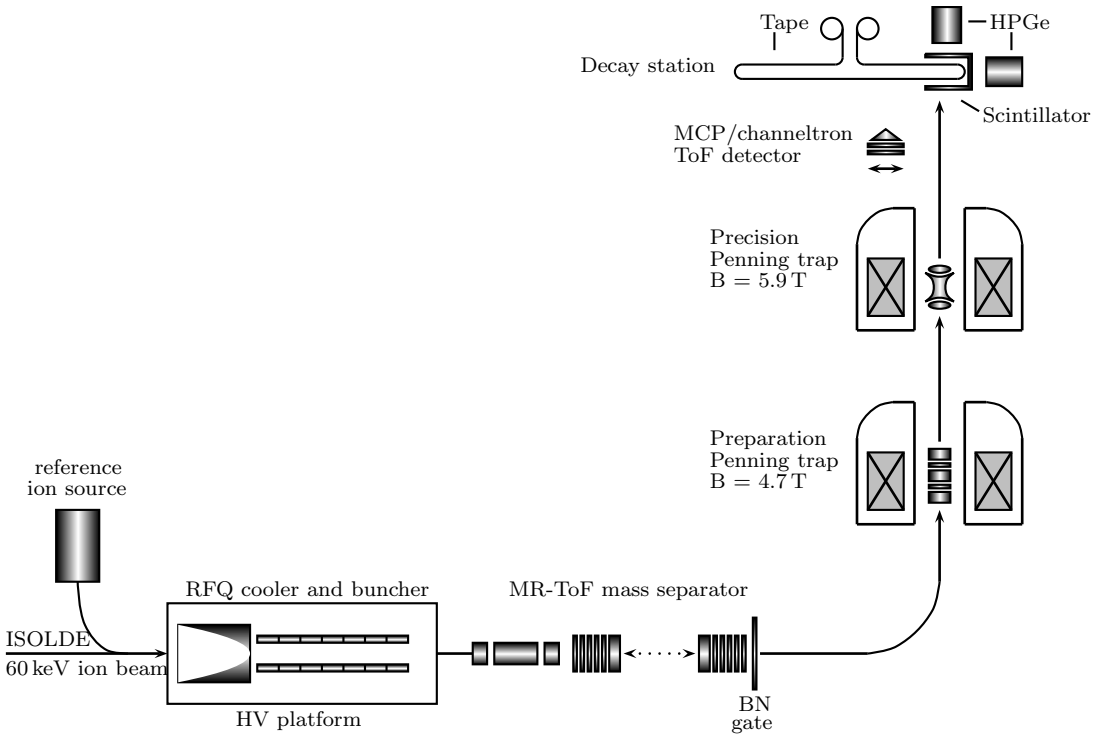

Figure 3.1: Scheme of the ISOLTRAP setup, which is used for mass measurements on exotic ion beams, and the decay-station extension.

3.2.1. The RFQ cooler and buncher

The beam coming from ISOLDE is a quasi-continuous beam with an energy of up to 60 keV. For mass measurements with Penning traps, small bunches of ions with low energy and low emittance are required. As a first step, the ion beam is decelerated electrostatically and injected into a linear radio-frequency quadrupole (RFQ) trap. The RFQ cooler and buncher is described in more detail in [Her01, Hea01]. It consists of four segmented rods to which radio-frequency voltages are applied for radial confinement. If, in addition, a potential gradient is created by applying different DC voltages U_{DC} along the axis, a three-dimensional well is spanned as can be seen from Fig. 3.2. The RFQ trap is filled with helium as buffer gas at a pressure of roughly 10^{-3} mbar thus leading to elastic collisions between the ions and the buffer-gas atoms where the kinetic energy of the ions is damped.

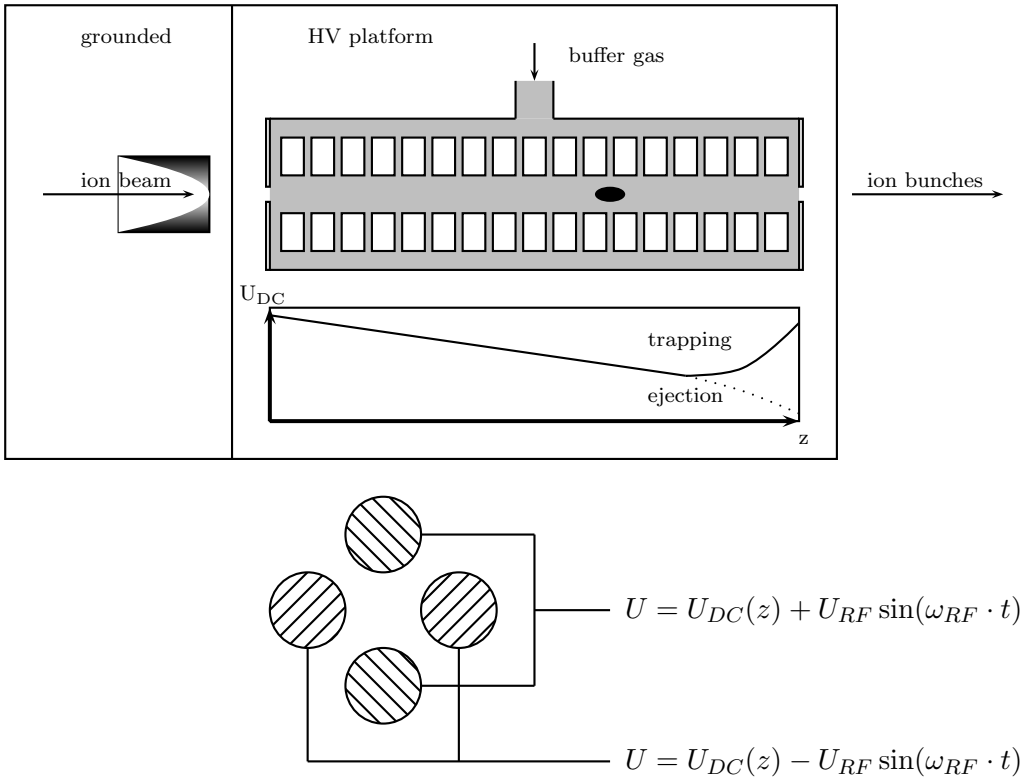

Figure 3.2: Top: Schematic side view of the radio-frequency trap which is used as a cooler and buncher at the ISOLTRAP setup. Bottom: Four rods with applied DC voltages and frequencies. Adapted from [Her01, Hea01].

According to [Sch08] the damping force can be described by

$$\mathbf{F} = -\delta\, m\mathbf{v} \tag{3.5}$$

where $m\mathbf{v}$ is the momentum of the ion and δ is the damping parameter. If μ is the ion mobility, q/m the charge-to-mass ratio of the ion and p and T are the pressure and temperature of the buffer gas in units of the normal pressure p_N and the normal temperature T_N, δ is given by

$$\delta = \frac{q}{m}\frac{1}{\mu}\frac{p/p_N}{T/T_N}. \tag{3.6}$$

After a storage time of some ms, the ions are in equilibrium with the buffer gas and have moved to the potential minimum. A large number of ions can thus be accumulated and ejected as ion bunches. Since the entrance electrode and the RFQ constitute a high-voltage platform, the ion bunch would re-accelerate to its initial energy after leaving this platform. This is avoided by a pulsed cavity that immediately follows the RFQ cooler and buncher and lowers the ion energy to roughly 3.1 keV. The switch that controls the drift tube voltage, has recently been re-designed within the PhD thesis of R. Wolf and is described in appendix C.

3.2.2. Multi-reflection time-of-flight mass separator

In 2010, a multi-reflection time-of-flight mass separator (MR-TOF-MS), as shown in Fig. 3.3, was installed at the ISOLTRAP experiment [Wea12b]. It constitutes the first step of purification of the ion bunches which usually consist of the ion of interest and isobaric as well as isomeric contaminations.

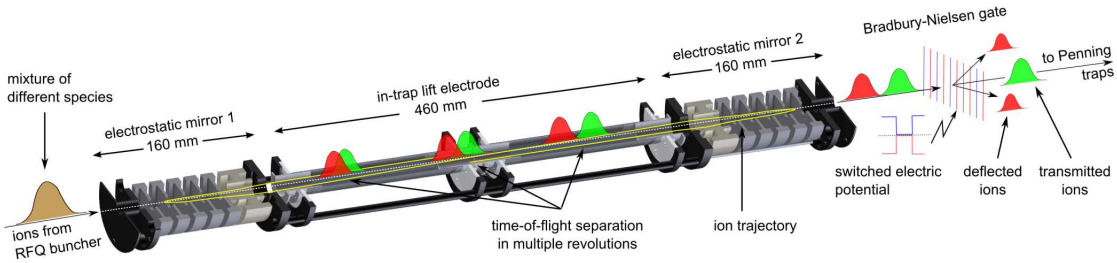

Figure 3.3: Sectional view of the multi reflection time of flight mass separator installed at ISOLTRAP. An ion bunch consisting of two species is injected and reflected several times between the two electrostatic mirrors. Thereby the two species get separated due to their different mass-to-charge ratios. After ejection, the contaminants are deflected by a Bradbury-Nielson gate. Taken from [Wea12b].

The principle of MR-TOF-MS is that ions with different mass-to-charge ratios but the same energy travel the same path within different times. Since it is not feasible to build a separator with the required dimensions for a time-of-flight separation of 1 μs the ion path must be folded. Thus, the ion beam is instead reflected several hundred or thousand times between mirror 1 and 2 in Fig. 3.3. After a certain number of revolutions the isobaric ensemble is separated spatially. The ions are extracted and the contaminant species are

deflected by a Bradbury-Nielson (BN) gate. In off-line measurements it was shown that this apparatus can deal with a contamination ratio up to 10^4 and reaches a mass-resolving power of $R = 10^5$ within only a few ms [Wea12b].

3.2.3. The preparation Penning trap

The purified ion bunch from the MR-TOF-MS is bent by 90° and guided to the first Penning trap of the ISOLTRAP experiment.

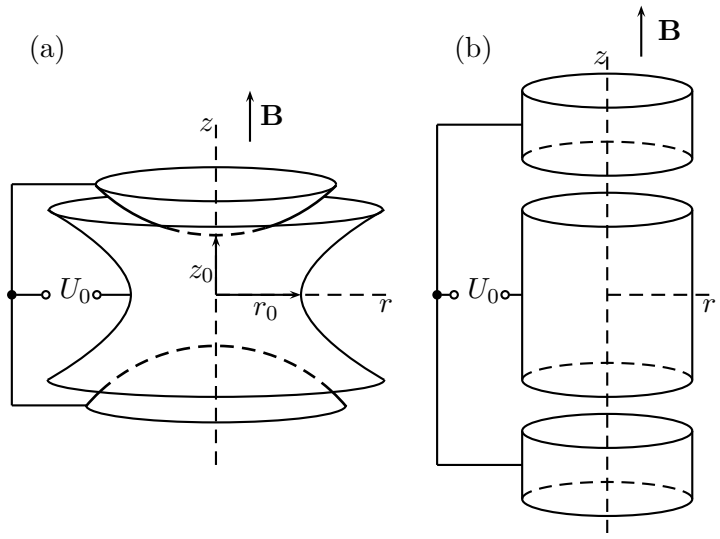

Figure 3.4: Schematics of a Penning trap in a) hyperbolic geometry and b) cylindric geometry. In addition, pairs of correction electrodes are used to approach an ideal quadrupole electrostatic potential.

An ideal Penning trap is the superposition of a weak azimuthal quadrupole potential with a strong homogeneous magnetic field that allows the confinement of a charged particle in all three dimensions. This is technically realized by a ring electrode and two end caps in cylindrical or hyperbolic geometry, see Fig. 3.4, placed in the interior of a superconducting magnet. The end caps have an opening to let the ion beam in and out. Thus, to approach an ideal quadrupole potential also correction electrodes are required. The ring electrode is usually segmented to apply dipole or quadrupole excitations for manipulation of the ion motion. The total motion of the ion in the trap, as it is shown in Fig. 3.5, is a superposition of three eigenmodes, namely the axial motion in z-direction with ω_z and the magnetron and reduced cyclotron motion in the radial plane with ω_- and ω_+. The theoretical description of the ion motion in a

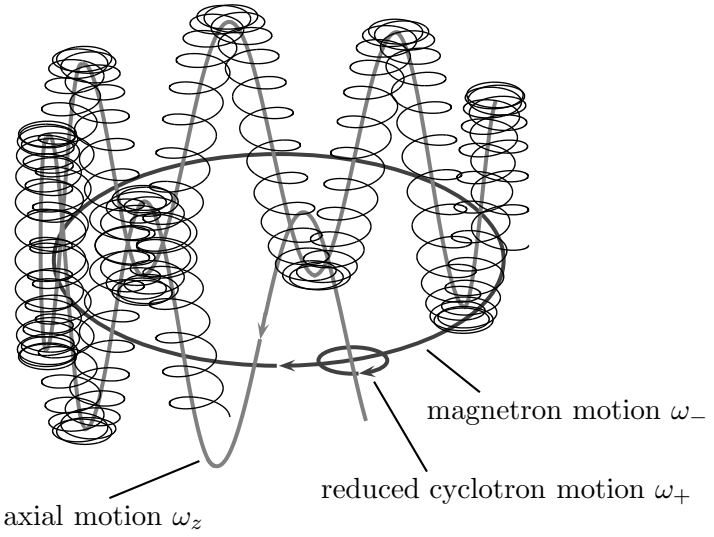

Figure 3.5: Sketch of the ion motion in a Penning trap. It is the superposition of the axial motion in z-direction, the magnetron and reduced cyclotron motion in the radial plane.

Penning trap, sketched in appendix A, gives the following important relations

$$\omega_- \approx \frac{U_0}{(r_0^2/2 + z_0^2) \cdot B} \tag{3.7}$$

$$\omega_c = \frac{q}{m} B = \omega_+ + \omega_- \tag{3.8}$$

$$\omega_- \ll \omega_+ \tag{3.9}$$

with U_0, r_0 and z_0 as in Fig. 3.4. Effects that are present in real Penning traps like field inhomogenities, ion-ion interaction or space charge are described for example in [MGW05]. However, it was shown in [Bea90] that the above relations all hold under the experimental conditions of the ISOLTRAP experiment within the experimental uncertainties.
The preparation trap of the ISOLTRAP experiment is a cylindrical trap which is filled with helium as a buffer gas at a pressure of $10^{-4} - 10^{-3}$ mbar and placed in a 4.7 T magnet [RHea97]. Like in the buncher, elastic scattering occurs and all eigenmotions of the ion are damped. For the magnetron motion the loss in energy results in an increase of the magnetron radius which can be seen from solving the equations of motion, see appendix A. The magnetron radius of all ions is even further increased by applying a dipole field with the magnetron frequency. This step is mass independent as can be seen from Eq. 3.7. After this second cooling step the ion motion consists only of a pure magnetron motion. By applying a quadrupole field with the cyclotron frequency ω_c the magnetron motion is fully converted to the reduced cyclotron motion for the desired ions. Since the radius of the reduced cyclotron motion decreases during buffer-gas

cooling the desired ions get centered in the trap [Sea91], see Fig. 3.6b. The centered ions can be then ejected through the ejection hole of the upper end cap with a diameter of only 1.5 mm. With the buffer-gas cooling method in this trap a mass resolving power of $R = 10^4 - 10^5$ can be achieved, but it takes a few hundreds of ms. If the MR-TOF-MS is instead used for the isobar separation, the measurement cycle can be shortened and thus shorter-lived species can be accessed.

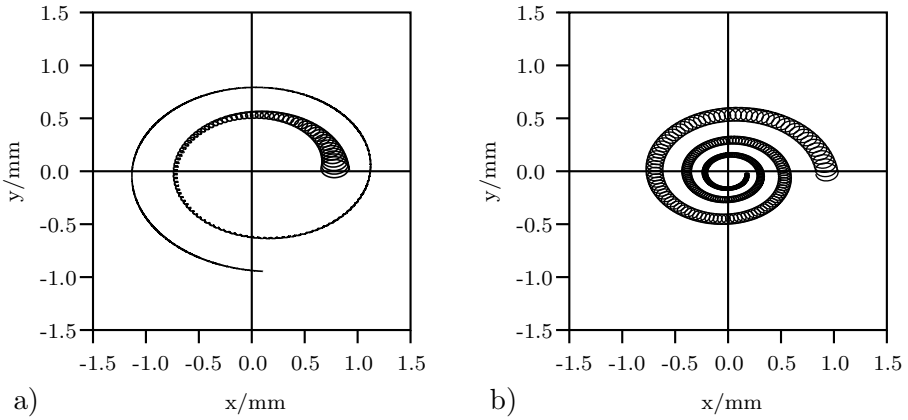

Figure 3.6: Simulation of the time evolution of the magnetron and reduced cyclotron motion in a Penning trap if a buffer gas is present and a) a dipole excitation with ω_- is applied, b) quadrupole excitation at ω_c is applied. In the latter case, the desired ions get centered [Sea91].

3.2.4. The precision Penning trap

The precision trap of the ISOLTRAP experiment is a hyperbolic Penning trap whereby the ring electrode is again segmented. It is operated in a 5.7 T magnet and a vacuum at 10^{-9} mbar [Bea90]. As soon as the ions get trapped, a dipole field at the ion magnetron frequency is applied to the ring electrode which leads to an increase of the magnetron radius. Sometimes the resolving power of the MR-TOF-MS and the preparation trap are not sufficient to remove all contaminations, like for example isomeric states with low excitation energies. In these cases a dipole field with the reduced cyclotron frequency of the contaminant is applied. The contaminant is then driven out of the trap. Afterwards, a quadrupole field at the cyclotron frequency is applied to the ring electrode, which again leads to a conversion from the magnetron motion to the reduced cyclotron motion for the desired ions, as it is shown in Fig. 3.7. The ions gain radial energy during this conversion. After a full conversion, when the energy gain is maximal, the excitation is stopped and the ions are smoothly ejected. As the ions leave the precision trap they travel through the gradient of the magnetic field and get accelerated due to the gradient force that is proportional to

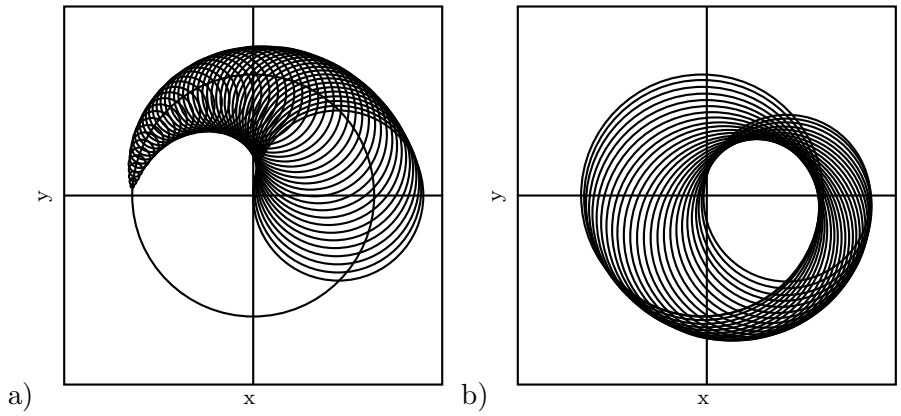

Figure 3.7: Simulation of the a) first half and b) second half of the conversion of the magnetron into the reduced cyclotron motion by applying a quadrupole excitation with ω_c. Adopted from [Bea90].

their orbital magnetic moment and thus their initial radial energy E_r

$$\mathbf{F} = -\boldsymbol{\mu}(\nabla \cdot \mathbf{B}) = -\frac{E_r}{B}\frac{\partial B}{\partial z}\mathbf{e_z}. \tag{3.10}$$

The time from the ejection from the trap to the detection at a micro-channel plate detector (MCP), compare Fig. 3.1, is measured. To determine the cyclotron frequency of the ion of interest the above described cycle is applied several times while scanning the frequency ν_q of the quadrupole excitation in the precision trap and recording the corresponding time of flight (TOF). Since for non-resonant excitations the gain in radial energy is smaller, the ions arrive later at the detector. An example of the resulting TOF-resonance is shown in Fig. 3.8 for ^{133}Cs. This measurement technique used at ISOLTRAP [Kea95] is a destructive one where the ions are lost after detection. The time of flight from the trap center ($z = 0$) to the detector ($z = z_1$) is given by

$$T(\nu_q) = \int_0^{z_1} \sqrt{\frac{m}{2(E_0 - qU(z) - \mu(\nu_q)B(z))}}\,\mathrm{d}z \tag{3.11}$$

with E_0 is the initial axial energy of the ion, μ the orbital magnetic moment of the ion and the electric and magnetic potential differences $U(z)$ and $B(z)$ along the path. By varying Eq. 3.11 with respect to the quadrupole frequency, the theoretical line shape is obtained [Kea95]. This is then used to fit the experimental data. The resolving power of this trap depends on the duration T_q of the quadrupole excitation as $R \sim \nu_q \cdot T_q$ [Bea96]. A typical value for $A = 100$ is $R = 10^5 - 10^6$.
The results from mass measurements with Penning traps are rather given as frequency ratios with respect to a well known reference mass m_{ref} lying as close

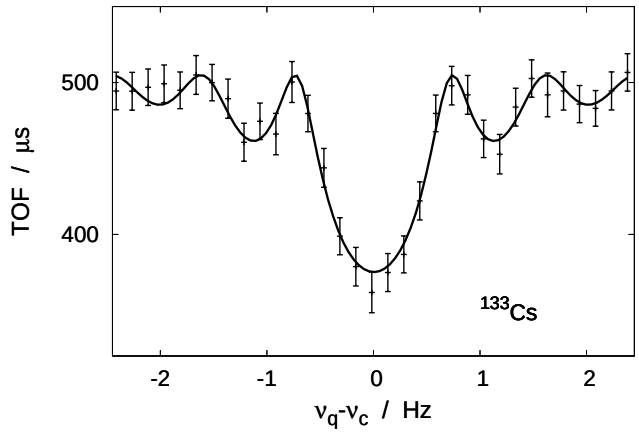

Figure 3.8: Time-of-flight resonance of ^{133}Cs. The quadrupole excitation was applied for T_q=1.2 s.

as possible in mass. The mass itself can be then obtained by

$$m_{\mathrm{meas}} = \frac{\nu_{\mathrm{ref}}}{\nu_{\mathrm{meas}}} \cdot (m_{\mathrm{ref}} - m_e) + m_e \tag{3.12}$$

where m_e is the electron mass.

3.3. The decay-station setup

As already mentioned, ion beams produced at the ISOLDE facility usually contain isobaric and isomeric contaminations beside the ion of interest. Especially nuclear decay spectroscopy is hampered by those contaminations and can therefore benefit from a setup for beam purification, such as the Penning-trap mass spectrometer ISOLTRAP. Within the precision trap, as presented in the previous section, mass differences down to several 100 keV can be resolved. Thus, it allows to distinguish the ion of interest and contaminating species. An illustrative example is ^{68}Cu [Bea04] where clearly two minima corresponding to two different states are observed in the upper part of Fig. 3.9. It follows from equation 3.4 that the right minimum corresponds to the lighter mass and thus to the ground state and the left minimum corresponds to the isomeric state. Since the spin states for the ground and isomeric states are well known an assignment of the TOF minima to them was also possible.
Usually, either the spin-state assignment of the ground and isomeric states in exotic nuclei or the decay pattern is not known. This information can be obtained by nuclear decay spectroscopy on pure samples. The ISOLTRAP experiment is capable to deliver pure ion samples, as can be seen from the lower part of Fig. 3.9. Thus, by adding a decay-spectroscopy system behind the ISOLTRAP Penning traps, more information to characterize for example isomeric states in exotic nuclei is accessible. In addition, contaminations can be

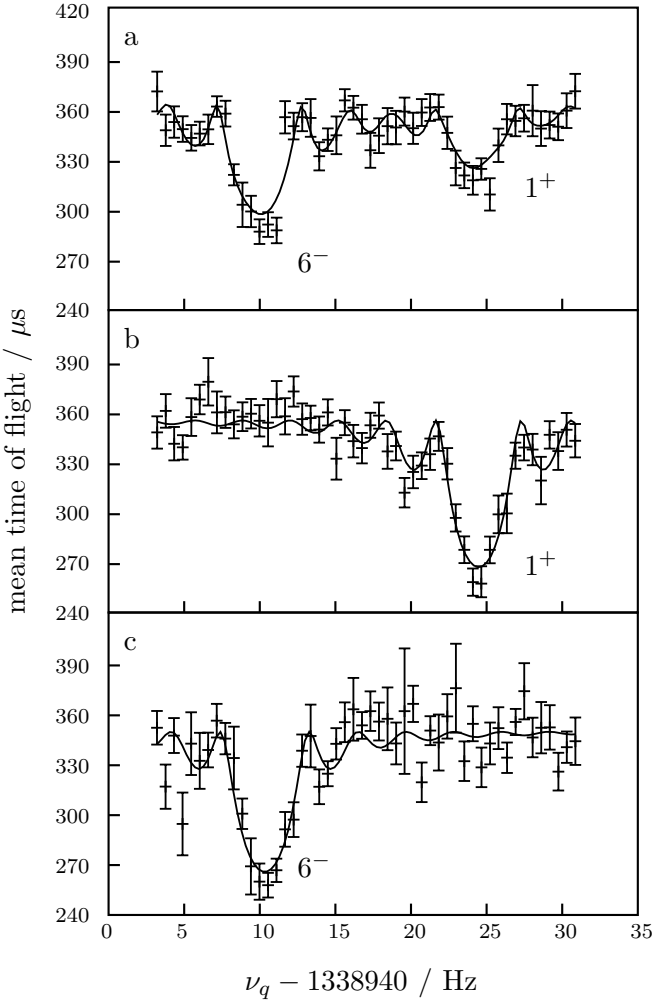

Figure 3.9: Time-of-flight resonance of ^{68}Cu where a) the ground and isomeric state are clearly resolved, b) the ground state was isolated and c) the isomeric state was isolated. Adopted from [Bea04].

present in the Penning traps that are not easily identified. In those cases, decay spectroscopy can help to identify the species that are ejected from the Penning trap. Thus, by combining the production of pure samples with immediate nuclear decay spectroscopy two new methods become available, namely trap-assisted decay spectroscopy and decay-assisted mass measurements. For the decay-spectroscopy measurements, a decay-station system was installed behind the precision Penning trap, which can be connected to the trap by the ion optics shown in Fig. 3.10.

The system is described in detail in [Kea12], where also results from first off-line and on-line studies are presented. As will be shown, the system is well suited for β-decay spectroscopy. For measurements which aim at a deeper understanding of α-decaying nuclei, as suggested in [Cea11], an alternative system using very

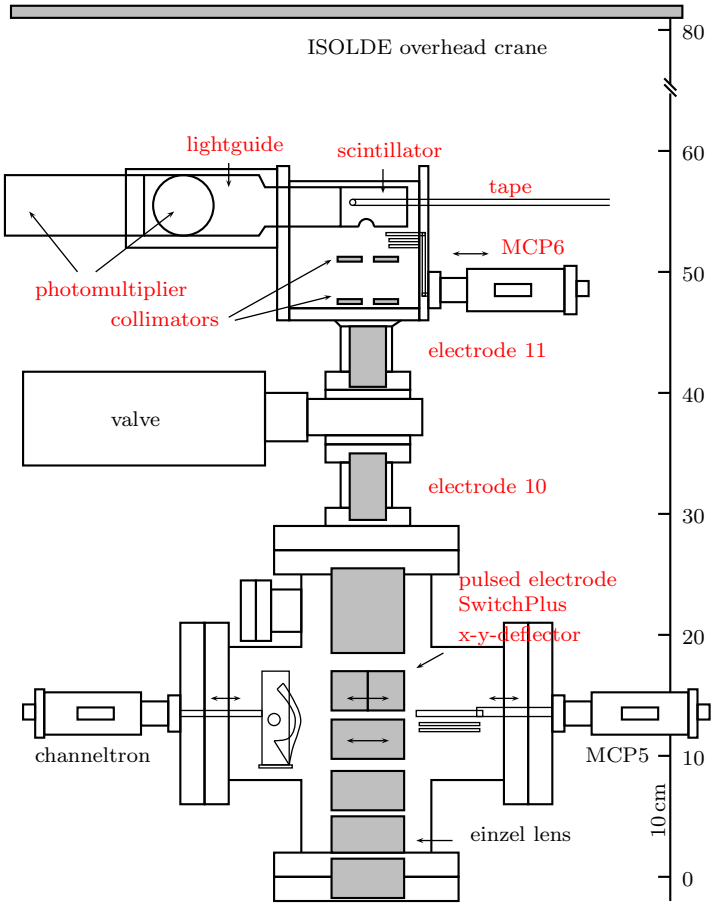

Figure 3.10: Schematic view of the decay-station setup that was installed after the precision trap of the ISOLTRAP experiment. The MCP which is usually used for mass measurements (MCP5) is replaced by a deflector on a mechanical feedthrough. The ions can then pass the SwitchPlus electrode for re-acceleration and can be implanted into the tape inside the decay chamber. Ion optics to access the decay-station and parts of the decay station are marked in red. Figure adopted from [Kea12]

thin foils can be attached to the ISOLTRAP setup instead of this tape system. In the following, a description of the decay-station system like it was used for the measurements on neutron-deficient thallium isotopes in 2010 and 2011 is given. In 2012, the decay-station system was used as a stand-alone experiment for nuclear decay spectroscopy on neutron-rich hafnium isotopes, see [Wea12a, Woo14]. This was possible thanks to its compact and thus portable design. All upgrades which were implemented until this measurement will also be presented.

3.3.1. The setup for measurements in 2010

As described in the previous section, the ion time-of-flight for mass measurements is measured with a detector placed behind the precision trap, MCP5

in Fig. 3.10. To perform decay spectroscopy on pure samples a decay-station system has to be attached also behind the precision trap. To access this decay-station system, several modifications to the ISOLTRAP beam line were required. The main modification was the installation of a switchable electrode (SwitchPlus), see Fig. 3.10. It allows to re-accelerate the ions, ejected from the trap with an energy of only a few eV, to several keV. This increase in energy is needed to implant the ions into the tape at a depth where they cannot diffuse out before decaying. The decay station itself consists of a decay chamber that houses a collimator to limit the size of the implanted sample and a MCP detector for the diagnostics. The main element placed inside the chamber is the end of a movable tape, perpendicular to the ion path, see Fig. 3.10 and 3.11. Usually, in exotic nuclei the daughter nuclei are radioactive as well and give rise to unwanted background. The tape allows to remove this daughter activity before implanting a new sample. For the detection of the nuclear decay, suitable detectors for β- and γ-decay must be arranged around the implantation point on the tape.

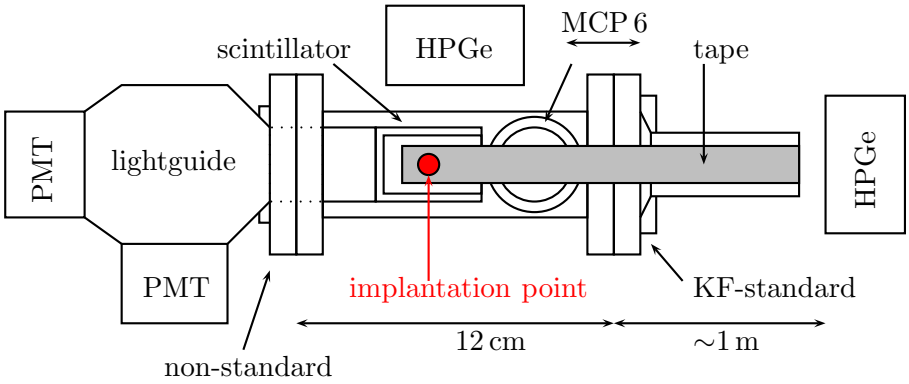

Figure 3.11: Top view of the decay-station system that was used in 2010, not to scale.

The decay-station setup at the ISOLTRAP experiment as well as the required ion optics were built in 2009 and are described in [Nai10, Kea12] and shown in Fig. 3.10. The pulsed electrode can be switched from -1.2 kV up to 15 kV within less than 1 μs. Due to limited space it is 7 cm long, which is just long enough to fit an ion-bunch of 1 μs time-width [Kea12]. After the ion-bunch is re-accelerated by this electrode, its diameter is limited by one or two collimators with an opening diameter of 5 mm. For the optimization of the ion transmission, a MCP of 2.5 cm diameter, placed at the end of a mechanical feedthrough, can be moved into the ion path behind the collimators (MCP 6 in Fig. 3.11). Since 2010, an aluminized Mylar® tape of 12 mm width is used for the ion implantation. It replaces the previous tape which had an effective width of only 4 mm. It is driven by a step motor that is magnetically coupled to the tape spools and can move the daughter activity either to another observation point or to the tape box. The tape movement can be reproduced with 5 mm precision. Although this is less precise than the previous system, it was proven

in 2012 that it is sufficient to run a second, fully instrumented decay chamber. In the implantation area the tape is surrounded by a 5 cm long and 2 mm thin plastic-scintillator tube of BC408 which is sensitive to β-particles. The scintillator is connected to a light guide that distributes the scintillation light to two photomultipliers (PMT) of type XP2262B perpendicular to each other and shielded by mu-metal from the residual magnetic field of the precision-trap magnet. The scintillator and the light guide are covered with reflective paint BC620 and aluminum foil to minimize the loss of scintillation light. All described parts are housed in a decay chamber made of aluminum. Since 2010, the inner part of the chamber can be easily accessed through the scintillator or tape connection plate in case of technical interruptions or efficiency calibrations. The side walls of this chamber are only 1 mm thin and thus allow gamma-ray detection outside the vacuum by high-purity germanium (HPGe) detectors. A sketch of the described system is shown in Fig. 3.11. The HPGe detector used at the implantation point in 2010 was a n-type Eurisys EGC 70 TR with a relative efficiency of 73%. The detector combination at the implantation point allows to study single γ-spectra and β-γ-coincidences. At the observation point, to which long-living samples can be moved, a second HPGe detector of n-type Canberra GC 7020 with relative efficiency of 55% was placed. All signals and the corresponding time stamps from the two HPGe detectors, the two PMTs and the trap ejection pulse were recorded by two 40 MHz Xia DGF-4C modules [xia12] and analyzed afterwards off-line, for details on the control commands see appendix B and for the data analysis see section 5.1. As the described system must be directly connected to the mass-measurement setup, the tape and the scintillator must be operated under vacuum that is in the ideal case either the same as in the mass-measurement section (10^{-9} mbar) or is separated by a differential pumping section. A vacuum comparable to the mass-measurement section was not reached due to the fact that the connections of the tape and the PMTs to the decay chamber were either non-standard vacuum components or only of KF-standard and that the tape and the scintillator consist of outgassing material. While testing a pumping barrier high transmission losses were observed, thus it was not implemented in the beam line. A differential pumping section by spatial separation of the two setups was not implemented due to geometrical constraints imposed by the ISOLDE overhead crane, as can be seen from Fig. 3.10. Under these circumstances a vacuum of only $3 \cdot 10^{-5}$ mbar was achieved with one turbo pump in the decay-station section. During the mass measurements the two sections were thus separated by an ultra high vacuum valve which was opened only for the decay measurements. A subsequent pumping time of roughly one hour was required to reconstitute the high-precision mass-measurement conditions.

3.3.2. The setup for measurements in 2011

In 2011 it was attempted to improve the vacuum in the decay chamber. For this purpose, a new connection between the decay chamber and the tape guidance based on CF-vacuum components was built as compared to formerly used KF-standard vacuum components, see Fig. 3.11. Furthermore, a second turbo pump

was installed close to the decay chamber. As a result, the vacuum was improved by one order of magnitude to 10^{-6} mbar. Since the measurements in 2010 were hampered by vibrations of the experimental platform as well as by electronic noise, effort was also made to decouple the detectors from the platform by damping material and to lower the electronic noise by additional shielding of the signal cables.

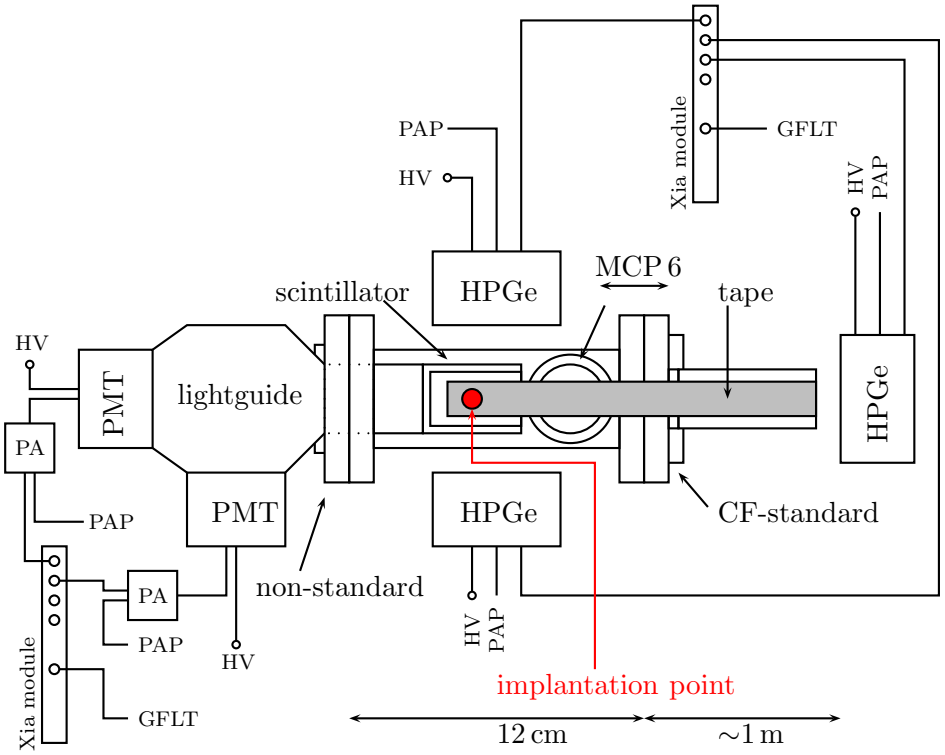

Figure 3.12: Top view of the decay-station system that was used in 2011, not to scale. Each detector signal goes through a pre-amplifier (PA) with a power supply (PAP) before entering the data-acquisition system.

To also study γ-γ-coincidences a second HPGe detector was placed at 180° with respect to the other HPGe detector at the implantation point, see Fig. 3.12. The detectors used were a 32% p-type Ortec GEM30P4-76, a 70% n-type Canberra GC 7023 at the implantation point and a 55% n-type Canberra GC 7020 HPGe detector at the observation point. All signals and the corresponding time stamps of the HPGe detectors, the PMTs, the trap ejection and the tape movement were again recorded by Xia module [xia12], see Fig. 3.12. To record data the General First Level Trigger (GFLT) input of the modules must be enabled (logic 1). If the data acquisition should stop, for example while the tape is moving, this input must be disabled (logic 0). The tape-control module helps to set this input properly. The tape can either move stepwise on a defined distance or continuously until the end of the tape is reached. The first mode can be controlled either manually (MEOT/MBOT) or by an external trigger (XEOT/XBOT). The external trigger must provide a positive signal with a

width of at least 300 ms to enable the tape movement. The tape-control module provides then a positive output signal (BUSY) while the tape is moving. This output can be used together with the external trigger to control the GFLT and thus the data acquisition as it is shown in Tab. 3.1.

trigger	BUSY	NOR = GFLT	DAQ	remark
1	0	0	no	tape movement triggered
1	1	0	no	tape movement started
0	1	0	no	tape movement
0	0	1	yes	no tape movement

Table 3.1: Logic table for a NOR gate which uses the external trigger signal and the BUSY signal from the tape controller as input. The output of this gate is then connected to the GFLT input of the Xia modules.

The events themselves are recorded in list mode in a local buffer of the Xia modules that is written to a data file whenever the buffer is entirely filled. The binary data files can be converted and analyzed off-line.

3.3.3. Requirements on the measurement cycle

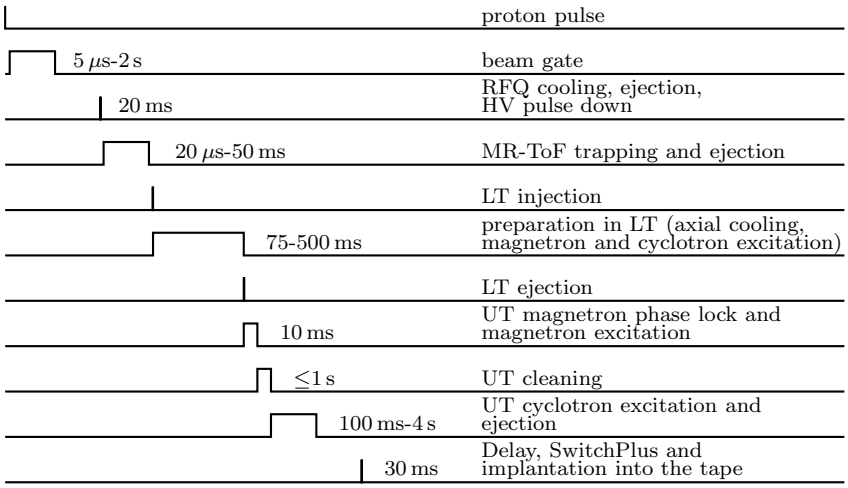

Figure 3.13: A typical cycle for decay spectroscopy at the ISOLTRAP experiment. The steps up to the ejection from the precision (upper) trap (UT) are the same as for the mass-measurement cycle. LT stands for preparation (lower) trap.

A typical cycle for the decay spectroscopy is shown in Fig. 3.13. All steps until the ejection from the precision trap are the same as for a typical mass-measurement cycle. Compared to the mass-measurement cycle the ions are ejected much faster from the trap so they can reach the SwitchPlus electrode as an ion bunch that is narrow enough to be switched within the time window of the

cavity. Therefore the potentials of all drift tubes behind the precision trap had to be changed. In addition, the MCP for the mass measurements was replaced by a focusing electrode (x-y deflector in Fig. 3.10). The SwitchPlus electrode is lifted from -1 kV to 15 kV to re-accelerate the ion sample and subsequently implant it into the tape.

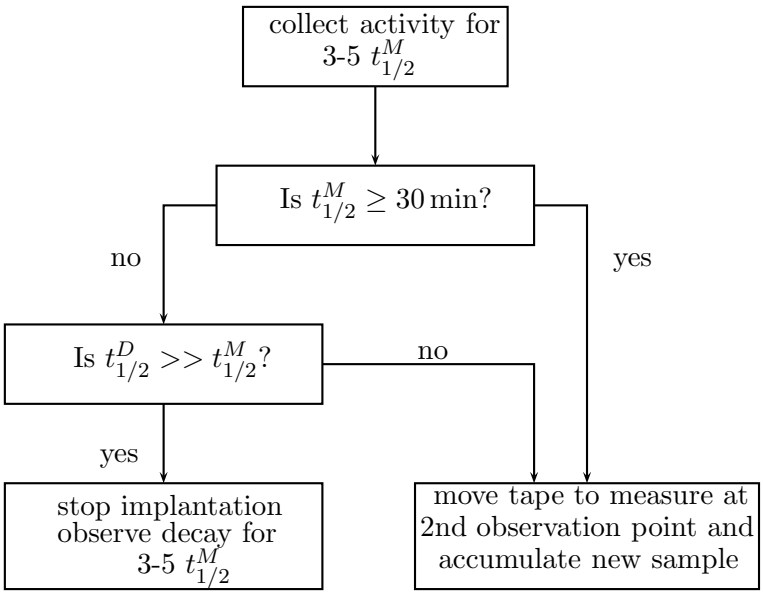

Figure 3.14: ISOLTRAP decay-station operation depending on the half-life of the mother $t^M_{1/2}$ and daughter nucleus $t^D_{1/2}$. The most right branch is mainly motivated by an efficient usage of the radioactive beam. If the time to switch between the mass-measurement and the decay-measurement mode can be decreased to a few minutes there might be an option to measure masses while the sample is decaying.

Besides the adjustment of the potentials behind the precision trap several timings of the measurement cycle have to be adjusted to the requirements of decay spectroscopy. Usually, the number of ions in one ion bunch, which is determined by the length of the ISOLDE beam gate and the production yield, has to be increased such that enough statistics can be collected in a reasonable time. This conflicts with the optimal trapping and cleaning conditions of the ISOLTRAP Penning traps that favor fewer ions. Thus, one has to choose the size of the ion sample such that the trapping and possible contaminant cleaning are still efficient. Furthermore, the times of the dipole excitation, to remove contaminations, and the cyclotron excitation in the precision trap have to be adapted, such that the ions are not driven out of their path to the tape due to the interaction with the magnetic field. Finally, the half-life $t_{1/2}$ of the nuclide under investigation is a limiting factor for the whole cycle. It must be long enough that most of the nuclei pass the cycle without decaying. Thus, very short-lived species are not accessible with the decay station. As a rule of thumb the ratio between the half-life and the cycle length should be at least

2-3. Then activity is built up with each implantation and after approximately 5 $t_{1/2}$ an equilibrium between formation and decay has formed and the saturation activity is reached. Depending on the half-life of mother and daughter nucleus, $t^M_{1/2}$ and $t^D_{1/2}$ respectively, either the implantation is stopped or the sample is moved to the second observation point, as shown in Fig. 3.14. In the case when $t^M_{1/2}$ is long ($t^M_{1/2} \gtrsim 30\,\text{min}$) a new sample at the implantation point can be immediately accumulated. It is important to keep in mind that for the measurements from 2010 and 2011 a tape movement was equivalent to the loss of coincidence information since the observation point was only equipped with one HPGe detector.

3.3.4. The mobile decay station

In 2012, the decay station has proven to be not only an extension of an existing experimental setup but to be a stand-alone apparatus. As already mentioned, it is well suited to study single gamma-rays as well as β-γ and γ-γ-coincidences. If the ion beam of interest is free from contaminations, the decay-station does not need to be placed behind the ISOLTRAP Penning traps and it can be used at another ISOLDE beam line. This is easily done thanks to the compactness of the whole system.

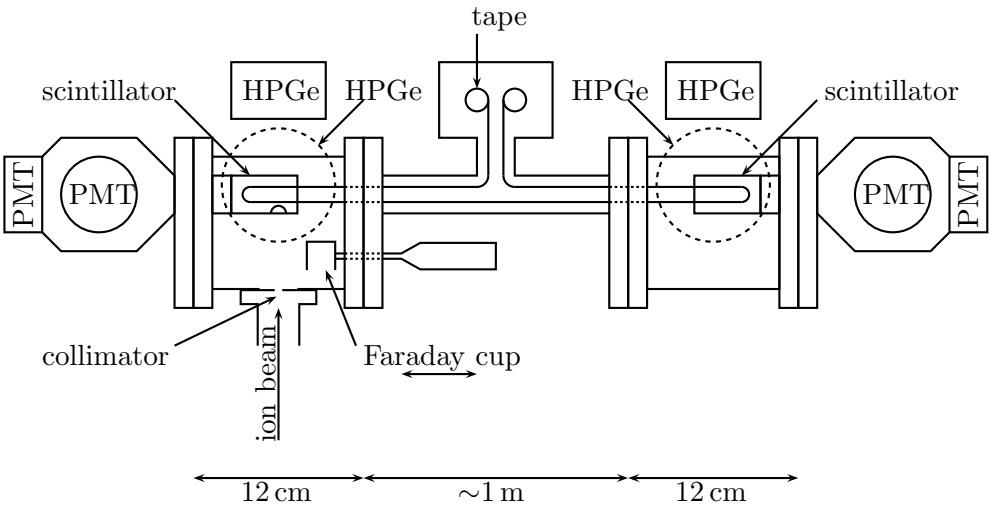

Figure 3.15: Scheme of the portable decay station which was used in 2012 as a stand-alone system. For easier beam tuning with stable ions the MCP detector was replaced by a Faraday cup. At this occasion a second decay chamber was added. This allows to study single gamma-rays, β-γ and γ-γ-coincidences at two positions simultaneously.

In the above configuration, see Fig. 3.15 a quasi-continuous ion-beam at up to 60 keV is directly implanted into the tape. Before entering the decay chamber the ion beam passes through a collimator with a diameter of 2 mm. The implantation point is again surrounded by the thin plastic scintillator and by two HPGe detectors. The angle between the two HPGe detectors was changed to

90° to avoid backscattering effects. Thus, one of the detectors is facing the top wall of the decay chamber which is also of 1 mm width. The main modification is the possibility to attach a second decay chamber that is in principle a copy of the first one. Inside this chamber the tape holder is also surrounded by a 5 cm long and 2 mm thin plastic scintillator of BC408 that is glued to a light guide, distributing the scintillation light to two PMTs. In principle, the side walls and the top wall of the aluminum chamber, that are only 1 mm thick, can be faced by HPGe detectors. Thus, this new chamber comprises a second fully instrumented decay-spectroscopy system. During the measurements on neutron-rich hafnium isotopes [Wea12a] it was shown that the tape can be moved such that the sample is transported from one decay chamber to another. Still, there is an uncertainty in the positioning of the sample because of the limited precision of the tape movement. This affects the efficiency calibration of the second decay-spectroscopy system. The uncertainty on the efficiency calibration however can be estimated by Geant4 simulations [gea12]. The big advantage of a second decay chamber is that one collects more statistics in the same time, since coincidence information from moved samples is no longer lost.

4. Simulations for efficiency studies

For the decay-station system several simulations were performed. First, it was intended to optimize the ion transmission to the decay chamber. Thus, the ion transport between the precision trap and the implantation point was simulated using the ion-trajectory program SIMION® [sim12]. Second, the feasibility of an ion bender which is an option to circumvent the constraints in height was also studied with this program. Third, the detection efficiency of the decay-spectroscopy setup was studied with the toolkit Geant4 [gea12]. In the following, each simulation and the obtained results are explained in more detail.

4.1. Transport efficiency

The ion optics for the ion transport, re-acceleration and implantation of the ions into the tape after the precision trap were chosen in 2009 [Nai10]. To study the transport efficiency by considering also a collimator, simulations with the ion-trajectory program SIMION® version 8.0.8.1 were made.

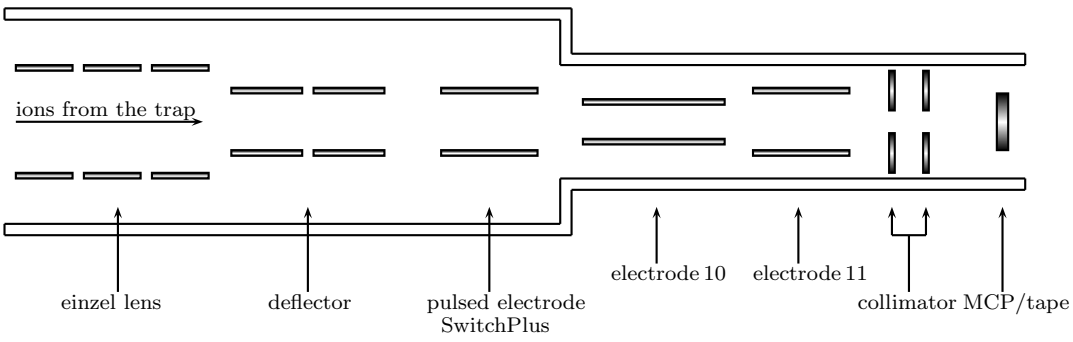

Figure 4.1: Electrode geometry implemented in SIMION for ion-transport, re-acceleration and implantation into the tape. Only the part that is different to the mass-measurement mode is shown. The deflector replaces the MCP that is used during mass measurements. The SwitchPlus electrode re-accelerates the ions. Electrode 10 and 11 are aimed at further focusing. Before the implantation into the tape, the radius of the ions is reduced by one or two collimators.

SIMION uses potential arrays to model the electric and magnetic fields. Thus, one potential array based on the electrode configuration, as shown in Fig. 4.1,

and one potential array representing the measured magnetic field are considered in the program. For decay-station studies, the MCP detector used for mass measurements is replaced by a deflector that guides the ions to the pulsed electrode SwitchPlus for re-acceleration. Behind the SwitchPlus electrode, two further electrodes are placed, aimed for further focusing of the ions. In addition, one or two collimators, ensuring a small enough ion bunch implanted into the tape, can be placed.
The fringe magnetic field of the ISOLTRAP superconducting magnet housing the precision trap was measured [Bor12]. A SIMION potential array was created to fit to the measured field allowing a maximal deviation, between simulation and data, of 10%. The result is shown in Fig. 4.2.

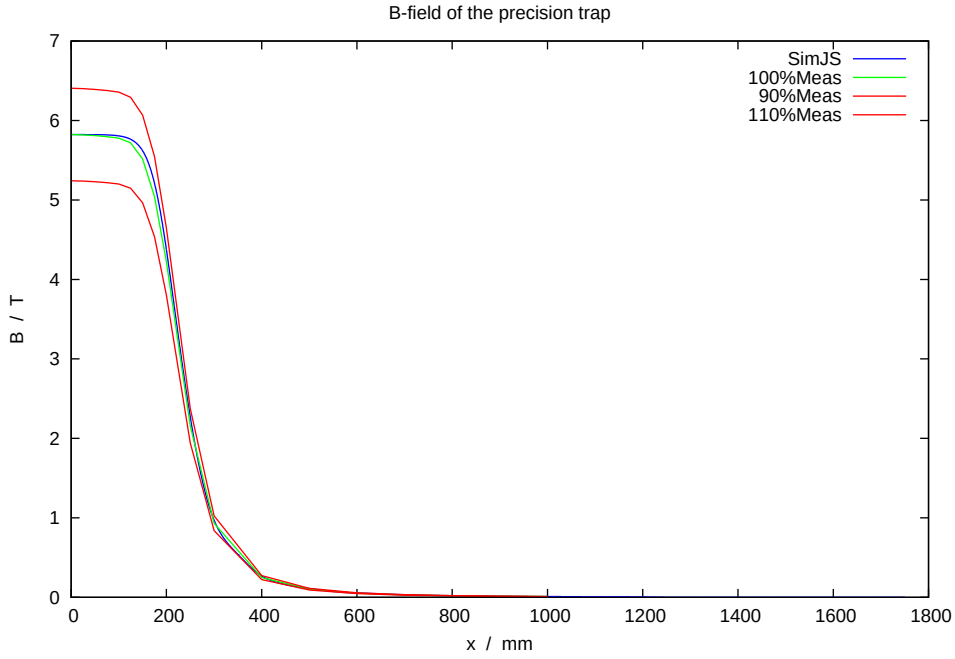

Figure 4.2: Magnetic field implemented in SIMION (blue) compared to the measured field (green). Also the 10% deviance band is shown (red).

In addition to the implementation of the electrode geometry and the magnetic field, the starting conditions for the ions have to be fixed. They are determined by the ion-cloud properties and its motion in the trap, due to excitations, and the extraction mode. During the mass-measurement mode the ions are ejected slowly from the precision trap and they drift through the gradient of the magnetic field, where their radial energy, gained during the excitation in the trap, is fully converted into axial kinetic energy. As a result their time-of-flight spread is 20-30 μs and their radius is rather large. These two features are not compatible with the decay-station mode since they result in transmission losses at the fast-switched electrode and on the collimator. Therefore, in the decay-spectroscopy mode all ions should be re-accelerated within a short time window and subsequently implanted into the tape. The ions are therefore ejected fast from the

trap. The simulation of the ion trajectories starts just after the ejection of the ions from the precision trap. Thus, an ion set with the momenta and energies corresponding to this ejection mode must be provided. One suitable set of ions, with $A = 133$, was created by the CERN summer student Jeremie Herterbreau. The potential arrays are then superimposed spatially, such that the real measurement conditions are reflected, and stored with the set of ions in a SIMION workbench. This workbench allows some user interaction, for example the voltage on each electrode can be fast adjusted. Only then, the field at each point of the geometry is calculated. When the ions are started, the equations of motion are solved using a Runge-Kutta method and the ion trajectories are calculated. To optimize this setup, potential values and switching time that maximize the number of ions transmitted to the tape have to be found. This can be done by an optimization program, based in the simplest case on the Lua programming language [lua12]. The optimization is a quite complex task since at least 11 voltages have to be scanned and in addition, the time when to switch the pulsed electrode SwitchPlus depends on these voltages. It was decided to fix the time when the potential at the SwitchPlus electrode is lifted. The optimization procedure contains then a simplex-optimization method for the voltages on the electrodes before the SwitchPlus electrode. The simplex algorithm requires starting values and step sizes for potential changes for each electrode. Furthermore, a function must be defined that is minimized with respect to the scanned values. The switch voltage U_S is defined as

$$U_S(t) = -(U_f - U_i) \cdot e^{-(t-t_S)} + U_f \qquad t \geq t_S \tag{4.1}$$

with U_i and U_f the initial and final value of the SwitchPlus electrode in volts and t_S the switch time in microseconds. Then the potential on the SwitchPlus electrode is lifted within $1\,\mu$s, as stated in [Kea12]. After a given number of steps, the program returns a set of voltages that represents a local minimum in the neighborhood of the starting values. By changing the starting values and the step size, other local minima can be found. This already shows the limits of the algorithm.
As one example, an arbitrary set of voltages (set A), see Tab. 4.1, with step size $\pm 10\,$V was used as initial set, yielding a transmission efficiency of already 59%. The program minimized the expression

$$f(N_s, N_d, v_y, v_z) = (N_s - N_d) + \sqrt{v_y^2 + v_z^2} \tag{4.2}$$

with N_s the number of stopped ions, N_d the number of ions transmitted to the tape and v_y and v_z the velocity components perpendicular to the ion motion. After 100 simulation steps a set of voltages with a transmission efficiency of 92% (set A') was obtained. The ions which were not transmitted to the tape were all lost at the collimator. In one simulation, the opening diameter of the collimator was thus increased by 1 mm, yielding a transmission efficiency of 100%. This slightly increased diameter would still yield a well-located sample on the tape.
To improve the ion transmission to the decay chamber, a direct comparison

electrode	set A	set A'	set B	set B'
einzel lens 1	-300	-297.695	-300	-292.5
einzel lens 2	-1325	-1340.604	-1000	-1000
einzel lens 3	-300	-297.695	-300	-292.5
deflector 1	-900	-907.146	-1000	-1000
deflector 2	-900	-882.853	-970	-970
SwitchPlus	-1200/15000	-1200/15000	-1200/15000	-1200/15000
electrode 10	-1000	-1000	-1000	1000
electrode 11	-1000	-1000	0	0

Table 4.1: Initial and optimized voltages in volts on the elements shown in Fig. 4.1. For details see text.

between the simulations and the measurements is needed. This is challenging since during the measurements the ion counts are compared between two detectors (MCP 5 and MCP 6 in Fig. 3.10) whose efficiencies are not known. Furthermore, the x-y-deflector, see Fig. 4.1, mounted on a mechanical feedthrough has to replace the first detector (MCP5) while using the second (MCP6) for ion detection, thus leading to slightly changed potentials with each replacement.
The set of optimized values from the beam time in 2011 (set B), see Tab. 4.1, was used in the simulation, which gave an initial transmission efficiency of 50%. After using the optimization program with a step size of $\pm 10\,\mathrm{V}$, an efficiency of 67% (set B') was obtained. Again, the ions are lost at the collimator. Since the radius of the ion bunch is larger with set B' than with set A', more ions get lost at the collimator.
Under the condition that all ion-optical elements are well aligned, the transmission from the precision trap to the decay-station setup can be optimized to at least 92% in the simulations. If the diameter of the collimator is increased by 1 mm, which still produces a small enough sample on the tape, this can be increased to 100%. Still, the applicability to real measurements has to be verified. This can be done by taking the ratio of the results from set A and B in real measurements in comparison to the ratio from the simulations. If discrepancies occur this might be due to the difference between the measured and simulated magnetic field, to the chosen starting conditions or misalignment of beam-line elements. Here a more intense study would be valuable.

4.2. Bending studies

To improve the vacuum in the precision trap while sending ions to the decay station, it was suggested to improve the decoupling between both setups. In addition, the current decay-station setup is restricted in height by the ISOLDE overhead crane. A new beam line that bends the ion path by 90° would solve both problems at once. In this way a differential pumping section can be realized, a longer pulsed cavity can be used and more detectors can be arranged around the detection chamber.

electrode	voltage / V	electrode	voltage / V
drift 1	-580	deflector 2	1583.821
drift 2	-580	deflector 3	-2647.408
drift 3	-580	deflector 4	-471.476
drift 4	-105.519	focus 1	-1214.063
drift 5	-1407.759	focus 2	921.484
deflector 1	-703.906	focus 3	-2601.563

Table 4.2: One set of voltages for the electrodes shown in Fig. 4.3 that give a transmission of 100%.

For bending of the ions either an electrostatic or a magnetic configuration was discussed. The latter was excluded since an additional magnetic field would influence the magnetic field required for the mass measurements. As the simplest approach, a quadrupole deflector consisting of 4 round electrodes, as shown in Fig. 4.3, was implemented in a SIMION potential array [Fou11].

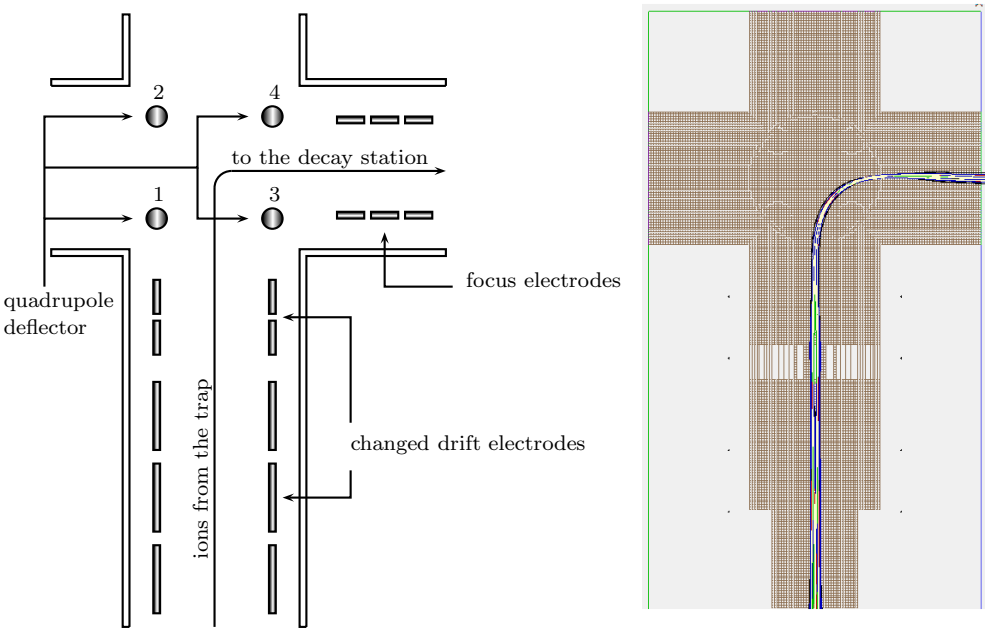

Figure 4.3: Left: Geometry used for bending studies in SIMION. Only the modifications to the cross that currently houses the MCP for mass measurements are shown. Some drift tubes were changed to allow a proper injection into the quadrupole deflector. After the bender, several electrodes are implemented to focus the ions. Right: Ion trajectories after the optimization. The voltages applied to the electrodes are shown in Tab. 4.2.

It replaces the mass-measurement detector which can be either attached to the top or to the side. This geometry was superimposed with the magnetic field as shown in Fig. 4.2. The electrode potentials were optimized using a

simplex algorithm. The optimization was done by minimizing the transversal components of the ion velocity and the distance to the center of the beam line several cm behind the focusing electrodes. By storing also the number of bent ions, located on a disk with 5 mm radius at the center of the beam line, it was shown that a transmission efficiency of 100% can be reached. Besides the realization of the quadrupole bender, the switching from the mass-measurement mode to the decay-spectroscopy mode should be fast and reproducible. For the mass measurements an ion detector is needed. It can be placed either on a feedthrough from the side or fixed on top of the bending cross. In the latter case a system similar to the HITRAP/FAIR could be used. It consists of a MCP, a drift tube and a quadrupole bender, which are mounted on a feed-through system, as shown in Fig. 4.4.

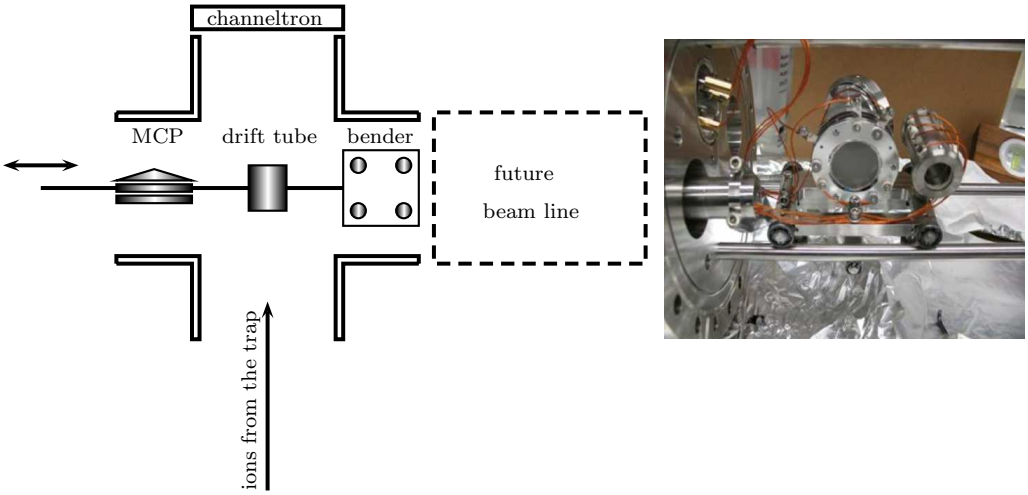

Figure 4.4: Left: Scheme of the feed-through system allowing (i) access to ion detectors, located at the side or on the top of the bending cross, for mass measurements, as well as (ii) access to the future beam line to the decay station via a quadrupole bender. Right: Realization of a similar system at HITRAP/FAIR.

4.3. Detection efficiency

As it is shown in chapter 5, the ISOLTRAP decay station is well suited to study gamma-rays that accompany β-decays. However, due to the chosen configuration and the geometry of each detector, clearly not all emitted particles can be detected. Especially, when analyzing gamma-ray spectra recorded in a germanium detector, the ratio of the detected full-energy events to the emitted ones becomes important. The absolute full-energy-peak efficiency of a detector is thus defined as

$$\varepsilon = \frac{\text{number of counts in full energy peak}}{\text{number of gamma-rays emitted by the source}}. \tag{4.3}$$

Usually, ε is determined with standard calibration sources, placed at the measurement position. In this case, it is however difficult to determine the position. In addition, the distance between the implanted source and the HPGe detector is quite small. Therefore, summing coincidence can occur, i.e. the detection of more than one gamma-ray at the same time, leading in the gamma-ray spectrum on the one hand to fewer counts at the single gamma-ray energies and on the other hand to more counts at the energy equal to the sum of the single gamma-ray energies. To support this study and to improve the understanding of the implemented decay-spectroscopy system, Monte-Carlo-simulation studies with the geometry and tracking toolkit Geant4 [gea12] were performed.

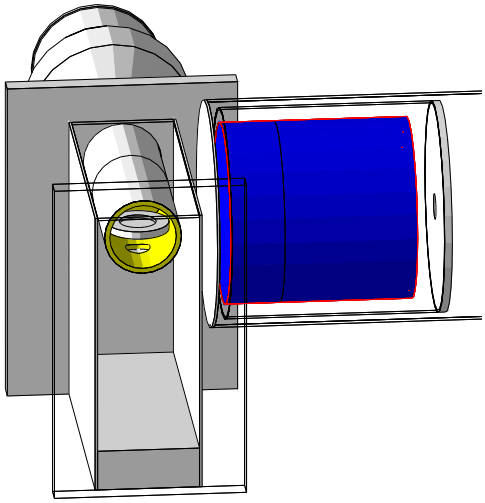

Figure 4.5: Decay chamber geometry used for Geant4 simulations. The scintillator (yellow) and the germanium crystal (blue) are declared as sensitive volumes. A standard calibration source is placed inside the scintillator and just above the injection hole. For some studies it was replaced by 2 layers of aluminized Mylar® tape.

Geant4 is based on the object-oriented programming language C++. Thus, several classes must be provided by the user. The three mandatory ones are the DetectorConstruction, the PhysicsList and the PrimaryGeneratorAction class. The DetectorConstruction class allows to define even complex geometries and materials. In addition, parts of the geometry, namely the detectors, can be registered as sensitive volumes. Those allow to store information about interactions of particles with the volume. For the decay station, the geometry as shown in Fig. 4.5 was implemented with the materials as provided by the manufacturer or as implemented in the Geant4 material list. It was decided to leave the parameters of the HPGe detector adjustable, since it is not a fixed part of the system. In the PhysicsList class all particles and the corresponding processes taken into account during the simulation, are contained. The most important particles for the interaction with the detector material and thus the energy deposition are gamma-rays, electrons and positrons. The processes are

divided into (i) transportation that is used for all particles, (ii) electromagnetic interactions that are defined particle-wise by

```
if (particleName == "gamma")
{
        // gamma
        pmanager->AddDiscreteProcess(new G4PhotoElectricEffect);
        pmanager->AddDiscreteProcess(new G4ComptonScattering);
        pmanager->AddDiscreteProcess(new G4GammaConversion);
}
else if (particleName == "e-")
{
        //electron
        pmanager->AddProcess(new G4eMultipleScattering,-1, 1, 1);
        pmanager->AddProcess(new G4eIonisation,         -1, 2, 2);
        pmanager->AddProcess(new G4eBremsstrahlung,     -1, 3, 3);
}
else if (particleName == "e+")
{
        //positron
        pmanager->AddProcess(new G4eMultipleScattering,-1, 1, 1);
        pmanager->AddProcess(new G4eIonisation,         -1, 2, 2);
        pmanager->AddProcess(new G4eBremsstrahlung,     -1, 3, 3);
        pmanager->AddProcess(new G4eplusAnnihilation,    0,-1, 4);
}
```

and in addition (iii) radioactive decay as the initial process. By default, the electromagnetic processes make use of standard electromagnetic physics. Alternatively, low energy physics based on the Livermore or Penelope library can be considered by choosing them at runtime. In the PrimaryGeneratorAction class the initial event must be provided with the particle type, its energy and position before the compilation. For the decay-station simulations it was decided to use instead the Geant4 GeneralParticleSource [gps12]. This allows to choose all properties of the initial event at runtime. Beside the mandatory classes several user classes can be defined. They are either messenger or action classes. The first handle the input for the simulation, like geometrical parameters. The latter take care of the data processing and the output of the simulation. In this case the energy deposition in the scintillator and in the germanium crystal are stored, both in text-files and ROOT-histograms [roo12]. When the program is executed an interactive session is started, allowing to put information into the simulation without changing the source code. First, the program is in a pre-initialization state. This is the only state where geometrical parameters such as

```
/Own/det/setCapLength 0.5 mm   #half thickness of end cap
/Own/det/setDistance 5 mm      #distance end cap to crystal
/Own/det/setCRadius 35.5 mm    #crystal radius
/Own/det/setCLength 26.5 mm    #half length of crystal
/Own/det/setHRadius 5 mm       #hole radius
/Own/det/setHLength 25.5 mm    #half length of hole
/Own/det/setODead 0.0005 mm    #outer deadlayer
/Own/det/setIDead 0.7 mm       #inner deadlayer
/Own/det/update
```

for the germanium detector are accepted. Also the choice for low energy physics

```
/Own/phys/SelectPhysics livermore
```

must be made in this state. Afterwards, the program is ready for initialization by

```
/run/initialize
```

and enters the idle state. Here, if needed, the visualization modules and the direction for the output can be chosen. Also the properties of the initial event are fixed by calling at least the following commands, for further properties see [gps12].

```
/gps/particle ion                #particle type
/gps/ion 27 60                   #nuclide that should decay (60Co)
/gps/position 0 0 0              #x y z in cm
```

The simulation is finally started by calling

```
/run/beamOn 10000                #number of events to process,
```

where 10000 initial events are created and processed.
The program was first used to study the response of the scintillator to mono-energetic and multi-energetic electrons. Under investigation were especially the energy information that one could gain from the scintillator as well as its efficiency. For this purpose, electrons with energies of either 200 or 2000 keV, in the following referred to as low- and high-energy electrons, were considered. They were launched from inside a standard calibration source which was placed just above the injection hole of the scintillator. The result is shown in Fig. 4.6. When starting from the source all electrons initially loose part of their energy due to interactions with the source container. The low-energy electrons deposit their remaining energy completely in the scintillator. The high-energy electrons leave only part of their energy in the scintillator due to its thickness. The result is an energy distribution which can be described by a Landau distribution with a maximum around 400 keV. Roughly 20% or 90% of electrons were counted, for

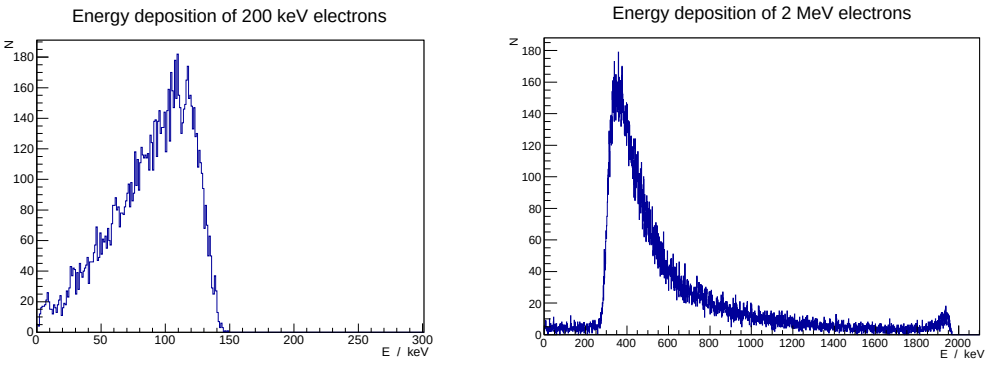

Figure 4.6: Energy deposition in the scintillator for 200 and 2000 keV electrons starting from a standard calibration source. The electrons interact with the coating and loose part of their energy before entering the scintillator.

low and high energy respectively. This counting efficiency is mainly determined

by the interaction of the electrons with the source encapsulation. In addition, the scintillator itself doesn't cover the full solid angle and thus electrons can escape, for example through the injection hole. Although this simple example doesn't reflect the measurement conditions, it is well suited to learn some properties of the system. First, low-energy electrons emitted in every β-decay will to some extent interact with the closest material, which is the tape, such that some of them cannot be detected. Second, since the source will always be just above the injection hole, some of the electrons will escape without interacting with the scintillator. This limits the overall electron-detection efficiency of the scintillator which is important for β-γ-coincidence studies. Third, the scintillator can not provide energy information because the electrons will loose part of their energy already in the tape material and deposit only another fraction of their energy in the scintillator, where the latter is determined by the thickness of the scintillator. Thus, the scintillator will only be used as a trigger of the decay.

To reproduce better the measurement conditions, the source volume was replaced by two layers of aluminized Mylar® tape 12 mm broad and 10 μm thick. A ^{60}Co source with a radius of 2.5 mm was placed on the lower layer, just above the injection hole of the scintillator. Depending on the exact material composition of the tape, 47-58% of the initial electrons were detected. Fig. 4.7 shows an energy deposition in the scintillator up to an energy of roughly 300 keV representing the β-decay of ^{60}Co to the excited state in ^{60}Ni. In the energy spectrum

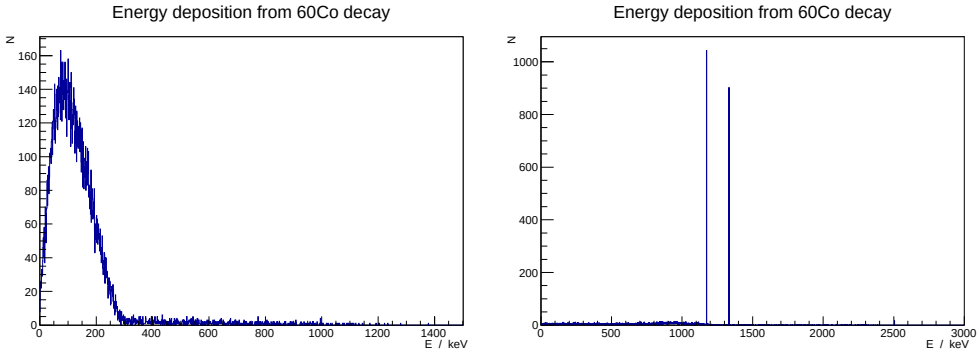

Figure 4.7: Energy deposition in the scintillator (left) and the germanium detector (right) for a plane source of ^{60}Co starting from a thin aluminized Mylar foil.

recorded by the germanium detector the two main transitions with energies of 1173 and 1333 keV are clearly visible, where the energy resolution was assumed to be perfect.

Besides the single spectra, a coincidence spectrum was recorded, containing only events in the germanium detector triggered by an event in the scintillator, see Fig. 4.8. A two-fold reduction, because of the scintillator efficiency is clearly visible, especially in the full energy peaks.

Finally, the simulations were used to determine the efficiency of the germanium detector as a function of gamma-ray energy. Here, the approach will be

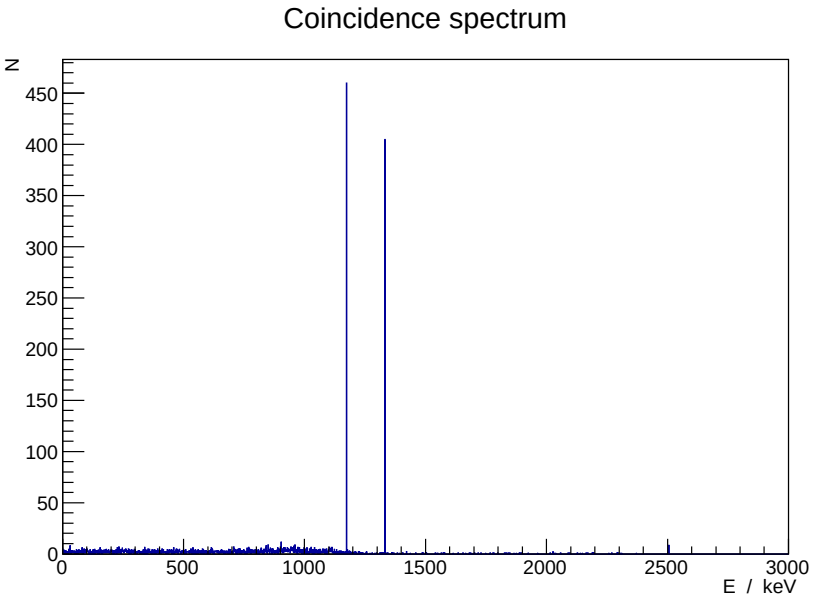

Figure 4.8: β-γ-coincidence spectrum for ^{60}Co. The total number of counts is reduced by a factor of $\sim$2 compared to the ungated γ-spectrum due to the detection efficiency of the scintillator. This is easily seen in the full energy peaks.

demonstrated for one n-type detector as it was used in 2010 with the geometry parameters given by the manufacturer, see Tab. 4.3. The length of the hole in the crystal and the inner dead layer were not given. The first was calculated from the given active volume. The latter was chosen appropriate compared to other HPGe detectors. First, the efficiency curve, as shown in Fig. 4.9, was

crystal radius	35.5 mm
crystal length	73 mm
hole radius	5 mm
hole length	51 mm
outer dead layer	0.5 μm
distance to endcap	5 mm
thickness of endcap	1 mm
inner dead layer	0.7 mm

Table 4.3: Geometry parameters as given by the manufacturer (black) for a 73% n-type HPGe detector. The hole length was calculated from the active volume given and the inner dead layer was chosen reasonably.

constructed from the calibration measurements with ^{137}Cs, ^{60}Co and ^{152}Eu by

calculating

$$\varepsilon = \frac{N_P}{I_\gamma \cdot A \cdot t} \tag{4.4}$$

for each full-energy peak. Here N_P is the number of counts in the full energy peak, I_γ is the absolute intensity of the gamma-ray, as given for example in [Fir96], A is the activity of the calibration source and t the measurement time.

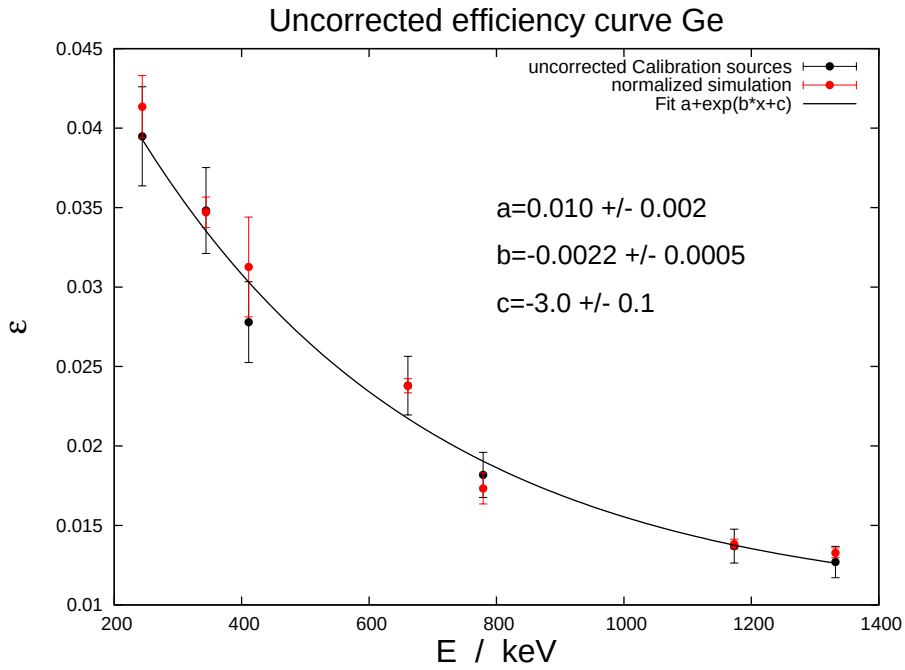

Figure 4.9: Efficiency curve from calibration measurements with ^{152}Eu,^{137}Cs and ^{60}Co for the HPGe detector used at the implantation point in 2010. The large uncertainties of the measurement values are mainly due to the uncertainties on the activity of the calibration sources that was taken to be 7%. Corrections due to summing coincidences are not yet considered.

Only peaks with an energy above 200 keV were considered since they allow an exponential fit in the form

$$\varepsilon(E) = a + e^{b \cdot E + c}. \tag{4.5}$$

As the next step each of the three sources was simulated and their efficiency was determined for several energies. It turned out that the simulation overestimates the efficiency of the HPGe detector but follows the same trend. Following an approach suggested by M. Venhart [Ven11], the simulated efficiency curve was normalized to the measured value of the mono-energetic ^{137}Cs source. The normalized simulations and the measurement agree within uncertainties. Thus, no reshaping of the crystal in the Geant4 simulation was needed, which becomes necessary if discrepancies appear.

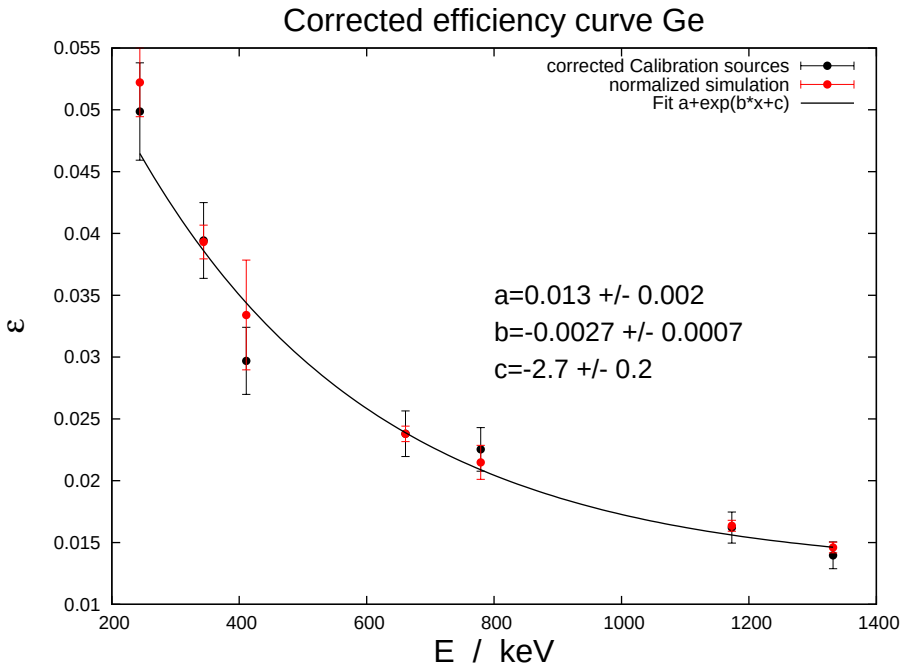

Figure 4.10: Efficiency curve as constructed from the calibration measurements including corrections due to summing coincidences for the same detector as in Fig. 4.9.

In addition, corrections due to the already mentioned summing coincidences have been considered. The correction factors were determined by comparing the efficiency from the simulation with mono-energetic gamma-ray sources with the efficiency from simulations with decaying ions. The final efficiency curve in comparison with the simulated one is shown in figure 4.10. The resulting fit parameters (Eq. 4.5) were finally taken to determine the efficiencies for the analysis of the thallium data as described in the following chapter.

5. Measurements on neutron-deficient Tl isotopes

The decay station as described in section 3.3 was used during two experiments connected to the ISOLTRAP proposal IS463 [Kea07]. In this proposal it was intended to investigate the β-decay of poorly known neutron-rich Tl and Hg isotopes in the vicinity of the N=126 shell closure. Nuclear-spectroscopy measurements in this region are usually hampered by the large activity resulting from isobaric surface-ionized francium. Thus, the ISOLTRAP experiment is intended to remove the contaminants and together with the decay station allow nuclear spectroscopy on pure samples. Both beam times suffered from the ionization procedure available and the limited production rates. As an alternative, the isomerism that is prominent in the neutron-deficient Tl isotopes was studied, starting from ^{195}Tl to the more neutron-deficient isotopes. The odd-A isotopes were mainly used as test cases to uncover new features of the measurement unit. For even-mass isotopes with $A \leq 194$ it was striking that the spin-state ordering of the ground and first isomeric states or its excitation energy are only predicted from systematics but not determined experimentally [ens12]. This is either due to the missing internal transition from the isomer to the ground state or to the insufficient precision when measuring the β-endpoint energies to the Hg daughters. Thanks to the combination of the ISOLTRAP setup with the decay station it is possible to measure the masses of the ground and isomeric state and to assign a decay pattern to them. In the following chapter, details on each beam time, the data analysis and the obtained results are presented.

5.1. Beam time November 2010

Since this beam time was intended for heavy mass nuclei, a target ion-source unit (#441), comprised of a uranium-carbide target and a tungsten surface ionizer, was used for the beam production. The spallation products were ionized by surface ionization, accelerated to an energy of 40 keV and subsequently mass separated by the High Resolution Separator (HRS). For mass measurements, the cycle as shown in Fig. 3.13 was applied skipping the last step. For decay measurements, the full cycle was applied. The cleaning sequence in the precision trap was omitted throughout the measurements due to its influence on the ion count, as discussed below. The three Tl isotopes $^{193-195}$Tl with known isomerism were under investigation on the one hand to test the cooperation of the mass-measurement setup with the decay station and on the other hand to obtain a deeper understanding of the isomerism in this region. For the nuclides the present knowledge of the ground-state mass excess and the excitation energy

of the first isomer is shown in Tab. 5.1.

isotope	mass excess (gs) / keV	excitation energy (m) / keV
^{193}Tl	-27320 (110)	365.2+x
^{194}Tl	-26830 (140)	300# (200#)
^{195}Tl	-28155 (14)	482.63 (17)

Table 5.1: Mass excess of the ground states and excitation energy of the first isomeric state from [AWT03, ens12]. For ^{193}Tl there exist two excited states, where the higher one is the metastable and the lower one de-excites by emitting a gamma-ray with 362.5 keV. The difference between both states is $x < 13$ keV.

5.1.1. Mass measurements of ^{193,194,195}Tl

The data obtained during the mass measurements were analyzed, using the method of [Kea03], and presented in more detail in [Bor12]. Here only a summary is given for completeness.
One important part of the mass measurements is the cross-check measurement with a well known mass to track systematic drifts. This was done with the mass of ^{85}Rb, produced by the ISOLTRAP off-line ion source, see Fig. 3.1. An agreement within 1σ with the value listed in [AWT03] was determined.

^{193}Tl: In this case there was only one state observed and no other contamination seen in the precision trap. The time for the quadrupole excitation in the precision trap was chosen to be 100, 2000 and 2500 ms. The resulting mass excess is $-27105.5(5.4)$ keV, where the uncertainty is decreased by a factor of 20 with respect to the previous value [AWT03]. Thanks to the decay measurements, presented below, this value can be assigned to the isomeric state.

^{194}Tl: The ground-state spin 2^- was assigned from hyperfine structure measurements by [EWS75]. However, the excitation energy of the (7^+) isomeric state was never determined experimentally before. Initially, only one state was present in the mass measurements that turned out to be an excited state. To produce the ground state as well, benefit was taken from an indirect population reaction. It was expected that in the target ^{198g}Po, with spin and parity 0^+, was also produced. It populates the 0^+ ground state of ^{194}Pb via α-decay. The subsequent electron capture/β^+-decay of this state only populates low-spin states in ^{194}Tl and according to

$$^{198g}\mathrm{Po} \xrightarrow[t_{1/2}=1.76\,m]{\alpha} {}^{194g}\mathrm{Pb} \xrightarrow[t_{1/2}=12\,m]{EC+\beta^+} {}^{194g}\mathrm{Tl} \tag{5.1}$$

this also yields the ground state. Then a ToF-resonance can be measured if the excited state can be suppressed. The latter is done by stopping the proton irradiation on the target. Finally, two ToF-resonances were obtained that clearly show a difference in their center frequencies, see Fig. 5.1. The state

that was present during proton irradiation on the target has a lower center frequency and is thus, according to Eq. 3.4, higher in mass and can be referred to as the isomeric state. The other state, which is lower in mass, is then the ground state. The mass excess of the ground and isomeric states were determined to −26938(14) keV and −26677.2(3.8) keV, respectively. They agree with the values from [AWT03] within 1σ. They yield an energy difference of 260(15) keV which would be in agreement with the value of the excitation energy predicted from systematics, see Tab. 5.1. To interpret the energy difference as the (7^+) isomer excitation energy, a decay pattern has to be assigned to the isomer which is done by decay measurements with the tape station.

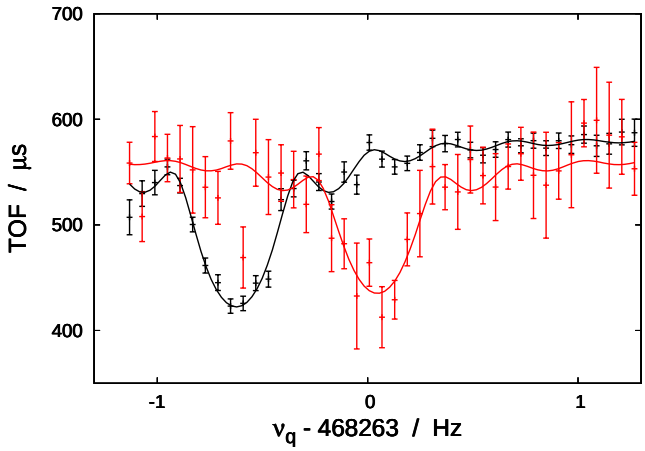

Figure 5.1: Time-of-flight resonances obtained for ^{194}Tl. The black resonance, which was dominant during proton bombardement, corresponds due to Eq. 3.4 to a higher mass and thus to the isomer. The red resonance was obtained while stopping the proton current. It corresponds to the ground state.

^{195}Tl: Here mainly the ground state was observed in the mass measurement. Resonances were recorded with 100 and 1200 ms quadrupole excitation time. Especially for the longer excitation time, the number of decay products was increased. This was interpreted as originating from an isomeric admixture and thus the analysis was performed for a mixed sample. The obtained ground-state mass excess is −28162(25) keV which agrees with the ground state value from [AWT03]. The mass excess of the isomer was determined to −27589(73) keV leading to an excitation energy of 573(75) keV.

5.1.2. Decay measurements of ^{193,194,195}Tl

As described in section 3.3.1 one HPGe detector and two PMTs coupled to the scintillator were operated at the implantation point. The signal of each detector was fed into a channel of a XiA DGF-4C(E) module, for more details see [xia12]. In total, two modules were used and the channel assignment is shown in Tab. 5.2. Each channel has its own configuration file with a set of parameters to optimize

its performance. Nevertheless, the best energy resolution that was obtained for the HPGe detector, was only 3.5 keV at an energy of 1.33 MeV. The reason was found in the vibrations of the experimental platform as well as the electrical shielding of the signal cables which was improved in subsequent measurements. For every detected event the module number, channel number, signal height in channels and the timestamp were written into a binary data file. The precision of the modules is 16 bit. To cover a time window of several hours, the time is separated into t_{high}, t_{middle} and t_{low}. The total timestamp in μs is

$$t = \frac{2^{16} \cdot 2^{16} \cdot t_{\mathrm{high}} + 2^{16} \cdot t_{\mathrm{middle}} + t_{\mathrm{low}}}{40} \tag{5.2}$$

since the modules have a processing rate of 40 MHz. The conversion of the data files to ROOT trees [roo12] was done by a home-made conversion program. Finally, the information allowed to study β-γ-coincidences or conversion electron-γ-coincidences besides single spectra by off-line analysis.

Channel	Module 1	Module 2
0	Ge1 (impl)	PMT $\parallel$
1	Ge2 (decay)	PMT $\perp$
2	Trap ej.	-
3	-	-

Table 5.2: Channel usage of the XiA modules in 2010.

Energy calibration: Depending on the height of the recorded signal, a channel is assigned to each event. The energy corresponding to this channel is obtained from an energy calibration with standard calibration sources. In this beam time ^{137}Cs, ^{60}Co and ^{152}Eu were used for the calibration. The calibration curve is shown in Fig. 5.2 and was used for the analysis.

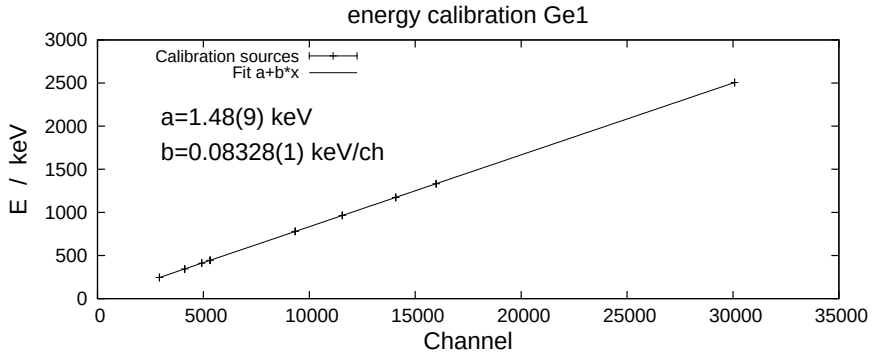

Figure 5.2: Energy calibration curve for the detector at the implantation point.

Background: In gamma-ray spectroscopy, the spectrum always contains sig-

nals from background activity. Natural radiation background, as well as special radiation background from the experimental area, contribute. In preparation for the decay measurements at the ISOLTRAP experiment, several background measurements were taken. The main contributions come from the natural radiation background, as listed in Tab. 5.3 and shown in Fig. 5.3.

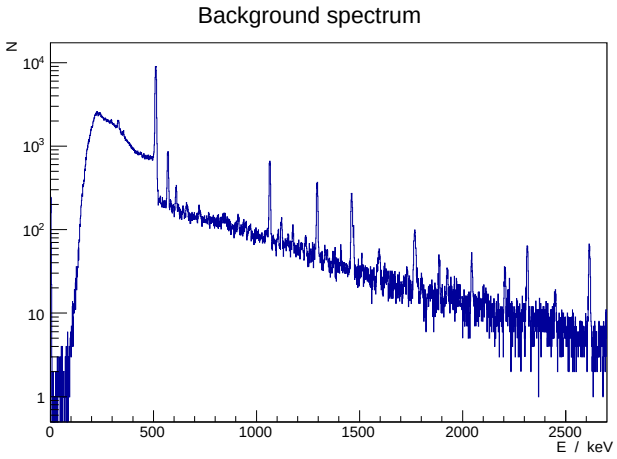

Figure 5.3: Example for the observed background. The spectrum was taken during 1 h 16 m. Main contributions come from natural background.

Energy / keV	Origin	Energy / keV	Origin
295.2	^{214}Pb	1155.2	^{214}Bi
327.9	^{228}Ac	1173.2	^{60}Co
328.0	^{212}Bi	1238.1	^{214}Bi
351.9	^{214}Pb	1294.1	
511.0	e^+e^- annihilation	1460.8	^{40}K
569.3	^{134}Cs	1592.9	DE ^{208}Tl
569.7	^{207}Bi	1729.6	^{214}Bi
583.2	^{208}Tl	1764.5	^{214}Bi
609.3	^{214}Bi	1770.2	^{207}Bi
661.7	^{137}Cs	1888.7	^{214}Bi+511
719.9	^{214}Bi	1925.4	
768.4	^{214}Bi	2044.5	
911.2	^{228}Ac	2204.2	^{214}Bi
949.8	SE ^{40}K	2222.9	
968.9	^{228}Ac	2313.2	
1063.7	^{207}Bi	2447.8	^{214}Bi
1120.3	^{214}Bi	2614.5	^{208}Tl

Table 5.3: List of main background contributions as observed in 2010. The origin is indicated if known.

Not all peaks could be identified but were excluded from the data analysis due to their presence in the background spectrum. A striking feature of all recorded spectra is the strong peak at 511 keV although β^+-decay not necessarily happened. This is related to the proton impact on the target that is followed by a strong 511 keV gamma-ray emission across the ISOLDE facility.

Efficiency curve: The efficiency curve gives the probability to detect a gamma-ray with a certain energy in a defined geometry. The same nuclides as mentioned above were used to determine the efficiency curve for the HPGe detector at the implantation point. For ^{60}Co and ^{152}Eu, true summing-coincidence correction factors were determined using Geant4 simulations, as described in the previous chapter. The resulting efficiency curve is shown in Fig. 4.10.

^{193}Tl: This nucleus has a $(9/2^-)$-isomeric state at (365.2+x) keV which decays to the $1/2^{(+)}$-ground state via an intermediate state, by either emitting a gamma-ray of 365.2 keV or by internal conversion. Alternatively, it undergoes EC/β^+ to ^{193}Hg [Gea76]. The ground state itself decays via EC/β^+ to ^{193}Hg where the β^+-contribution is about 4% [Vea74].

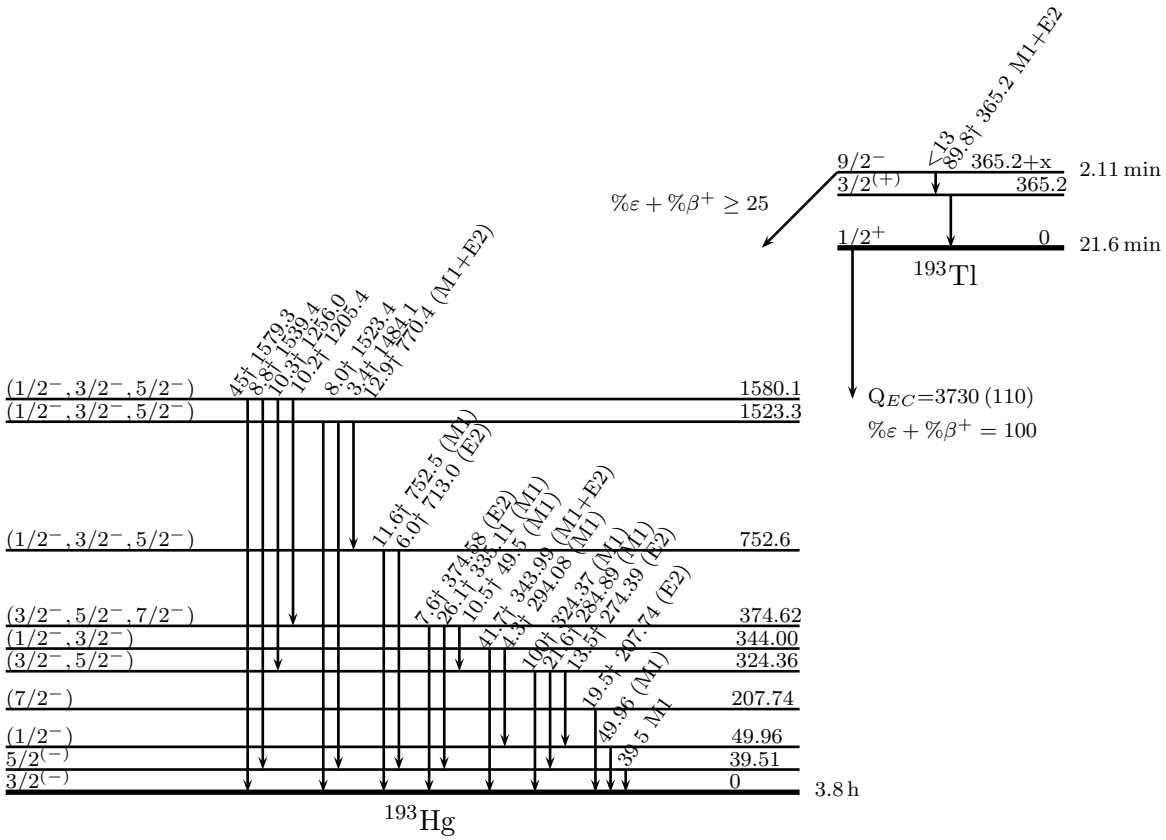

Figure 5.4: Decay scheme of ^{193}Tl. Numbers were taken from [ens12, Aea06]. Energies are given in keV.

As it is shown in figure 5.4, the branching ratios to the different excited levels in ^{193}Hg are not determined so far, but the feeding to the levels below 50 keV was estimated to be less than 20% [ens12].
This isotope gave first hints for the dependence of the detected ion count rate on the waiting time in the precision trap. It was shown that while choosing a waiting time of 1 s, either with or without applied dipole excitation, the ions could not be detected any longer in the detection chamber. Thus, it was decided to omit dipole cleaning and waiting times in the precision trap while performing decay spectroscopy. Later it was found that the detected ion count drops to zero for waiting times separated by roughly 0.6 ms, corresponding to a frequency of the order of the magnetron frequency. Thus, it appears as if the magnetron motion in the precision trap is not entirely converted into the cyclotron motion. This residual motion might interact with the magnetic field such that the ions are driven out of the flight path. This behavior has to be investigated more carefully.
During one measurement without dipole cleaning and a waiting time of 10 μs the gamma-ray that is emitted while the isomeric state de-excites was observed in the single spectrum of the germanium detector at the implantation point. Thus, the ground state was created in the decay chamber where it should subsequently decay to ^{193}Hg. However, a clear evidence for this decay was not observed in the γ-spectrum. To understand this puzzling fact, the number of ^{193m}Tl, ^{193g}Tl and ^{193}Hg at the end of the measurement was calculated

$$N_{193m}(t) = \frac{N_0}{\lambda_{193m} \cdot t_c} \left(1 - e^{-\lambda_{193m} \cdot t}\right) \tag{5.3}$$

$$N_{193g}(t) = \frac{N_0}{\lambda_{193g} \cdot t_c} + \frac{N_0}{tc \cdot (\lambda_{193g} - \lambda_{193m})} \left[\frac{\lambda_{193m}}{\lambda_{193g}} e^{-\lambda_{193g} \cdot t} - e^{-\lambda_{193m} \cdot t}\right] \tag{5.4}$$

$$N_{Hg}(t) = \frac{N_0 \cdot t}{t_c} - N_{193m}(t) - N_{193g}(t) \tag{5.5}$$

with N_0 the MCP-efficiency corrected ions per implantation, t_c the cycle length and $\lambda = \ln 2/t_{1/2}$ the decay constant of the corresponding nuclide. The results for $N_0 = 26$, $t_c = 1.58$ s and $t = 5400$ s are given in Tab. 5.4. According to

nuclide	number
^{193m}Tl	3005
^{193g}Tl	28869
^{193}Hg	56986

Table 5.4: Calculated number of nuclides after the measuring time based on the detected count rate, the cycle length and the measuring time.

this calculation roughly 57000 ground-state decays happened during the measurement time. From the ground-state decay a transition at 324.4 keV with a relative intensity of 100% is expected, according to [Vea74]. Due to the bad energy resolution, the corresponding peak was expected to overlap partly with

the 328 keV background peak. Following [Gil08], the background peak area was subtracted from the sample peak. This leaves a net peak area of 420(293) counts. Taking the numbers from Tab. 5.4, Eq. 4.4 and assuming that 80% decay via the 324.4 keV level, this corresponds to an absolute intensity of 23%. The expected number of counts from the next strongest transition at 284.9 keV from the same level was also calculated, see Tab. 5.5, with an intensity weighted by 23%. For the following analysis, the method described in appendix D was used. From the gamma-ray spectrum the net count and the critical limit were determined in this energy region. In addition, the upper limit was determined since the net count is smaller than the critical limit. It is 95% certain that the real number of counts with 284.9 keV is less than this upper limit. The expected number of counts is less than the upper limit and thus it is conclusive to not observe a peak at 284.9 keV if the absolute intensities of the ground-state transitions are small. However, the question, what are the branching ratios to the levels in ^{193}Hg cannot be solved.

expected counts	97
net peak area	74
critical limit	260
upper limit	334

Table 5.5: Analysis in the region of 284 keV following [Gil08]

Furthermore, coincident signals within a time window of 1.5 μs between the scintillator and the germanium detector were investigated. Since mainly EC is expected this should yield coincidences between conversion electrons and gamma-rays. However, there was no clear evidence for gamma-rays that could be assigned to the decay scheme of ^{193g}Tl. The internal transition that was present in the single spectrum vanished in the coincidence spectrum, confirming that it originates from the isomer.
The observed transition at 365.2 keV is assigned to the decay of the isomeric state in the decay chamber and thus the creation of the ground state and its subsequent decay is expected. Unfortunately, the signature of the ground state EC in the single spectrum is pretty weak and in addition, due to the bad energy resolution, overlapped by background lines. The measurements on this nucleus showed some features of the measurement setup that are not relevant for mass measurements and thus have not been known before. First, a count-rate dependence on the dipole excitation or waiting time in the precision trap was uncovered, as described before. Second, there are combinations of half-lives and absolute intensities which complicate the decay measurements. This situation could be improved by background reduction in combination with longer measurement times. To facilitate the interpretation, additional detectors could be placed to access more decay information, for example about conversion electrons.

^{194}Tl: In this nucleus the existence of the (7^+) state with a half-life of 32.8 min

was known for a few decades [JA60]. This state is believed to arise from the

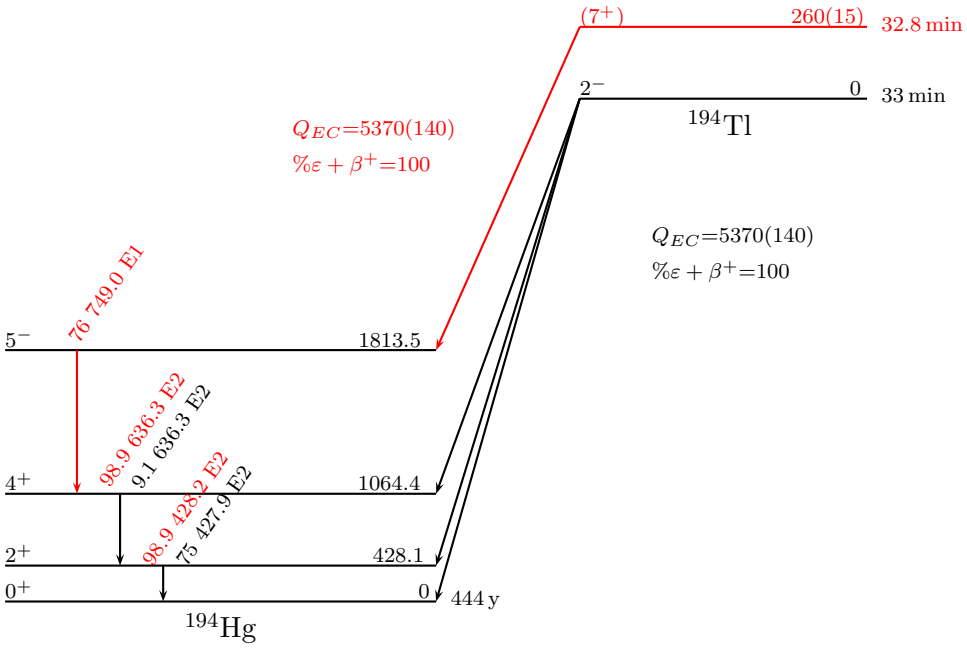

Figure 5.5: Simplified decay scheme for the ground and first isomeric state (red) of ^{194}Tl. Energies are given in keV. Numbers were taken from [ens12, Sin06]. The level energies in ^{194}Hg are mean values.

coupling of the valence proton and neutron in a similar way to that observed in heavier even-A Tl isotopes. Like the 2^- state, it decays via EC/β^+ to ^{194}Hg, see Fig. 5.5. Thanks to the mass measurement on the ion sample with the Penning traps it was known that mostly the isomeric state was present in the ion sample and thus implanted into the tape. The decay measurements were used to assign a state to the time-of-flight-resonances by comparing the measured spectra with the known decay schemes of the 2^- and (7^+) state [Sin06]. If the ions at the cyclotron frequency of the isomer decay as expected from the high-spin state, the determined mass difference of 260(15) keV can be claimed as its excitation energy. The 2 data sets of interest were taken while implanting for 1.5 h and 2.5 h, respectively. As can be seen in Fig. 5.6, 3 peaks at 428 keV, 636 keV and 749 keV were observed in the single spectra. The latter was already strong evidence for the presence of the high-spin state. Since both states have the other two transitions in common the intensity ratios of the lines were calculated and compared to the tabulated values in order to determine the purity of the ion sample. The intensity ratios are given by

$$RI_{ij} = \frac{I_{\gamma_i}}{I_{\gamma_j}} = \frac{N_{\gamma_i} \cdot \varepsilon_{\gamma_j}}{N_{\gamma_j} \cdot \varepsilon_{\gamma_i}}. \tag{5.6}$$

were the efficiency ε to each energy was calculated from Fig. 4.10. In the following $\{\gamma_1, \gamma_2, \gamma_3\}$ corresponds to $\{428, 636, 749\}$ [keV].

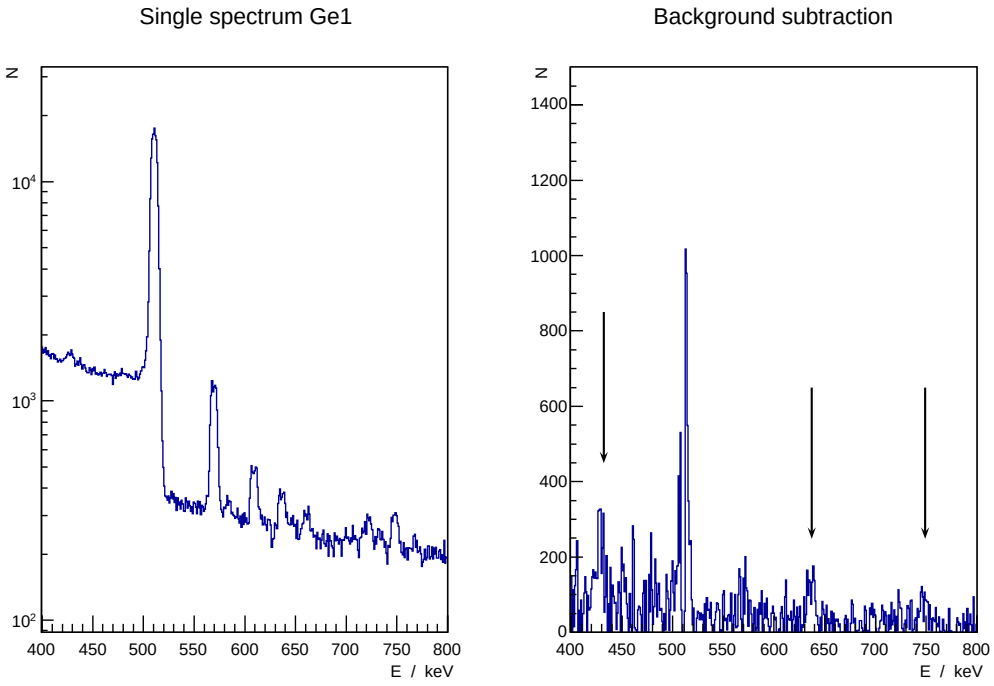

Figure 5.6: Left: single spectrum from the germanium detector at the implantation point, right: same spectrum with subtracted background. The 3 peaks from the decay of ^{194}Tl are visible.

For a pure decay of the 2^- state a ratio $RI_{12}^{\mathrm{t,g}} = 8.24$ is expected from the tabulated values. A pure decay from the (7^+) state would give $RI_{12}^{\mathrm{t,m}} = 1$ and $RI_{13}^{\mathrm{t}} = 1.3$. The ratios which were obtained from the measurement are shown in table 5.6. The weighted average values $RI_{12} = 0.95(12)$ and $RI_{13} = 1.24(16)$

set	RI_{12}	RI_{13}
1	0.97(20)	1.22(27)
2	0.93(15)	1.26(20)

Table 5.6: Intensity ratios obtained for ^{194}Tl.

are in agreement with a pure decay from the (7^+)- state although they allow an admixture of the 2^--state up to 10%. This admixture is the same as the maximal ground state admixture deduced from the mass measurements. Thus, the state, which from mass measurements is determined as the isomeric state, turns out to be the high-spin state in the decay measurements.
Furthermore, coincidences between the scintillator and the germanium detector were studied. All transitions mentioned before were present in those spectra, proving a proper implantation. In one coincidence spectrum an additional transition at 820 keV was observed, see Fig. 5.7. Currently, this gamma-ray is not placed in the decay scheme. Due to the poor statistics and the missing γ-γ-coincidences a conclusion on this transition could not be drawn. In addition,

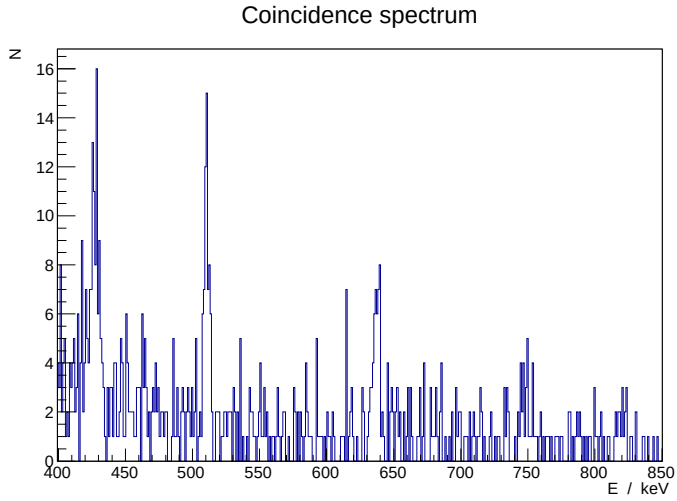

Figure 5.7: Coincidence spectrum between both PMTs and the germanium detector at the implantation point with a coincidence window of 1.5 μs. Beside the transitions already known from the single spectrum a peak at 820 keV is observed.

the data was used to determine the half-life. The number of counts of the 3 strongest peaks was observed every 20 min yielding the growth curve shown in figure 5.8. From this curve a half-life of 37(6) min was determined which is in agreement with the half-lives of the isomer and ground state.

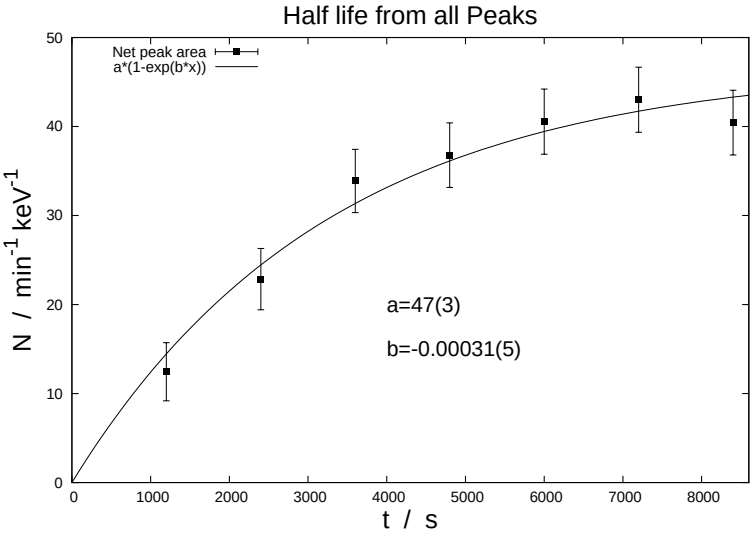

Figure 5.8: Growth curve of ^{194}Tl obtained by measuring the number of counts of the 3 strongest peaks every 20 min.

From the observations presented above together with the result from the mass

measurement it is concluded that an almost pure sample of the isomeric state was implanted into the tape. There it decayed as expected from the high-spin state. Thus, the excitation energy as deduced from systematics can be confirmed.

^{195}Tl: This nucleus has a $9/2^-$-isomeric state with a half-life of 3.6(4) s and a $1/2^+$-ground state with a half-life of 1.16(5) h. The excitation energy is 482.6(7) keV and via a cascade of an E3 transition with 99 keV to an intermediate $3/2^+$-state followed by a 383.6 keV gamma-ray it decays to the ground state. The ground state itself undergoes EC/β^+ to a wide range of excited levels in ^{195}Hg but only with a branching of $\%\varepsilon + \%\beta^+ < 9.1$ to levels below 37 keV including the ground state [Chu99, ens12]. The ion samples were implanted into the tape for 2 h and afterwards decay data was recorded for another 1.25 h. In none of the single spectra clear evidence was found for the decay of ^{195}Tl. Again coincidences between the scintillator and the germanium detector were analyzed but no transitions assigned to the ground state were observed although one would expect them from the mass measurements. In [Bor12] it was stated that the number of decay products increased while increasing the quadrupole excitation time in the precision trap. This was attributed to an isomeric admixture. Thus, if the ions, that were initially in the isomeric state, were decaying on their way to the tape they might get lost due to their recoil energy. Furthermore, the ground-state ions have a pretty long half-life and the intensity of the strongest transition is ~ 7 times smaller then for example the strongest one in ^{194}Tl. Thus, the combination of half-life, intensity and background might have prevented a successful observation.

5.2. Beamtime July 2011

For the second campaign a similar UC-W (#453) target-ion-source unit was used. Besides the surface ionization, the RILIS setup for laser ionization was used [Fea08, Fea12]. This setup allows to apply an element-specific ionization scheme that leads to an enhancement of the desired ions. The ions were accelerated to an energy of 50 keV and the mass separation was carried out by the General Purpose Separator (GPS). For mass measurements, the cycle, as shown in Fig. 3.13, was applied apart from the last step. For decay measurements the full cycle was applied. The cleaning sequence in the precision trap was only applied for the decay measurements in ^{184}Tl.

isotope	mass excess (gs)	exc. energy (m1)	exc.energy (m2)
^{184}Tl	-16890(50)	100#(100#)	500#(140#)
^{190}Tl	-24330(50)	130#(90#)	290#(70#)

Table 5.7: Mass excess of the ground states and excitation energy of the isomeric states in keV from [AWT03].

With the measurements on ^{184,190}Tl, the study on neutron-deficient even mass

Tl isotopes was extended. The previously known ground-state mass excess and excitation energy of the isomers are given in Tab. 5.7

5.2.1. Mass measurements of ^{184,190}Tl

As in the previous section the results from the mass measurements are only given for completeness. A detailed analysis and discussion on them can be found in [Bor12]. The cross-check measurement was again done with ^{85}Rb and yielded an agreement within 1σ with the value from [AWT03].

^{184}Tl: On this mass, only one resonance at the position of the ground and first isomeric states was clearly observed. According to [AWT03], the two states are separated by 50(30) keV, which is difficult to resolve. Another experiment at the ISOLDE facility yielded a 28% (7^+) admixture to the (2^-) state [Rap12]. Assuming also a mixture in the analysis, a mass excess of -16874(22) keV resulted.

^{190}Tl: During the measurements on this nucleus only one state was observed. Time-of-flight resonances were taken with quadrupole excitation times of 200, 900, 1200, 2000, 3500 and 5000 ms. A mass excess of -24292.1(8.8) keV was calculated. To identify this state the decay was investigated at the decay station.

5.2.2. Decay measurements of ^{184,190}Tl

During this beam time, the system described in 3.3.2 was used. Thanks to the second HPGe detector at the implantation point γ-γ-coincidences were studied in addition to single spectra and β-γ-coincidences. As in the previous beam time the signals were recorded by XiA DGF-4C(E) modules and the analysis was done off-line. The energy resolution of the HPGe detectors was optimized to 1.9-2.5 keV at 1.33 MeV, depending on the detector.

Channel	Module 1	Module 2
0	Ge1 (impl)	PMT $\parallel$
1	Ge2 (impl)	PMT $\perp$
2	Ge3 (decay)	Tape move
3	Trap ej.	-

Table 5.8: Channel usage of the XiA modules in 2011.

Energy calibration: In this beam time the detector calibration was done with the calibration sources ^{57}Co, ^{109}Cd, ^{113}Sn, ^{241}Am, ^{133}Ba, ^{137}Cs, ^{60}Co and ^{152}Eu. The resulting energy calibration curves for the two detectors at the implantation point are shown in Fig. 5.9.

Background: As in the previous beam time, several background spectra were taken. They show the same transitions as listed in Tab. 5.3.

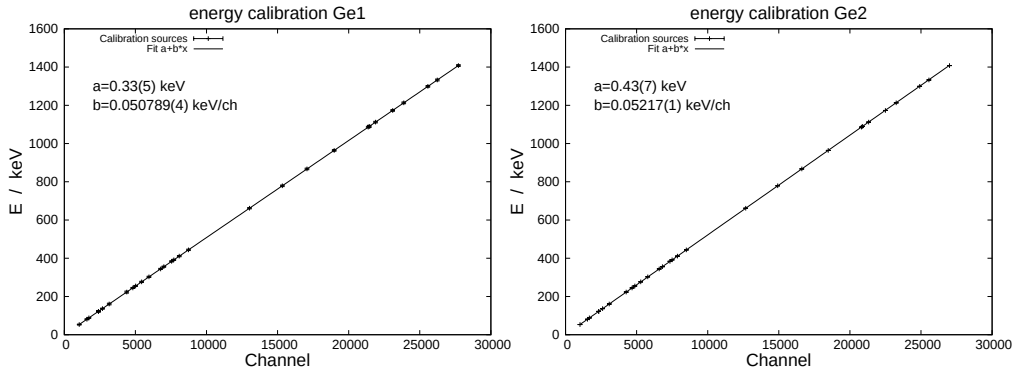

Figure 5.9: Energy calibration curves for the detectors at the implantation point.

Efficiency curve: The efficiency curves for the two HPGe detectors at the implantation point were determined with the calibration sources mentioned above.
Sources such as ^{57}Co, ^{109}Cd and ^{113}Sn do not show true coincidence summing and are thus well suited for efficiency calibrations in close geometries. In addition, ^{241}Am and ^{133}Ba cover the low energy range and thus allow to determine the "knee" of the efficiency curve. The correction factors for true coincidence summing were again determined by Geant4 simulations, as described in chapter 4. The resulting curves are shown in Fig. 5.10.

^{184}Tl: This Tl isotope was the most exotic one under investigation. As in the other even-A Tl isotopes with $A < 194$ a (2^-) and a (7^+) state compete for the ground state [ens12]. In addition, a (10^-) isomeric state has been observed with an estimated excitation energy of 500 keV. For this state, neither a decay scheme nor a half-life was given before the beam time, but a pure internal transition and a half-life of 0.5 s was expected. Since the hyperfine structure of the mixed $(2^-)/(7^+)$ states and the (10^-) state do not (fully) overlap, the lasers were set on the (10^-) state to enhance its admixture. In the precision trap dipole cleaning was applied on the $(2^-)/(7^+)$ state to create a pure (10^-) sample. This was then implanted into the tape. However, neither the single spectra nor the coincidence spectra showed any transition that could be assigned to the decay of ^{184}Tl. A different experiment finally yielded a half-life of 37 ms for the (10^-) state and proposed decay schemes for all states [Rap12]. This half-life lies below the limit of what can be measured with the ISOLTRAP Penning traps and its decay station since the shortest living ion measured at the ISOLTRAP setup had a half-life of 65 ms [Hea02].

^{190}Tl: This nucleus has a $2^{(-)}$ state with a half-life of 2.6(3) min and a $7^{(+)}$ state with a half-life of 3.7(3) min [Bea76]. Both states decay via EC/β^+ to ^{190}Hg, as shown in Fig. 5.11. It is not clear which of the states can be declared as the ground state since their Q-values for the EC/β^+-decay are identical within uncertainties. During the mass measurements there was only one state

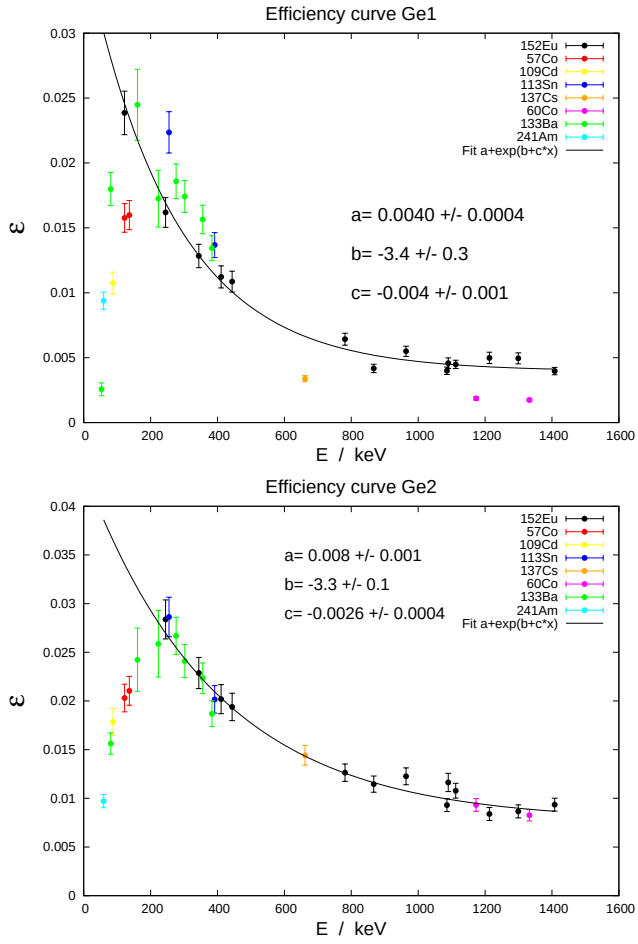

Figure 5.10: Efficiency curves for the HPGe detectors at the implantation point. Only values above 200 keV were considered during fitting. ^{133}Ba, ^{152}Eu and ^{60}Co are corrected for true coincidence summing. As can be seen, ^{152}Eu gives a different profile for the efficiency curve of Ge1 than the other sources. However, simulation studies supported the profile from ^{152}Eu and thus only those values were considered during the fit.

observed and thus this question cannot be answered. Nevertheless, the decay measurements were used to identify this state and to create a fix point. Several data sets were recorded, each during an implantation time of about 15 min. In the single spectra of the two germanium detectors at the implantation point (denoted as Ge1 and Ge2) strong transitions at 416 keV, 625 keV, 731 keV and 839 keV were observed. The latter two transitions can only be observed if the high-spin state decays. To check the purity of the ion sample the intensity ratios for $\{\gamma_1, \gamma_2, \gamma_3\} = \{416.4, 625.6, 731.1\}$ [keV] were calculated, and compared to the tabulated values, using equation 5.6. Table 5.9 shows the expected ratios from the tabulated intensities as well as the calculated ratios from the single spectra. The ratios from the tabulated values do not agree with the calculated

	R_{12}	R_{13}
tab. $(7^{(+)})$	1.1	2.45
tab. $(2^{(-)})$	7.9	-
Ge1	0.64(10)	1.18(18)
Ge2	0.65(5)	1.27(9)

Table 5.9: Calculated intensity ratios for the single spectra in comparison with the ratios obtained from the tabulated values. For both detectors at the implantation point the ratios differ by a factor of 2 from the literature.

ones by a factor of ~ 2. Only the number of counts and the energy-dependent efficiency influence these ratios. Too high counts in the peaks at higher energies might have their origin in summing effects or additional feeding from daughter and grand-daughter decays. Too low counts in lower energies are either due to summing effects or to blocking materials. The summing effects are excluded since there are no low-energy gamma-rays adding up to 625.4 or 731.1 keV and no additional peaks originating from the sum of 416.4 keV and another ^{190}Tl transition.

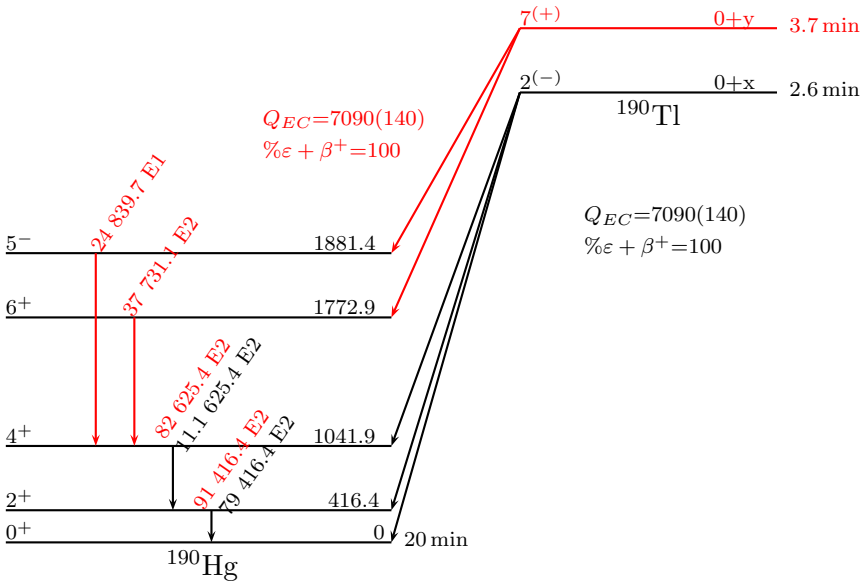

Figure 5.11: Simplified decay scheme of ^{190}Tl. Only transitions and intensities that are relevant for the identification of the spin state are shown. Numbers were taken from [ens12, Sin03]. Energies are given in keV.

Also the daughter and grand-daughter decays cannot account for the obtained ratios since their intensities, at the energies where they might contribute, are too small. The confidence in the efficiency curve is also high since it shows the typical profile [Kno00] and is reproduced by the simulations after normalization.

In addition, both detectors give the same result within uncertainties leading to the conclusion that it is rather a sample feature than an analysis feature.

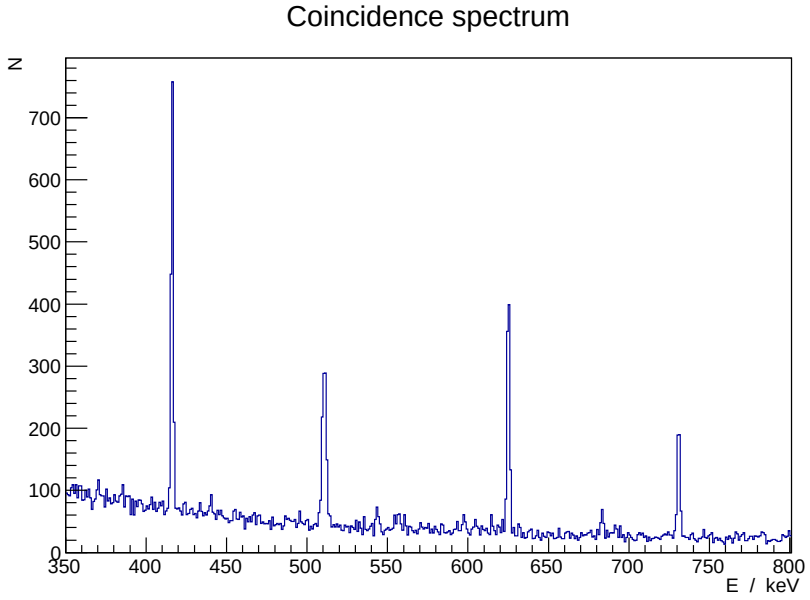

Figure 5.12: γ-Spectrum of detector Ge2 in coincidence with detector Ge1. The three transitions at 416.4, 625.4 and 731.1 keV from the ^{190}Tl decay are clearly visible.

To clarify the situation, only those events from one HPGe detector were analyzed which are in coincidence with the other HPGe detector, yielding a full range γ-γ-coincidence spectrum, as shown in figure 5.12. This spectrum should mainly contain the gamma-rays that are coming from in between the two detectors. The weighted average of the ratios obtained for each detector is shown in table 5.10. Those ratios are in agreement with a pure decay of the high-spin

R_{12}	1.06(19)
R_{13}	1.96(36)

Table 5.10: Weighted average of the intensity ratios obtained from the γ-γ-coincidence spectra between the HPGe detectors at the implantation point.

state. The mismatch of the ratios obtained from the single spectra can be explained by an implantation of the ion samples at a position that is separated from the detectors by enough material to block low-energy gamma-rays. With the ratios from the coincidence spectra it is concluded that the state that was observed during the mass measurement and subsequently implanted in the tape was the $7^{(+)}$ state of ^{190}Tl.
In addition the intensity ratios from β-γ-coincidences were checked. As shown in Tab. 5.11, they also yield intensity ratios that are in agreement with a pure

R_{12}	1.22(15)
R_{13}	3.07(48)

Table 5.11: Weighted average of the intensity ratios obtained from the β-γ-coincidence spectra between the detectors at the implantation point.

$7^{(+)}$ state. The β-γ-coincidences were also used to study β-triggered γ-γ-coincidences. There, an energy gate is set on one transition in one detector and all gamma-rays, that arrive in a certain time window in the second detector, are listed. One example with the gate set on the X-rays is shown in Fig. 5.13.

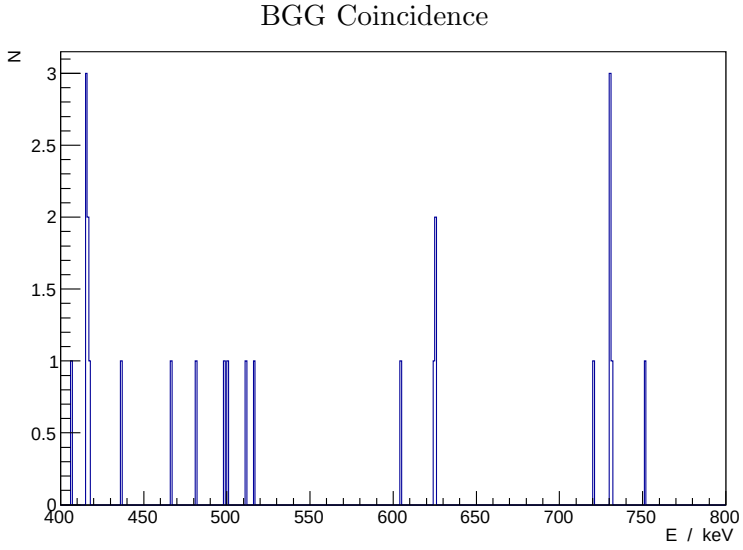

Figure 5.13: β-γ-γ-coincidence spectrum. The gate was set on the X-rays. The coincidence-time window was chosen to be 2 μs.

There the coincidence with the three strongest transitions is seen. Somewhat surprising is the strength of the 731 keV transition. This can be explained by a coincidence with a highly converted transition.

Gate	109	194	196	377	416	625	731	839
68&80	-	-	x	-	x	x	x	-
305	-	-	-	-	x	-	-	-
416	-	-	-	x	-	x	-	x
625	x	x	-	-	x	-	-	-

Table 5.12: β-triggered γ-γ-coincidences within a time window of 2 μs. All energies are given in keV.

The full set of coincidences obtained from β triggered γ-γ-coincidences is shown in Tab. 5.12. Furthermore, the simple γ-γ-coincidences were studied. It was gated on the known transitions of ^{190}Tl, ^{190}Hg and ^{190}Au. From table 5.13 it is obvious that the 416.4, 625.4, 731.1 and 305.3 keV transitions are coincident to each other yielding a gamma cascade. The same holds for the 416.4, 625.4 and 839.7 keV transitions. Gating on the 196.8 keV transition, coincidences with the 416.4 and 625.4 transitions, but not with the 839.7 keV transition, were found, as expected from [Sin03].

	Gate										
Coinc	68	80	416	625	731	839	305	196	296	301	143
68	(x)	(x)	x	x	x	x	x	(x)	x	x	x
80	(x)	(x)	x	(x)	x	-	-	-	x	-	x
416	x	x	-	x	x	x	x	x	-	-	-
625	x	x	x	-	x	x	x	x	-	-	-
731	x	x	x	x	-	-	x	-	-	-	-
839	x	-	x	x	-	-	-	-	-	-	-
305	x	-	x	x	x	-	-	-	-	-	-
206	-	-	-	-	-	-	#	-	-	-	-
296	-	x	-	-	-	-	-	-	-	x	-
143	x	x	-	-	-	-	-	-	-	-	-
445	-	-	x	-	-	-	-	-	-	-	-
313	-	-	-	-	-	-	-	#	-	-	-
301	-	-	-	-	-	-	-	-	x	-	-
157	-	-	-	-	-	-	-	-	-	-	x

Table 5.13: γ-γ-coincidences between the both detectors at the implantation point. Lines coincident with this gate are marked by a 'x'. Coincidences that are most likely due to backscattering of 511 keV gamma-ray are marked by a '#'. All energies are given in keV.

It might be that the 196 keV transition is a fake, originating from a 511 keV gamma-ray backscattering between the two detectors. Therefore, no conclusion can be drawn on this coincidence. The gate on the two ^{190}Au transitions at 296 and 301 keV does not yield any new information. While gating on the 143 keV transition of ^{190}Hg a coincident line at 157 keV was observed which is not placed in the decay scheme so far.
Finally, some effort was made to obtain a half-life from the data. Benefit was taken from drops in the proton current which lead to a decreased count rate according to the half-life. In those cases the sum of the net counts of the 4 strongest transitions was recorded every 60 s yielding the decay curve shown in Fig. 5.14. This yields a half-life of 3.62(27) min which is in agreement with the half-life from the high-spin state.

The preceding section demonstrated how decay spectroscopy can add valuable information to mass-measurement results. In the case of ^{193}Tl the results from

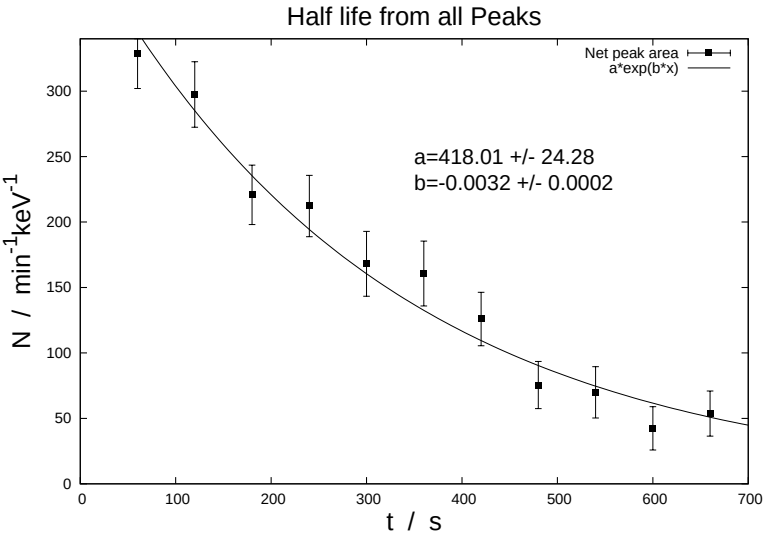

Figure 5.14: Half-life determination for ^{190}Tl from the sum of the 4 strongest transitions every 60 s.

the decay spectroscopy help to identify the measured state as the isomer. For ^{194}Tl, mass measurements yielded a dominant isomeric state. With the results from the decay measurement the decay pattern of the high-spin state could be assigned to this state and thus confirm the previous assignment. The combination of mass and decay measurements allowed to determine the excitation energy for the first time which is in agreement with the value predicted from systematics. The second measurement campaign on neutron-deficient Tl isotopes showed that already with one detector in addition the accessible information increases significantly. Besides β-γ-coincidences it was possible to study γ-γ-coincidences. Both helped to improve the understanding of the data for ^{190}Tl. In addition, it must be noted that the limits of the decay station behind a Penning-trap mass spectrometer were highlighted by the measurements on ^{184}Tl, ^{193}Tl and ^{195}Tl. They show that the yield of the desired ions must be high enough and the half-life must be long enough to be measured successfully. In addition, gamma-ray intensities must be high enough to lead to significant peaks in the gamma-ray spectrum. The approach for the half-life determination has to be improved, since for ^{190}Tl it was only possible during drops in the proton irradiation.

6. Physics discussion

The Tl (Z=81) isotopes only miss one proton to close the major shell to the next magic number. This allows to explain some basic features, as for example total angular momentum, in the following referred to as spin, and parity, directly in the view of the single-particle shell model [JA60].
Also due to the prominent isomerism, the neutron-deficient Tl isotopes have been investigated for a few years, but many of their properties are still not known or understood. Thus, they are very interesting for current nuclear-structure research. In the odd-A isotopes those features arise from the unpaired proton, whereas in the even-A isotopes they are due to the proton-neutron (p-n) interaction. Thus, the Tl isotopes can be an ideal test case for investigating p-n interactions. In addition, the isomers with excitation energies of only a few hundred keV are most likely due to single-particle excitation and thus form an ideal test case for shell-model predictions. In the neighboring nuclei it was shown that another feature is visible at low energies, when approaching the neutron mid-shell at $N = 104$, namely shape coexistence [Hea83].
Below, the current knowledge about the neutron-deficient Tl isotopes is summarized which includes the results from the recent ISOLTRAP measurements.

6.1. Mass

With the present ISOLTRAP campaign on neutron-deficient Tl isotopes the masses for $^{190,193m,194(g+m),195g}$Tl were measured and their uncertainties could be reduced significantly. The masses have been compared to different mass models [Bor12]. The liquid drop model [LPT03, MS66, BB36] represents macroscopic models which only take into account macroscopic properties of the nucleus such as the volume. For this model the strongest deviation from the measured values was found, as expected since the pairing effect was omitted. Another approach is to model the nuclear force in the framework of quantum mechanics, leading to microscopic models. The HFB21 [GCP10] and the D1M [Gea09] were chosen. They are microscopic models which construct a Hartree-Fock-Bogoliubov-Hamiltonian with an effective two-body interaction. The first makes use of the infinite-range Skyrme force [Sky56] and the latter of the finite-range Gogny force [DG80]. Finally, a model that takes into account both, macroscopic and microscopic aspects, was used for comparison - the finite range droplet model FRDM1995 [Mea95, Mea12]. All three models are in agreement with the measured values, although it was noted that none of them reproduces the pairing effect properly [Bor12]. A comparison to the shell model which would be interesting, especially in the context of the following discussion, was not carried out.

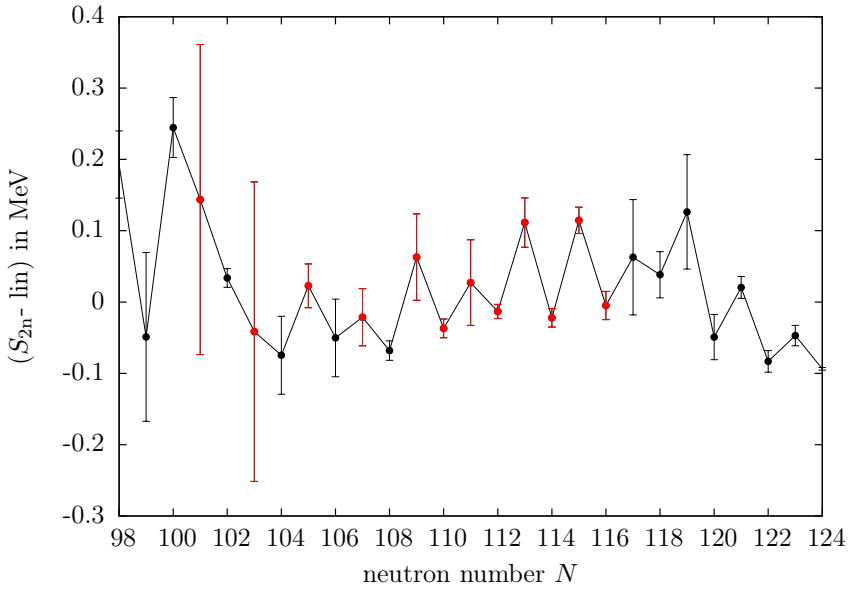

Figure 6.1: Odd-even staggering in the S_{2n} values for Tl isotopes after subtracting the linear trend. Red dots are values which were influenced by the ISOLTRAP measurements. Adopted from [Bor12].

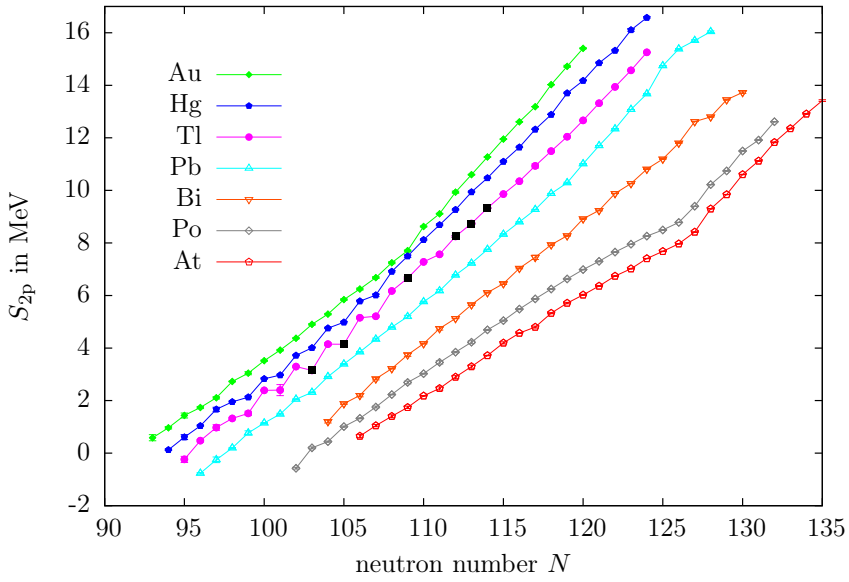

Figure 6.2: S_{2p} values in the Tl region. For Tl isotopes also an odd-even staggering is visible. Values which have been improved by the ISOLTRAP measurements are marked black. Adopted from [Bor12].

Furthermore, the mass values were used to calculate differences in binding energies B to uncover nuclear-structure effects. The considered differences are the two-neutron separation energy S_{2n} and the two-proton separation energy S_{2p}, defined as

$$S_{2n} = B(Z,N) - B(Z,N-2) \tag{6.1}$$
$$S_{2p} = B(Z,N) - B(Z-2,N). \tag{6.2}$$

The S_{2n} values become smoother than before thanks to the ISOLTRAP measurements, but after subtracting the linear trend an odd-even staggering was still visible [Bor12], see Fig. 6.1. Also the S_{2p} values show this odd-even effect, as shown in Fig. 6.2, that was already reported by [Wea08]. In this mass region such behavior is unique for the thallium isotopes and still not understood. Both works suggest that this can appear due to an unusual change in pairing energy, but also core polarizations could explain this staggering [Dea01].

6.2. Charge radius

The nuclear charge radius is a measure for the mean charge distribution within a nucleus and should thus be sensitive to deformation. The neutron-deficient Tl isotopes represent a region of the nuclear chart where shape coexistence is known.

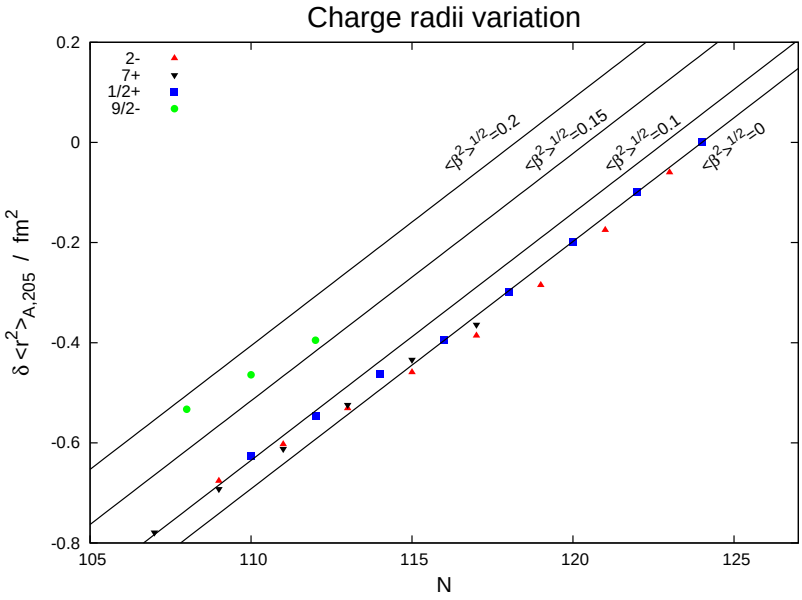

Figure 6.3: Change in root-mean-square charge radii for the neutron-deficient Tl isotopes with respect to ^{205}Tl . Numbers were calculated from the isotopic shifts given in [Bea87, Mea92]. The solid lines represent predictions from the deformed droplet model.

The most prominent example are the neutron-deficient Hg isotopes where it manifests as an odd-even staggering in the variation of the root-mean-square (rms) charge radii. This quantity is the difference between the rms radius of the isotope and the most abundant isotope. For the neutron-deficient Tl isotopes the same quantity is shown in Fig. 6.3. The solid lines represent predictions from the deformed droplet model where β is the deformation parameter and $<\beta^2>=0$ corresponds to no deformation. First, from shell closure at $N = 126$ towards mid-shell at $N = 104$ an increase in deformation for the Tl ground states and the even-A isomers is observed. Second, for $N \leq 113$ an odd-even shape staggering manifests for the isomers. This can be explained by their different origins, see discussion below. Finally, for the odd-A Tl isotopes a staggering between the ground state and isomer exists and thus they should have different shapes.

6.3. Spin and Parity

The single-particle approach is used to discuss spin and parity of the ground and isomeric states in neutron-deficient Tl isotopes. It is assumed that paired nucleons do not contribute. Applying this to the ground state of odd-A Tl isotopes, spin and parity are determined by the unpaired valence proton. The odd-A Tl isotopes are thus expected to have a $1/2^+$ ground state [ens12] throughout the isotopic chain that is due to the proton hole in the $3s_{1/2}$ orbit, see Fig. 2.1 and 6.4.

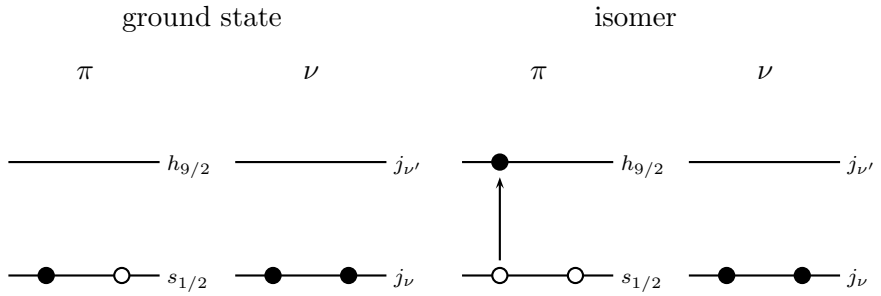

Figure 6.4: Creation of spin and parity in the single-particle picture for the ground and isomeric state in the odd-A Tl isotopes. Only the last nucleons are considered where π referes to protons and ν to neutrons. Filled circles denote particles and empty ones holes.

For the isomeric states in the odd-A neutron-deficient Tl isotopes with $A \leq 201$ a $9/2^-$ spin was observed. This spin can only originate from a proton excitation into the $1h_{9/2}$ level, see Fig. 6.4. In spherical nuclei this state lies above the shell gap, see Fig. 2.1, and would appear at much higher energies. The lowering in energy is explained on the one hand by the pairing interaction between the proton particle and holes (1p-2h) and on the other hand by the residual interaction between the 1p-2h configuration and the valence neutrons [Hea88]. In addition, it was found to be consistent with an oblate deformation of the isomeric state [Nea70].

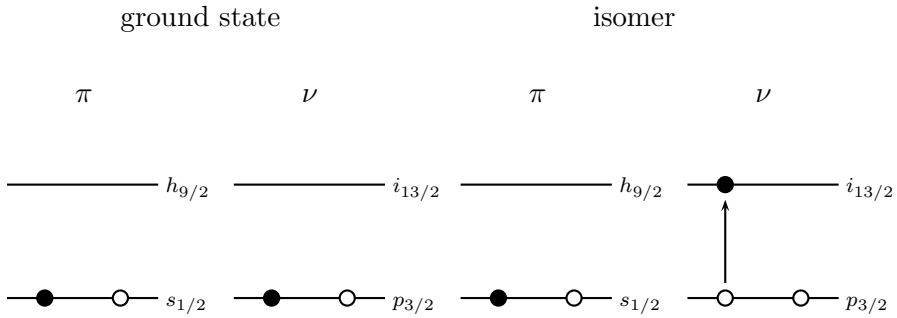

Figure 6.5: Creation of spin and parity of the ground and isomeric state in the even-A Tl isotopes. Only the last nucleons are considered. The unpaired neutron is assumed to occupy the $p_{3/2}$ level in the ground state, although other levels might contribute. Filled circles denote particles and empty ones holes.

In the ground state of the even-A Tl isotopes not only one proton but also one neutron is unpaired. The proton is again assumed to occupy the $s_{1/2}$ level. To predict the angular-momentum contribution of the unpaired neutron, the ground-state properties of neutron-deficient odd-A Pb and Hg isotopes can be studied. There, the proton shell is closed and ground-state properties should arise from the unpaired neutron. The odd-A Pb and Hg isotopes have spin and parity of $3/2^-$ for $A \leq 197$ and $A \leq 193$ [ens12], respectively, resulting from the neutron occupying the $p_{3/2}$ single-particle state. It is expected that the unpaired neutron in the even-A Tl isotopes with the same neutron number occupies this level as well, see Fig. 6.5. The nucleons then couple to a doublet 1^- and 2^-. Indeed, for $194 \leq A \leq 204$ 2^- ground states are observed, see [EWS75]. They however noted, that the ground state is likely due to a mixed configuration $((\pi s_{1/2} \otimes \nu p_{3/2}) + (\pi s_{1/2} \otimes \nu f_{5/2}))$, since the above neutron levels are close in energy. Assuming that the isomers in odd-A Pb isotopes are due to neutron excitations and that the same holds for the isomers in the even-A Tl isotopes, a $\pi s_{1/2} \otimes \nu i_{13/2}$ coupling is obtained, see Fig. 6.5. This yields a doublet of 6^+ and 7^+. The 7^+ member of this doublet is observed as the isomeric state in even-A Tl isotopes with $A \geq 194$.

6.4. Magnetic Dipole Moments

Measurements on magnetic dipole moments in neutron-deficient Tl isotopes confirmed the spin as predicted by the shell model. The magnetic moment $\boldsymbol{\mu}$ of a nucleus arises due to the magnetic moments of the nucleons. It can be related to the nuclear spin by

$$\boldsymbol{\mu} = g\frac{e}{2m_p}\mathbf{I} \tag{6.3}$$

where g is the nuclear g-factor, e the elementary charge, m_p the proton mass and $\mathbf{I}$ the total angular momentum as defined in Eq. 2.3. Again, in the view of the single-particle model only unpaired nucleons are assumed to contribute to the magnetic moment.

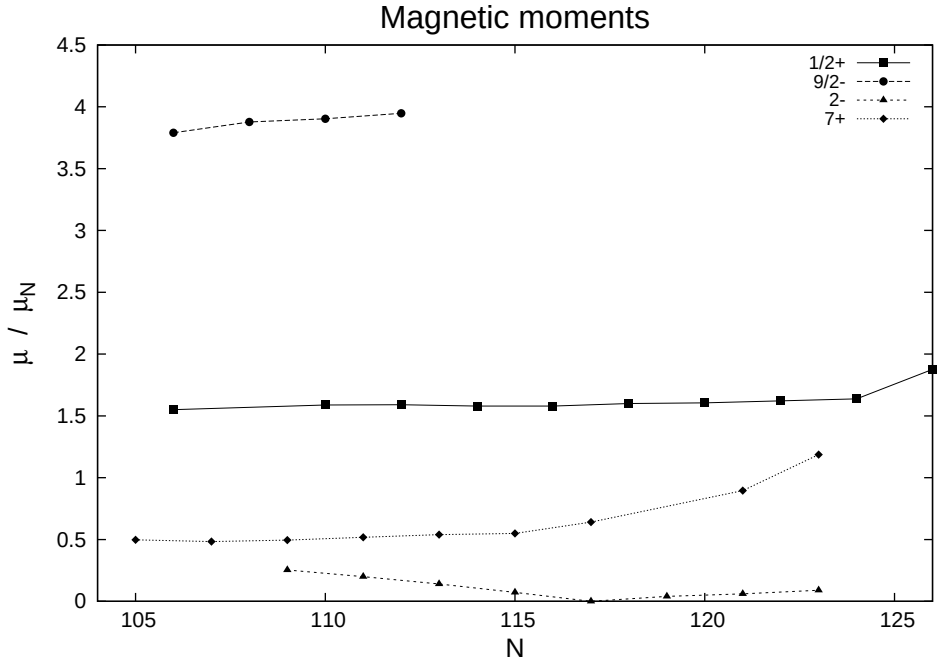

Figure 6.6: Magnetic dipole moments for the $1/2^+$ ground state and the $9/2^-$ isomeric state in the neutron-deficient odd-A Tl isotopes and for the 2^- and 7^+ state in the even-A Tl isotopes [EWS75, Bea87, Nea85, Mea92, Sea92, Sea95]. Uncertainties are smaller than the symbols.

The measured magnetic moments for the ground and isomeric states of the neutron-deficient Tl isotopes are shown in Fig. 6.6 [EWS75, Bea87, Nea85, Mea92, Sea92, Sea95]. For the odd-A Tl isotopes down to $A = 187$, except $A = 189$, they yield a $1/2^+$ ground-state and a $9/2^-$ isomeric-state. The smooth trend of the magnetic moments, while varying N, indicates no configuration change down to $N = 106$ in the odd-A Tl isotopes. The difference in magnetic moments of $1/2^+$ and $9/2^-$ state is due to the unpaired proton occupying different levels. For the even-A Tl isotopes the ground-state magnetic moments yield a spin 2 for $A \geq 194$ arising from a $\pi s_{1/2} \otimes \nu f_{5/2}$ configuration. However, for $N < 117$ a different trend is observed than for $N > 117$ which might indicate the $\pi s_{1/2} \otimes \nu p_{3/2}$ admixture in the 2^- states towards mid-shell, as suggested by [EWS75].

6.5. Excitation energies

The $9/2^-$ isomeric states in odd-A Tl isotopes arise from the $h_{9/2}$ proton intruder, as discussed above. The excitation energies of the isomeric states are known down to $A = 183$, except $A = 191$. The systematics of the excitation energy of the $9/2^-$ state in the odd-A Tl isotopes are shown in Fig. 6.7 [Hea83]. First, it is remarkable that the excitation energy for $102 \leq N \leq 120$ is less than

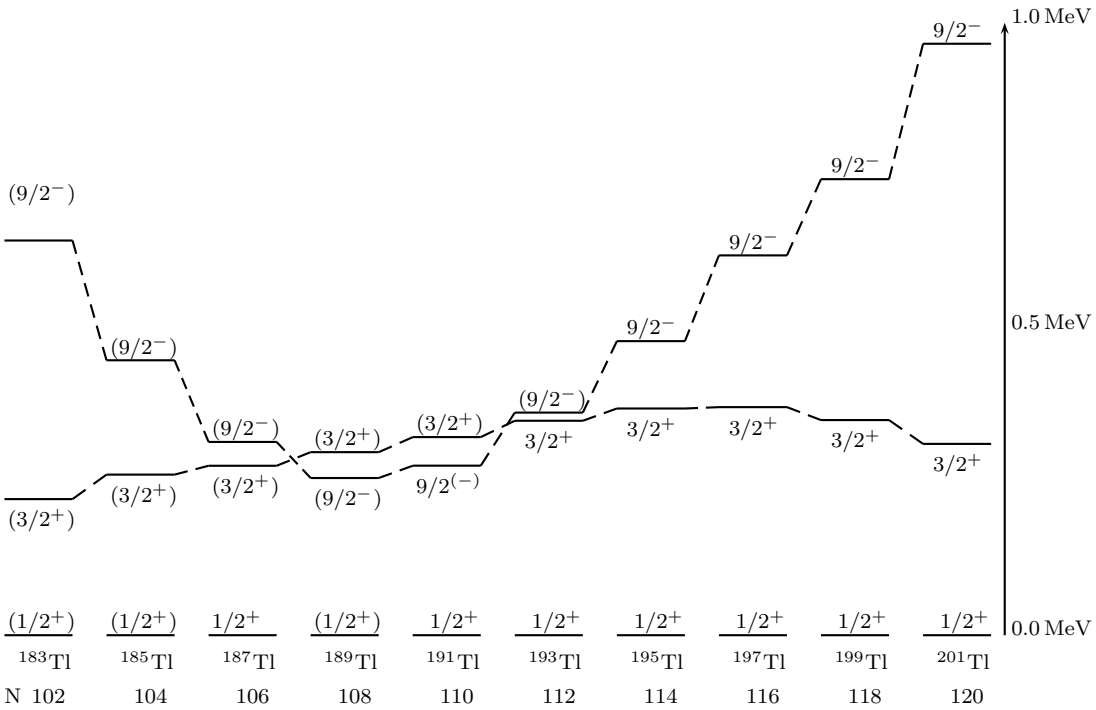

Figure 6.7: Energy systematics for the $(9/2^-)$ level in the odd-A Tl isotopes, from to [Hea83].

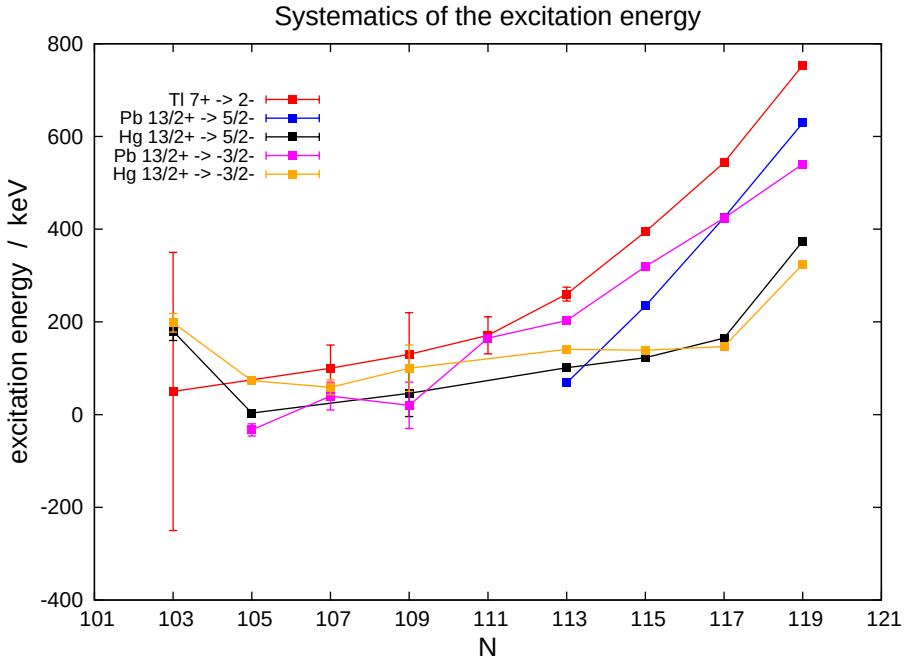

Figure 6.8: Systematics of the excitation energy of the isomeric states in neutron-deficient odd-N Hg, Tl and Pb isotopes. Data is taken from [ens12] and this work.

1 MeV. Second, a minimum in excitation energy appears at $N = 108$, although it would be rather expected at mid-shell. The lowering in excitation energy was already discussed before. However, no model can reproduce this effect quantitatively [Hea83]. The excitation energies of the 7^+ states in even-A Tl isotopes were previously known for $A \geq 196$. An extrapolation of those data yielded an excitation energy for ^{194m}Tl of 300(200) keV. Within the combined mass and decay measurements with the ISOLTRAP experiment the excitation energy of the 7^+ state of 260(15) keV could be determined for the first time. The resulting energy systematics are shown in Fig. 6.8. For $N \geq 117$ a similar behavior to the $13/2^+ \rightarrow 5/2^-$ spacing in odd-A Pb isotopes was found [BG57]. Already [JA60] noted that the parallelism between the two curves is disturbed for $N = 115$. The deviation even continues for smaller N, as confirmed with the measurements presented in this work and [Bor12]. Taking also the $13/2^+ \rightarrow 5/2^-$ level spacings for Hg isotopes into account, it seems like the level spacings for Tl isotopes behave asymptotically to the $13/2^+ \rightarrow 5/2^-$ Pb and Hg curve. This hints to a similar configuration of these states and thus the isomers in even-A Tl isotopes being due to neutron excitations. The systematics for the $13/2^+ \rightarrow 3/2^-$ level spacings in the Pb isotopes are included into the discussion as well. For $N < 117$ the Tl curve approaches this curve which supports the idea of a mixed ground-state configuration, as suggested by [EWS75]. Finally, the systematics also show that the level spacing between the 2^- and 7^+ state goes towards zero for $N < 111$ and might even become negative. Thus, a change in ground- state spin and parity is expected towards neutron mid-shell.

6.6. Conclusion

In the preceding sections the nuclear properties of the neutron-deficient Tl isotopes were summarized. The present results from ISOLTRAP mass measurements combined with decay spectroscopy complement the data collected before. The resulting nucleon-separation energies confirm the odd-even staggering as observed by [Wea08]. A further investigation of this behavior and the shape coexistence which relies on the observation in the nuclear charge radii will be part of [Böh13]. The confirmation of the spin-state assignment and the new excitation energy for ^{194m}Tl follow the systematic trend which, together with the magnetic dipole moments, strengthen the idea of a mixed ground-state configuration.

7. Conclusion and Outlook

A new measurement principle at the ISOLTRAP experiment that combines high-precision mass measurements with nuclear decay spectroscopy has been presented. The technique allows to assign species and even states to masses and thus to determine complementary nuclear properties simultaneously. Within this work a new decay chamber has been built and the involved tape system has been improved. It was also pointed to the compact design of the decay station that allows to use it as a stand-alone experiment. Simulations to optimize the ion transport to the decay chamber have been performed. Depending on the choice of collimator they yield a transport efficiency up to 100%. In addition, the realization of a bending unit was studied which should improve the cooperation between mass and decay measurements in the future. The chosen model yielded a bending efficiency of 100%. For the data analysis detection-efficiency curves of the HPGe detectors have been determined using an approach that combines Geant4 simulations with measurements.
The combination of mass and decay measurements was first applied to the neutron-deficient Tl isotopes ^{184,190,193,194,195}Tl which all have isomeric states at only a few 100 keV excitation energy. The masses of the neutron-deficient Tl isotopes were measured with the Penning-trap mass spectrometer ISOLTRAP and their uncertainties could be decreased significantly. States were assigned from decay measurements with the attached decay station. For ^{193}Tl, only the isomer was observed. In ^{194}Tl the method allowed to determine the excitation energy of the isomer for the first time and to confirm the spin-state assignment. In ^{190}Tl, where the spin-state ordering of ground state and isomer is not known, only the high-spin state was measured. Besides these successful measurements, the limits of the method in terms of half-life, gamma-ray intensity and production yield have been discussed. The measurement results were used together with other nuclear properties to summarize the current knowledge of the neutron-deficient Tl isotopes. The masses and the nuclear charge radii point to a change in pairing energy towards neutron mid-shell. A theoretical description of the observed behavior is still missing. The systematics of ground-state and isomer spins, magnetic moments and excitation energies for the even-A Tl isotopes were found to support a mixed ground-state configuration for $N < 117$.
For the future, there exist several ideas how to improve the presented measurement principle. For example, high-precision mass measurements require ultra-high vacuum which is not the case while performing decay spectroscopy. Thus, it is proposed, supported by the results from simulations, to implement a bending unit and a differential pumping section. In addition, as discussed before, the cooperation of the two setups poses some experimental limits. On the one hand, the Penning trap favors less ions for its best performance whereas

decay spectroscopy is facilitated by more ions. Thus, one has to agree on a sample size that still allows good enough performance of the Penning trap. On the other hand, the ion of interest has to pass through the whole measurement cycle before being implanted at the decay station which results in a lower limit for the half-life. If no contamination is expected one could also use the decay-station system as a stand-alone system, as demonstrated. Another idea, under the assumption of less contamination, is the attachment of a decay-spectroscopy unit behind the MR-TOF-MS. With both suggestions shorter-lived species would become accessible. Finally, by modifying the decay-spectroscopy setup, more decay information could be determined. For example, β-decay could be studied in terms of energy. There are also lots of nuclei where information about conversion electrons is missing. In [Cea11] it was even suggested to study α-decays. These suggestions would require a different detector than the scintillator since simulations on electrons indicate that the scintillator is not suitable for this task. Suitable detectors might be passivated implanted planar silicon (PIPS) detectors. If these measurements are feasible at all depends on whether the decay particles can leave the tape and how their energy distribution changes. The range of α-particles in matter can be calculated with programs like SRIM [sri12] and the energy distribution can be studied with Geant4 [gea12]. These ideas represent not only an increase in information for one nuclei but also in the number of nuclei of interest. Of course, decay-spectroscopy experiments with the mobile decay station would benefit from these changes as well.
For a deeper understanding of the nuclear structure in neutron-deficient nuclei in the vicinity of the magic proton number $Z = 82$ further measurements are required. To extend the studies presented in this work, the spin-state ordering and the excitation energies of the isomers in ^{188,190}Tl should be measured. This might be challenging since for ^{190}Tl only the high-spin state was observed. If a α-decay system is available one could access the information from mass measurements on $^{194(g+m)}$Bi and their subsequent α-decays. A further investigation of the odd-even staggering in the Tl isotopes and the shape coexistence which relies on the observation in the nuclear charge radii will be carried out in [Böh13]. It may benefit from the shape-coexistence studies by laser spectroscopy, as suggested by [Aea11]. In addition, a study of the isomerism in the neutron-deficient bismuth isotopes, with one proton above the shell closure at $Z = 82$, might help to understand the behavior observed in the nucleon-separation energies of the Tl isotopes. Finally, the isomers in neutron-deficient polonium isotopes which are also due to neutron excitations into the $i_{13/2}$ level are under investigation with respect to shape coexistence. Their excitation energies and α-decays should be measured [Cea11].

A. Ion motion in a Penning trap

The ion motion in an ideal Penning trap is described in more detail in [BG86] and [MGW05]. As it was already stated in chapter 3 an ideal Penning trap is the superposition of a weak electrostatic quadrupole field described by

$$\Phi(x, y, z) = \frac{U_0}{2d^2}\left(2z^2 - x^2 - y^2\right) \tag{A.1}$$

with a strong magnetic field $\mathbf{B} = (0, 0, B)$ that can be obtained from the vector potential $\mathbf{A} = B/2(-y, x, 0)$. U_0 is the voltage applied between the ring electrode and the endcaps and d is a parameter depending on the trap geometry. The general Lagrangian $\mathcal{L}$ of a particle with charge q and mass m in an electromagnetic field is

$$\mathcal{L}(\mathbf{r}, \dot{\mathbf{r}}) = \frac{m}{2}\dot{\mathbf{r}} - q\left(\Phi(\mathbf{r}, t) - \dot{\mathbf{r}} \cdot \mathbf{A}(\mathbf{r}, t)\right). \tag{A.2}$$

From the Euler-Lagrange equations the following equations of motion of the ion in cartesian coordinates are obtained

$$\frac{\mathrm{d}^2x}{\mathrm{d}t^2} - \omega_0\frac{\mathrm{d}y}{\mathrm{d}t} - \frac{1}{2}\omega_z^2 x = 0 \tag{A.3}$$

$$\frac{\mathrm{d}^2y}{\mathrm{d}t^2} + \omega_0\frac{\mathrm{d}x}{\mathrm{d}t} - \frac{1}{2}\omega_z^2 y = 0 \tag{A.4}$$

$$\frac{\mathrm{d}^2z}{\mathrm{d}t^2} + \omega_z^2 z = 0, \tag{A.5}$$

where

$$\omega_0 = \omega_{\mathrm{cycl}} = \frac{qB}{m}, \qquad \omega_z = \sqrt{\frac{2qU_0}{md^2}}. \tag{A.6}$$

Equation (A.5) describes a harmonic oscillation in z-direction which is decoupled from the motion in the x-y-plane. The motion in the x-y-plane can be understood by introducing the coordinate $u = x + \mathrm{i}y$ that reduces (A.3) and (A.4) to

$$\frac{\mathrm{d}^2u}{\mathrm{d}t^2} + \mathrm{i}\omega_0\frac{\mathrm{d}u}{\mathrm{d}t} - \frac{1}{2}\omega_z^2 u = 0. \tag{A.7}$$

The ansatz $u = e^{-\mathrm{i}\omega t}$ leads to the solutions

$$\omega_+ = \frac{1}{2}(\omega_0 + \omega_1), \quad \omega_- = \frac{1}{2}(\omega_0 - \omega_1), \quad \omega_1 = \sqrt{\omega_0^2 - 2\omega_z^2}, \tag{A.8}$$

where ω_+ is called the reduced cyclotron frequency and ω_- is called the magnetron frequency. To trap the ion, ω_1 is required to be real from which the minimal magnetic field for stable confinement can be determined. In total the

motion of the ion in the trap, as shown in Fig. A.1, is a superposition of three independent eigenmotions namely an oscillation along the z-direction between the two endcaps, a slow oscillation in the x-y-plane with ω_- and a fast oscillation in the x-y-plane with ω_+.

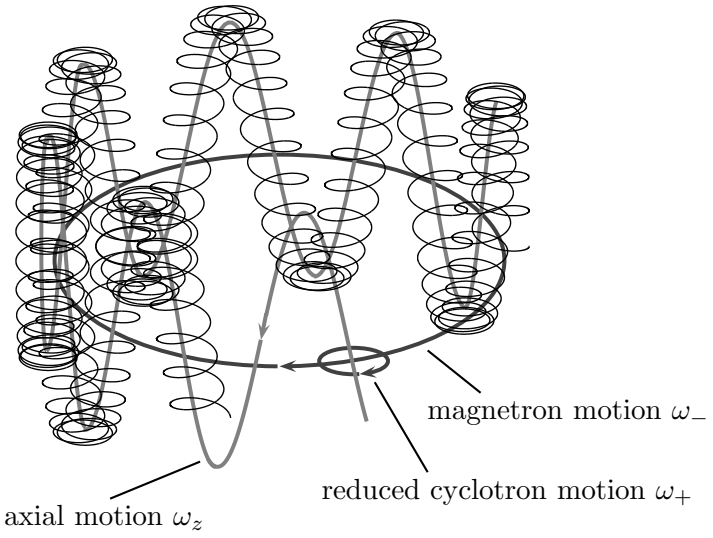

Figure A.1: Sketch of the superposition of the three eigenmodes of an ion in an ideal Penning trap

The following general relations hold

$$\omega_{\text{cycl}} = \omega_+ + \omega_- \tag{A.9}$$

$$\omega_{\text{cycl}}^2 = \omega_+^2 + \omega_-^2 + \omega_z^2 \tag{A.10}$$

$$\omega_{\text{cycl}} \approx \omega_+ > \omega_z > \omega_-. \tag{A.11}$$

Here (A.9) is the relation of interest concerning the coupling of the magnetron and reduced cyclotron motion. Relation (A.10) is known as the invariance theorem since it also holds for real Penning traps. Finally a Taylor expansion for the magnetron frequency while taking into account (A.11) leads to a first order term that is mass independent.
To consider the energy of the system the Hamilton function is calculated

$$\mathcal{H} = \frac{1}{2m}\left(p_x^2 + p_y^2 + p_z^2\right) - \frac{\omega_c}{2}(xp_y - yp_x) + \frac{\omega_1^2}{2}(x^2 + y^2) + \frac{m\omega_z^2}{2}z^2 \tag{A.12}$$

where $p_i = \partial\mathcal{L}/\partial\dot{r}_i$ are the canonical momenta. After eliminating the cross

terms via canonical transformation

$$q_{\pm} = \frac{1}{\sqrt{2}} \left(\sqrt{m\omega_1} x \mp \frac{p_y}{\sqrt{m\omega_1}} \right) \tag{A.13}$$

$$p_{\pm} = \frac{1}{\sqrt{2}} \left(\pm \sqrt{m\omega_1} y + \frac{p_x}{\sqrt{m\omega_1}} \right) \tag{A.14}$$

$$q_z = \sqrt{m\omega_z} z, \quad p'_z = \frac{p_z}{\sqrt{m\omega_z}} \tag{A.15}$$

one ends up with

$$\mathcal{H} = \frac{\omega_+}{2}(p_+^2 + q_+^2) - \frac{\omega_-}{2}(p_-^2 + q_-^2) + \frac{\omega_z}{2}(p_z'^2 + q_z^2). \tag{A.16}$$

Except for the minus sign in front of the magnetron term this looks like the Hamiltonian of 3 harmonic oscillators. An increase in magnetron energy thus leads to a decrease in total energy and vice versa.

B. Xia control commands

As reported in chapter 3 the signals from the decay spectroscopy setup are fed into Xia DGF-4C modules which are connected to a PC with LInux as operating system. In the following the most important control commands are listed.

```
mb_boot_dgf              #(re)start DGF
mb_setup_dgf             #load channel settings
mb_mca [CN] x -t         #record temporary data for x seconds
cne CLU_[Ch]A0.spc       #investigate temporary data
mb_sample [Ch]A0         #internal scope for specified channel
mb_showdgf [CN] [SN]     #print information on module
                         #(e. g. run time and life time)
watch cat rates *        #print count rate for each channel
mb_collector             #start acquisition
mb_start_writer          #write data into file
CTRL+C                   #stop acquisition/writing data
```

[CN] refers to the crate number (typically 0), [SN] is the slot number and [Ch] is the channel number. The output directory and the output name can be defined in '.mb' which requires sourcing afterwards. The configuration for each channel is stored in 'dgf_config_[Ch]A0.setup' files where parameters such as the gain and offset can be adapted. Changes in these files require reloading the channel settings.

C. Switch for the pulsed cavity behind the RFQ buncher

As mentioned in chapter 3, the switch that controls the voltage of the pulsed cavity behind the RFQ buncher has recently been re-designed within the PhD thesis of R. Wolf to provide the quality of ion bunches required by the following electrostatic mirror trap, that is described in section 3.2.2. There ion bunches

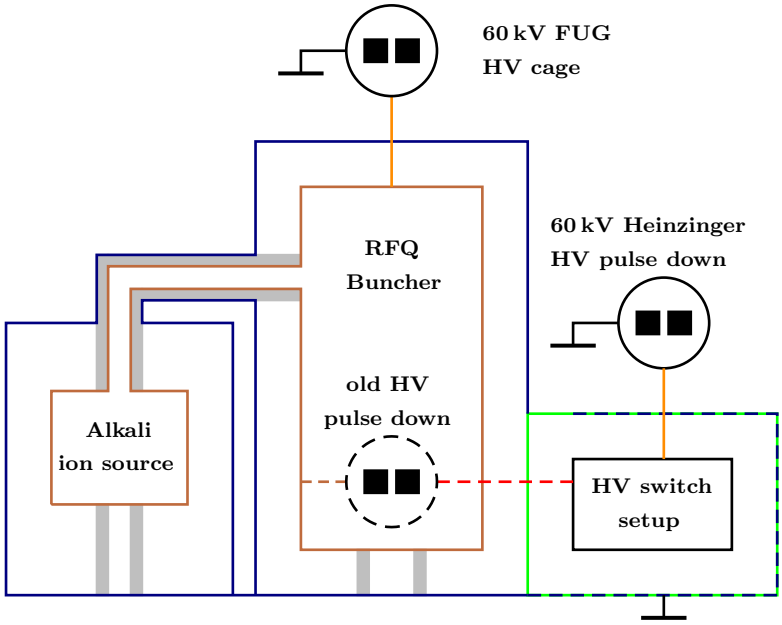

Figure C.1: Modifications on the high-voltage platform. Parts of the old setup that changed are indicated by dashed lines. The high-voltage supply for the switch of the pulsed cavity is now decoupled from the high-voltage cage.

of almost Gaussian shape with a width of only a few ten ns are needed. Such bunches are provided by decoupling the high-voltage (HV) power supply for the switch from the HV power supply for the HV cage housing the RFQ cooler and buncher, as shown in Fig. C.1. Currently, the HV cage is connected to a 60 kV FUG power supply and the power supply for the HV switch is a Heinzinger PNChp ±60 kV, 10 mA. The latter is a high-stability power supply that ensures to be stable to roughly 200 mV at 60 kV within 8 hours. The switching itself is now done by a fast Behlke switch of type HTS 651-10-GSM, 65 kV, 100 Apk. It provides rise times on the order of a few μs and fall times on the order of a few hundred ns. The circuit diagram and the timing of the switch are shown in Fig. C.2. The combination of the power supply with the new switch enables

high repetition rates up to 1 kHz.

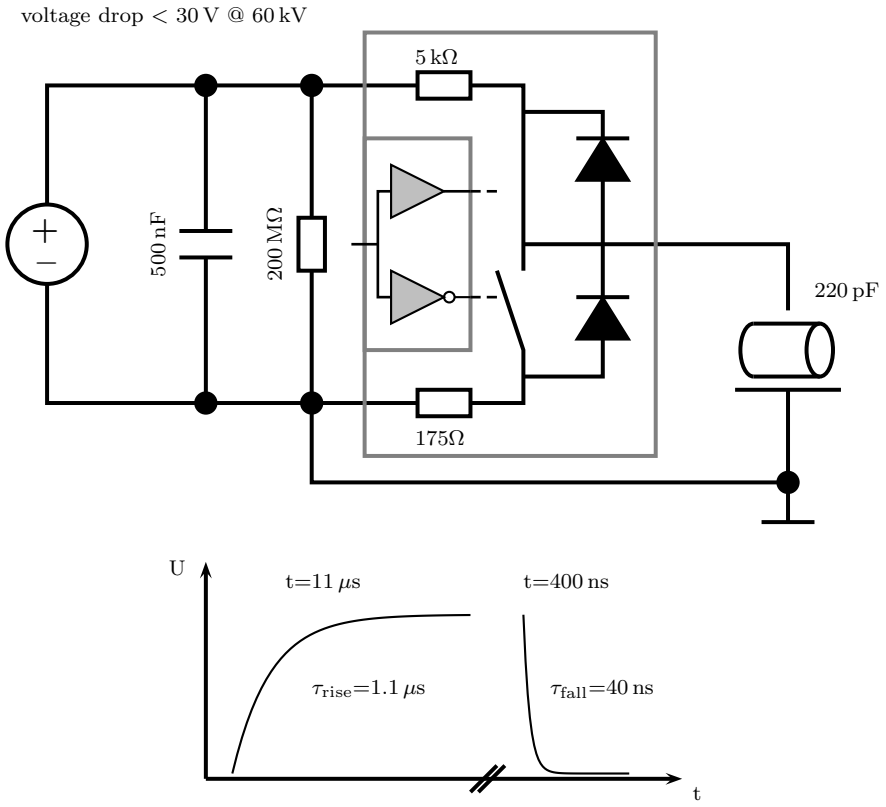

Figure C.2: Circuit diagram and timing of the new Behlke switch for the pulsed cavity behind the RFQ cooler and buncher.

D. Counting decision limits

There exist different approaches how to analyze a peak in a gamma-ray spectrum. Here, the one suggested by [Gil08] is presented. A window is chosen such that it contains the peak, with n_P bins, as well as some lower and upper background, with n_B bins each, see Fig. D.1.

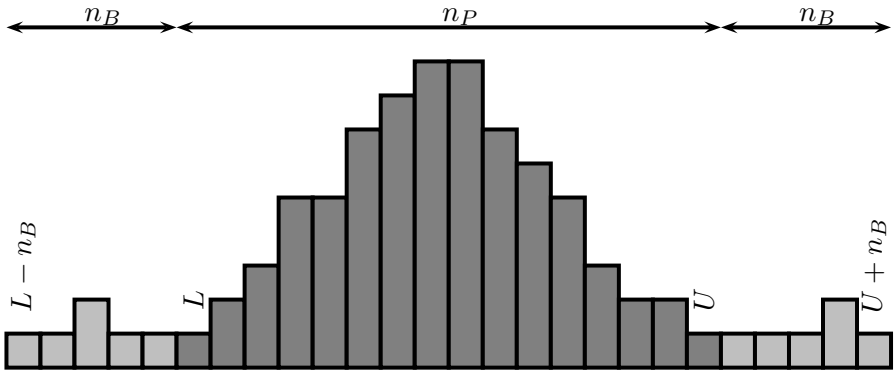

Figure D.1: Example for a peak window with n_p bins in the peak area and n_B bins in the lower and upper backround.

Adding the bin content in each of the three areas yields the gross count P and the background count B

$$P = \sum_{i=L}^{U} N_i \tag{D.1}$$

$$B = \sum_{i=L-n_B}^{L-1} N_i + \sum_{i=U+1}^{U+n_B} N_i \tag{D.2}$$

where N_i is the content of the ith bin. The background S in the peak area can be estimated with

$$S = n_P \cdot \frac{B}{2 \cdot n_B}. \tag{D.3}$$

The net count of the peak is then $A = P - S$. To decide whether the net count is significant it is compared to the critical limit L_c

$$L_c = 1.645\sqrt{S(1 + n_P/2n_B)}. \tag{D.4}$$

If the net count is smaller than this critical limit the peak is not detected in the 95% confidence limit. To conclude how many counts are at maximum in

this peak, an upper limit L_U has to be calculated. It is given by

$$L_U = A + 1.645\sqrt{A + S(1 + n_P/2n_B)} \tag{D.5}$$

for a 95% confidence limit.

Bibliography

[Aea06] E. Achterberg et al. Nuclear Data Sheets for A=193. *Nuclear Data Sheets*, 107:1 – 224, 2006.

[Aea11] A. N. Andreyev et al. Shape coexistence in the lightest Tl isotopes studied by laser spectroscopy. CERN-INTC-2011-005; INTC-P-291, 2011.

[AWT03] G. Audi, A.H. Wapstra, and C. Thibault. The Ame2003 atomic mass evaluation: (II). Tables, graphs and references. *Nucl. Phys. A*, 729:337 – 676, 2003.

[BB36] H. A. Bethe and R. F. Bacher. Stationary States of Nuclei. *Rev. Mod. Phys.*, 8:82–229, 1936.

[Bea76] C. R. Bingham et al. Decay of mass-separated ^{190}Tl and ^{190}Hg. *Phys. Rev. C*, 14:1586–1600, 1976.

[Bea87] J. A. Bounds et al. Nuclear structure of light thallium isotopes as deduced from laser spectroscopy on a fast atom beam. *Phys. Rev. C*, 36:2560–2568, 1987.

[Bea90] G. Bollen et al. The accuracy of heavy-ion mass measurements using time of flight-ion cyclotron resonance in a Penning trap. *Journ. of Appl. Phys.*, 68:4355–4374, 1990.

[Bea96] G. Bollen et al. ISOLTRAP: a tandem Penning trap system for accurate on-line mass determination of short-lived isotopes . *Nucl. Inst. and Meth. A*, 368:675–697, 1996.

[Bea99] D. Belic et al. Photoactivation of ^{180}Ta^m and Its Implications for the Nucleosynthesis of Nature's Rarest Naturally Occurring Isotope. *Phys. Rev. Lett.*, 83:5242, 1999.

[Bea04] K. Blaum et al. Population inversion of nuclear states by a Penning trap mass spectrometer. *EPL*, 67:586–592, 2004.

[Beq96] H. Bequerel. Sur les radiations invisibles emises par les corps phosphorescents. *Comptes Rendus*, 122:501–503, 1896.

[Bet71] H. A. Bethe. Theory of Nuclear Matter. *Ann. Rev. of Nucl. Sci.*, 21:93–244, 1971.

[BFS10] S. K. Bogner, R. J. Furnstahl, and A. Schwenk. From low-momentum interactions to nuclear structure. *Progress in Particle and Nuclear Physics*, 65:94 – 147, 2010.

[BG57] I. Bergstrom and Andersson G. Nuclear Energy Levels and Multipole Transitions in the Lead Region, Part I. *Arkiv Fysik*, 12, 1957.

[BG86] L. S. Brown and G. Gabrielse. Geonium theory: Physics of a single electron or ion in a Penning trap. *Rev. Mod. Phys.*, 58:233–311, 1986.

[Böh13] Ch. Böhm. *in preparation.* PhD thesis, 2013.

[Bor12] Ch. Borgmann. *Mass Measurements of Exotic Ions in the Heavy Mass Region for Nuclear Structure Studies at ISOLTRAP.* PhD thesis, 2012.

[BS97] G. C. Baldwin and J. Solem. Recoilless gamma-ray lasers. *Rev. Mod. Phys.*, 69:1085, 1997.

[CC97] C. B. Collins and J. J. Carroll. Evidence for K-mixing in 178Hf. *Hyp. Int.*, 107:3, 1997.

[Cea89] J. J. Carroll et al. Accelerated decay of $^{180}\mathrm{Ta}^m$ and ^{174}Lu in stellar interiors through (γ, γ') reactions. *Astrophys. J.*, 344:454, 1989.

[Cea11] T. E. Cocolios et al. Study of the odd-A, high-spin isomers in neutron-deficient trans-lead nuclei with ISOLTRAP. CERN-INTC-2011-009; INTC-P-293, 2011.

[Cha32] J. Chadwick. Possible Existence of a Neutron. *Nature*, 129, 1932.

[Chu99] Z. Chunmei. Nuclear Data Sheets for A=195. *Nuclear Data Sheets*, 86:645–784, 1999.

[Dea01] J. Dobaczewcki et al. Odd-even staggering of binding energies as a consequence of pairing and mean-field effects. *Phys. Rev. C*, 63:024308, 2001.

[DG80] J. Dechargé and D. Gogny. Hartree-Fock-Bogolyubov calculations with the D1 effective interaction on spherical nuclei. *Phys. Rev. C.*, 21:1568–1593, 1980.

[ens12] ENSDF. `www.nndc.bnl.gov/ensdf/`, April 2012.

[EWS75] C. Ekström, G. Wannberg, and Y. S. Shishodia. Hyperfine structure and nuclear magnetic moments of some neutron-deficient thallium isotopes. *Hyp. Int.*, 1:437–458, 1975.

[Fea08] V. N. Feedoseev et al. ISOLDE RILIS: New beams, new facilities. *Nucl. Inst. and Meth. B*, 266:4378–4382, 2008.

[Fea12] V. N. Feedoseev et al. Upgrade of the resonance ionization laser ion source at ISOLDE on-line isotope separation facility: New lasers and new ion beams. *Rev. Sci. Inst.*, 83:02A903, 2012.

[Fir96] R. B. Firestone. *Table of Isotopes - CD ROM Edition.* 1996.

[Fou11] L. Fouché. ISOLTRAP Tape Station: synergy between mass and nuclear spectroscopy. Internship Report, 2011.

[GCP10] S. Goriely, N. Chamel, and J. M. Pearson. Further explorations of Skyrme-Hartree-Fock-Bogoliubov mass formulas. XII. Stiffness and stability of neutron-star matter. *Phys. Rev. C*, 82:035804, 2010.

[Gea76] G. M. Gowdy et al. Structure of the Odd-Mass $^{187-197}$Hg Levels. Technical report, ORNL, 1976.

[Gea09] S. Goriely et al. First Gogny-Hartree-Fock-Bogoliubov Nuclear Mass Model. *Phys. Rev. Lett.*, 102:242501, 2009.

[gea12] Geant4. `http://geant4.cern.ch/`, February 2012.

[Gil08] G. Gilmore. *Practical Gamma-ray Spectroscopy.* John Wiley & Sons, 2008.

[GM09] H. Geiger and E. Marsden. On a diffuse reflection of the α-particles. *Proc. R. Soc. Lond. A*, 82:495–500, 1909.

[gps12] GPS. `http://reat.space.qinetiq.com/gps/`, June 2012.

[Hea83] K. Heyde et al. Coexistens in odd-mass nuclei. *Phys. Rep.*, 102:291–393, 1983.

[Hea88] K. Heyde et al. Intruder states in odd-mass and odd-odd nuclei. *Nucl. Phys. A*, 484:275–294, 1988.

[Hea01] F. Herfurth et al. A linear radiofrequency ion trap for accumulation, bunching, and emittance improvement of radioactive ion beams. *Nucl. Inst. and Meth. A*, 469:254–275, 2001.

[Hea02] F. Herfurth et al. Accurate mass measurements of very short-lived nuclei. *Eur. Phys. J. A*, 15:17–20, 2002.

[Her01] F. Herfurth. *Ein neuer Ionenstrahlkühler und -pulser für ISOLTRAP und Massenmessungen an radioaktiven Argonisotopen.* PhD thesis, 2001.

[HJS49] Otto Haxel, J. Hans D. Jensen, and Hans E. Suess. On the "magic numbers" in nuclear structure. *Phys. Rev.*, 75:1766–1766, 1949.

[iso12] ISOLDE. `http://isolde.web.cern.ch`, July 2012.

[JA60] B. Jung and G. Andersson. Low mass odd-odd isomers of thallium. *Nucl. Phys*, 15:108–124, 1960.

[Kea95] M. König et al. Quadrupole excitation of stored ion motion at the true cyclotron frequency . *Int. J. Mass Spectrom. Ion. Process.*, 142:95–116, 1995.

[Kea03] A. Kellerbauer et al. From Direct to Absolute Mass Measurements: A Study of the Accuracy of ISOLTRAP. *Eur. Phys. J. D*, 22:53–56, 2003.

[Kea07] M. Kowalska et al. Decay studies and mass measurements on isobarically pure neutron-rich Hg and Tl isotopes. CERN-INTC-2007-022; INTC-P-232, 2007.

[Kea12] M. Kowalska et al. Trap-assisted decay spectroscopy with ISOLTRAP. *Nucl. Inst. and Meth. A*, 689:102–107, 2012.

[Kno00] G. F. Knoll. *Radiation Detection and Measurement*. John Wiley & Sons, 2000.

[Kra88] K. S. Krane. *Introductory to Nuclear Physics*. John Wiley & Sons, 1988.

[Kug00] E. Kugler. The ISOLDE facility. *Hyp. Int.*, 129:23–42, 2000.

[LPT03] D. Lunney, J. D. Pearson, and C. Thibault. Recent trends in the determination of nuclear masses. *Rev. Mod. Phys.*, 75:1021–1082, 2003.

[lua12] Lua. `http://www.lua.org/`, July 2012.

[May48] Maria G. Mayer. On closed shells in nuclei. *Phys. Rev.*, 74:235–239, 1948.

[May49] Maria Goeppert Mayer. On closed shells in nuclei. ii. *Phys. Rev.*, 75:1969–1970, 1949.

[Mea92] R. Menges et al. Nuclear moments and the change in the mean square charge radius of neutron deficient thallium isotopes. *Zeit. f. Phys. A Hadrons and Nuclei*, 341:475–479, 1992.

[Mea95] P. Möller et al. Nuclear Ground-State Masses and Deformations. *At. Data Nucl. Data Tables*, 59:185381, 1995.

[Mea08] M. Mukherjee et al. ISOLTRAP: An on-line Penning trap for mass spectrometry on short-lived nuclides. *Eur. Phys. J. A*, 35:1–29, 2008.

[Mea12] P. Möller et al. New Finite-Range Droplet Mass Model and Equation-of-State Parameters. *Phys. Rev. Lett*, 108:052501, 2012.

[MGW05] F.G. Major, V.N. Gheorghe, and G. Werth. *Charged Particle Traps*. Springer, 2005.

[MJ55] M. G. Mayer and J. H. D. Jensen. *Elementary Theory of Nuclear Shell Structure*. Wiley, 1955.

[MPD12] J. Magill, G. Pfennig, R. Dreher, and Z. Sóti. Karlsruher Nuklidkarte, 2012.

[MS66] W. D. Myers and W. J. Swiatecki. Nuclear masses and deformations. *Nucl. Phys.*, 81:1–60, 1966.

[Nai10] S. Naimi. *Onsets of nuclear deformation from measurements with the Isoltrap mass spectrometer*. PhD thesis, 2010.

[Nea70] J. O. Newton et al. Possible oblate shape of $\frac{9}{2}$-isomer in ^{199}Tl. *Nucl. Phys. A*, 148:593–614, 1970.

[Nea85] R. Neugart et al. Nuclear Magnetic Moment of ^{207}Tl. *Phys. Rev. Lett.*, 55:1559–1562, 1985.

[Pfü12] M. Pfützner. Radioactive decays at limits of nuclear stability. *Rev. Mod. Phys.*, 48:567–619, 2012.

[PPW01] Steven C. Pieper, V. R. Pandharipande, R. B. Wiringa, and J. Carlson. Realistic models of pion-exchange three-nucleon interactions. *Phys. Rev. C*, 64:014001, 2001.

[Rap12] E. Rapisarda. priv. communication, 2012.

[RHea97] H. Raimbault-Hartmann et al. A cylindrical Penning trap for capture, mass selective cooling, and bunching of radioactive ion beams . *Nucl. Inst. and Meth. B*, 126:378–382, 1997.

[roo12] Root. `http://root.cern.ch/`, August 2012.

[Rut98] E. Rutherford. Uranium Radiation and the Electrical conduction Produced by it. *Philos. Mag.*, 47:109, 1898.

[Rut11] E. Rutherford. The scattering of α and β particles by matter and the structure of the atom. *Philos. Mag. Series 6*, 21:669–688, 1911.

[Sch08] S. Schwarz. *Lecture Notes in Physics 749*, chapter Simulations for Ion Traps - Buffer Gas Cooling. 2008.

[Sea91] G. Savard et al. A new cooling technique for heavy ions in a Penning trap. *Phys. Lett. A*, 158:247–252, 1991.

[Sea92] H. A. Schuessler et al. Nuclear Moments of the Neutron-Deficient Thallium Isotopes. *Hyp. Int.*, 74:13–21, 1992.

[Sea95] H. A. Schuessler et al. Nuclear Spectroscopy using Lasers at Oak Ridge National Laboratory: Experiments with stable (past) and radioactive (future) tandem beams. *Nucl. Inst. and Meth. A*, 352:583–587, 1995.

[sim12] SIMION. `http://simion.com/`, February 2012.

[Sin03] B. Singh. Nuclear Data Sheets for A=190. *Nuclear Data Sheets*, 99:275481, 2003.

[Sin06] B. Singh. Nuclear Data Sheets for A=194. *Nuclear Data Sheets*, 107:1531–1746, 2006.

[Sky56] T. H. R. Skyrme. The nuclear surface. *Philos. Mag.*, 1:1043–1054, 1956.

[Sod17] F. Soddy. The complexity of the chemical elements. *Nature*, 99:433–438, 1917.

[sri12] SRIM. `http://www.srim.org/`, October 2012.

[Vea74] T. B. Vandlik et al. Decay Scheme of ^{193}Tl. *Izv. Akad. Nauk*, 38:689–694, 1974.

[Ven11] M. Venhart. priv. communication, 2011.

[Vil00] M. P. Villard. Sur la reflexion et la refraction des rayons cathodiques et des rayons deviables du radium. *Comptes Rendus*, 130:1010–1012, 1900.

[vW35] C. F. von Weizsäcker. Zur Theorie der Kernmassen. *Zeit. f. Physik*, 96:431–458, 1935.

[vW36] C. F. von Weizäcker. Metastabile Zustände der Atomkerne . *Naturwissenschaften*, 24:813–814, 1936.

[WD99] P. M. Walker and G. D. Dracoulis. Energy traps in atomic nuclei. *Nature*, 399:35–40, 1999.

[WD01] P. M. Walker and G. D. Dracoulis. Exotic Isomers in Deformed Atomic Nuclei. *Hyp. Int.*, 135:83–107, 2001.

[WDC01] P. M. Walker, G. D. Dracoulis, and J. J. Carroll. Interpretation of the excitation and decay of ^{180}Ta^m through a $K^\pi = 5^+$ band. *Phys. Rev. C*, 64:061302, 2001.

[Wea08] C. Weber et al. Atomic mass measurements of short-lived nuclides around the doubly-magic ^{208}Pb. *Nucl. Phys. A*, 803:1–29, 2008.

[Wea12a] P. M. Walker et al. Properties of neutron-rich hafnium high-spin isomers. CERN-INTC-2012-009; INTC-P-325, 2012.

[Wea12b] R. Wolf et al. On-line separation of short-lived nuclei by a multi-reflection time-of-flight device. *Nucl. Inst. and Meth. A*, 686:82–90, 2012.

[WEM11] R. Wolf, M. Eritt, G. Marx, and L. Schweikhard. A multi-reflection time-of-flight mass separator for isobaric purification of radioactive ion beams. *Hyp. Int.*, 199:115–122, 2011.

[Woo14] R. Wood. *in preparation.* PhD thesis, 2014.

[xia12] XiA. `www.xia.com`, April 2012.

Acknowledgement

This work was only possible thanks to the help with words and deeds of the following people.
First, I would like to thank my supervisor Kai Zuber for offering me this PhD project, including stays at the ISOLTRAP experiment at CERN, and his constant support during the whole time.
Special thanks to Magda Kowalska, Susanne Kreim and Thomas Cocolios. The first invented this project in the first place and all of them played a special role in the experiment, the data analysis and interpretation. Thanks for the many fruitful discussions and the meaningful comments to the manuscript.
Thanks to the entire ISOLTRAP collaboration and in particular the local group for maintaining the experiment. Thanks to Sarah Naimi for introducing me to the experiment and to SIMION. Thanks to Martin Breitenfeld, Marco Rosenbusch, Robert Wolf, Frank Wienholtz and Vladimir Manea for the nice time in the lab. Thanks to Christopher Borgmann for the discussions about the thallium mass data.
Thanks to the technical group of ISOLDE for preparing the separator as good as possible before each experiment.
Thanks to Gary Simpson for his support with the data acquisition.
Thanks to Martin Venhart for the discussions about Geant4.
Thanks to the people from the mechanical workshop for their excellent realization of the decay chamber.
Finally, I would like to thank my parents, sister and Sven for motivating me whenever it was necessary.

Versicherung

Hiermit versichere ich, dass ich die vorliegende Arbeit ohne unzulässige Hilfe Dritter und ohne Benutzung anderer als der angegebenen Hilfsmittel angefertigt habe; die aus fremden Quellen direkt oder indirekt übernommenen Gedanken sind als solche kenntlich gemacht. Die Arbeit wurde bisher weder im Inland noch im Ausland in gleicher oder ähnlicher Form einer anderen Prüfungsbehörde vorgelegt.

Die Dissertation wurde an der Technischen Universität Dresden unter der Betreuung von Prof. Dr. Kai Zuber angefertigt.

Es wurden zuvor keine Promotionsvorhaben unternommen.

Ich erkenne die Promotionsordnung der Fakultät Mathematik und Naturwissenschaften der TU Dresden vom 23.02.2011 an.

Dresden, den 19.12.2012 Juliane Stanja